

HYDROTHERMAL PARTICLE SYNTHESIS OF BARIUM TITANATE AND  
PARTICLE FORMATION MECHANISM STUDY

By

JOOHO MOON

A THESIS PRESENTED TO THE GRADUATE SCHOOL  
OF THE UNIVERSITY OF FLORIDA IN PARTIAL FULFILLMENT  
OF THE REQUIREMENTS FOR THE DEGREE OF  
DOCTOR OF PHILOSOPHY

UNIVERSITY OF FLORIDA

1996

Dedicated to

my family

in appreciation of their patience, support and encouragement

## ACKNOWLEDGMENTS

I would like to express the most sincere thanks to my advisor, Dr. James H. Adair, for his guidance, encouragement, and constructive criticism throughout my research, and for increasing my knowledge of colloidal and solution chemistry. I would also like to thank Dr. Anthony Brennan, Dr. Brij Moudgil, Dr. E. Dow Whitney, all of the Department of Materials Science and Engineering, and Dr. Dinesh Shah of the Department of Chemical Engineering for serving on my committee, and Dr. Changwon Park for substituting for Dr. Dinesh Shah at short notice. Special thanks are directed to Dr. Stephen A. Costantino and Dr. Sridhar Venigalla, Cabot Performance Materials, Boyertown, PA, for their useful suggestions and financial support for this study.

I also thank all of my colleagues in Materials Chemistry Group in the Department of Materials Science and Engineering at the University of Florida. I am particularly indebted to Robert Chodelka, Seung Beom Cho, Craig Habeger, Tuo Li, Henrik Krarup, Jeff Kerchner, and Robert Sabia for their research assistance and proof-reading my dissertation. I am grateful to Dr. Stanley Bates and Dr. Augusto Morrone, Richard Crockett, the staff of the Major Analytical Instrumentation Center at the University of Florida, for their technical help and analytical support in the characterization of specimens. I would like to take this opportunity to thank Pam Howell for her administrative support and assistance all along my research.

Finally, I would like to thank my parents, my beloved wife, Shinsook, and my adorable son, Gimin, and other family for their endless support, patience, encouragement, and belief in me.

## TABLE OF CONTENTS

	<u>page</u>
ACKNOWLEDGMENTS.....	iii
LIST OF TABLES .....	vi
LIST OF FIGURES .....	vii
ABSTRACT .....	xii
CHAPTERS	
1 INTRODUCTION .....	1
2 LITERATURE REVIEW.....	5
Introduction .....	5
Perovskite Ferroelectric Materials .....	6
Crystallographic Aspects of Ferroelectricity .....	6
Structural Origin of the Ferroelectric State .....	8
Applications of Perovskite Ferroelectrics .....	15
Chemical Synthesis of Perovskite Ferroelectric Powders .....	20
Definition of Particulate Materials.....	22
Properties and Characterization of Powders.....	22
Powder Synthesis Techniques .....	28
Solid-state reactions method .....	28
Precipitation/calcination method with metal salts .....	29
Metal alkoxide decomposition method.....	31
Polymeric metal organic-gel method (Pechini process).....	32
Precipitation from homogeneous solution (PFHS).....	33
Hydrothermal synthesis .....	34
Molten salt synthesis .....	35
Pyrolysis method .....	36
Mechanisms of Precipitation Process from Solution Phase .....	36
General Aspects of Precipitation Processes.....	38
Definition and Driving Force of Precipitation .....	39
Nucleation Theory .....	39
Classical theory .....	40
Kinetic theory .....	41
Growth Theory .....	42
Continuous growth model.....	44
Two-dimensional nucleation and growth theory.....	44
Screw dislocation theory (BCF theory).....	46
Surface reaction theory .....	47
Morphological theory.....	48
Physical Growth Mechanism for Monodisperse Particle Formation.....	51
Monomer addition model .....	53
Aggregative growth model .....	53
Summary .....	54

3	THERMODYNAMIC APPROACH TO HYDROTHERMAL SYNTHESIS OF BaTiO <sub>3</sub> .....	56
	Introduction .....	56
	Stability Diagram for the Ba-Ti-H <sub>2</sub> O System .....	56
	Aqueous Solution Chemistry .....	64
	Hydrolysis .....	66
	Condensation .....	68
	Complexation by Anion Species .....	72
	Modeling of the Ba-Ti-H <sub>2</sub> O System .....	72
	Conclusions .....	80
4	HYDROTHERMAL SYNTHESIS OF BaTiO <sub>3</sub> .....	82
	Introduction .....	82
	Background .....	83
	Materials and Methods .....	85
	Results and Discussion .....	89
	Characteristics of the Coprecipitated Ba-Ti Complex Gel .....	89
	Influence of Reaction Conditions on Phase Composition .....	89
	Influence of Reaction Conditions on Particle Size .....	95
	Dielectric Properties of Hydrothermally Derived Barium Titanate .....	99
	Hydrothermal Synthesis of Other Ferroelectric Ceramics .....	99
	Influence of the Chemically Modified Titanium Precursor .....	104
	Conclusions .....	111
5	PARTICLE FORMATION MECHANISMS OF BaTiO <sub>3</sub> UNDER HYDROTHERMAL CONDITIONS .....	112
	Introduction .....	112
	Materials and Methods .....	114
	Results and Discussion .....	116
	Conclusions .....	132
6	INFLUENCES OF TITANIUM PRECURSOR CHARACTERISTICS ON PARTICLE FORMATION MECHANISMS OF BaTiO <sub>3</sub> .....	133
	Introduction .....	133
	Materials and Methods .....	134
	Results and Discussion .....	136
	Ti Precursor Characteristics .....	136
	Reaction Conditions for Barium Titanate Particle Synthesis .....	139
	Influence of Ti Precursor Characteristics on Barium Titanate Particle Formation .....	141
	Conclusions .....	156
7	CONCLUSIONS AND SUGGESTIONS FOR FUTURE WORK .....	159
	Overall Conclusions .....	159
	Future Work .....	162
	LIST OF REFERENCES .....	164
	BIOGRAPHICAL SKETCH .....	179

## LIST OF TABLES

<u>Table</u>	<u>page</u>
2-1. Applications of Ferroelectrics since 1940 .....	18
2-2. Characteristics of Ceramic Starting Powders .....	24
2-3. Particle Size Analysis Methods and Size Ranges .....	26
2-4. Analytical Methods for Determination of Chemical Characteristics .....	27
2-5. Summarized References for Chemical Derived Perovskite Ferroelectric Powders .....	37
3-1. Reaction Constants for the Ti-H <sub>2</sub> O System at 25°C.....	58
3-2. Reaction Constants for the Ba-Ti-H <sub>2</sub> O System at 25°C .....	59
3-3. Standard Free Energy Formation in the Ba-Ti-H <sub>2</sub> O System .....	60
3-4. Possible Hydrolyzed Species of Barium and Titanium in Aqueous Solution .....	73
3-5. Electronegativities for Selected Species .....	76
3-6. The pH Range for Stable Metal-Anion Complexation .....	77
4-1. Influence of pH of Hydrothermal Reaction Medium on the Phase Composition ...	91
4-2. Charge Distribution in the Ti Precursor during Chemical Modification by Acetylacetone .....	109
5-1. Kinetic Data of the BaTiO <sub>3</sub> Formation Process at 75°C from the Modified Ti Precursor and Barium Acetate .....	117
5-2. Solid State Reaction Rate Equations .....	121
6-1. Kinetic Data for the BaTiO <sub>3</sub> Formation Process from the As-Received Ti Gel Precursor and Barium Hydroxide .....	143
6-2. Kinetic Data for the BaTiO <sub>3</sub> Formation Process from the Hydrothermally- Treated Ti Precursor and Barium Hydroxide .....	145

## LIST OF FIGURES

<u>Figure</u>	<u>page</u>
2-1. Crystal structure of perovskite $ABO_3$ .....	7
2-2. Interrelationship between piezoelectric, pyroelectric, and ferroelectric materials on the basis of crystal symmetry .....	9
2-3. Crystallographic transformations in $BaTiO_3$ .....	10
2-4. Free energy configurations as a function of $Ti^{4+}$ position in cubic and tetragonal phases of $BaTiO_3$ .....	12
2-5. Domain structure development: (a) surface charge associated with spontaneous polarization; and (b) formation of $180^\circ$ domains to minimize electrostatic energy .....	13
2-6. Schematic diagram of $180^\circ$ and $90^\circ$ domain structure in ferroelectrics .....	14
2-7. Hysteresis behavior of polarization as a function of the applied field and relevant domain rotation and growth process in the direction of an applied field ( $P_r$ is the remnant polarization) .....	16
2-8. Structure of a multilayer capacitor .....	19
2-9. Domino effect in ceramic processing: the role of the starting powders .....	21
2-10. Structure of primary particle: (a) single crystal; and (b) polycrystalline .....	23
2-11. Adsorbed layer of the solute on the surface of a growing crystal. The square, sphere, and triangle represent the crystal AB, hydrated $A^+$ , and hydrated anion $B^-$ , respectively .....	43
2-12. Growth model: (a) continuous growth mechanism; (b) two dimensional growth mechanism; and (c) spiral growth mechanism. The arrows indicate the growth direction of the crystal plane .....	45
2-13. Hypothetical crystal structure showing flat (F), stepped (S), and kinked (K) faces. The A, B, and C represent three different directions of the periodic bond chain .....	50
2-14. The LaMer-Dinegar model for monodisperse particle formation: (a) solute concentration as a function of precipitation time; and (b) precipitation rate for nucleation and growth as a function of solute concentration where I pre-nucleation stage, II nucleation stage, and III growth stage.....	52

3-1.	Theoretical phase stability diagram for the Ti-H <sub>2</sub> O system at 25°C based on the ideal solution approximation .....	62
3-2.	Theoretical phase stability diagram for the Ba-Ti-H <sub>2</sub> O system at 25°C based on the ideal solution approximation .....	63
3-3.	Phase stability diagram for the Ba-Ti-H <sub>2</sub> O system at 65°C including activity coefficients: (a) CO <sub>2</sub> free condition; and (b) in the presence of CO <sub>2</sub> . The dashed line indicates the results from the ideal solution approximation .....	65
3-4.	Schematic picture illustrating the solvated metal cation .....	67
3-5.	The charge-pH diagram indicating the type of solution species formed in aqueous solution as a function of the metal cation valence state .....	69
3-6.	The charge-electronegativity diagram illustrating the five different regimes of condensed species for the various metal cations .....	71
3-7.	The calculated hydrolysis ratio of both barium and titanium metal cations as a function of pH .....	74
3-8.	The electronegativity-solution pH diagram for [Ba-anions] complexation: (a) complexation in inner-shell coordination; (b) complexation in outer-shell coordination .....	78
3-9.	The electronegativity-solution pH diagram for [Ti-anions] complexation: (a) complexation in inner-shell coordination; (b) complexation in outer-shell coordination .....	79
4-1.	Tautomerism of acetylacetone .....	84
4-2.	Processing procedure used for preparing BaTiO <sub>3</sub> powder by hydrothermal methods .....	86
4-3.	The schematic diagram showing a 600 ml-capacity hydrothermal reactor used for preparing BaTiO <sub>3</sub> powders .....	88
4-4.	Characterization of the coprecipitated Ba-Ti gel: (a) TEM micrograph; and (b) TGA/DTA curves .....	90
4-5.	XRD patterns of the products prepared as a function of pH at 150°C for 18 hours .....	93
4-6.	XRD patterns of the products prepared as a function of synthesis temperature at the solution pH>13.5 reacted for 12 hours .....	94
4-7.	SEM micrographs of the prepared BaTiO <sub>3</sub> powders as a function of reaction parameters such as reaction concentration, temperature, and time, respectively: (a) at 0.1 M-75°C-4 hours; and (b) at 0.1 M-150°C-1 hour; (c) at 0.05 M-150°C-1 hour; and (d) at 0.025 M-150°C-1 hour .....	96
4-8.	Particle size distribution of the synthesized particles .....	98

4-9.	SEM micrographs showing the microstructure of the sintered BaTiO <sub>3</sub> at 1300°C for 3 hours followed by thermal etching 1200°C for 1 hour: (a) polished surface; and (b) fractured surface .....	100
4-10.	Dielectric constant and dielectric loss as a function of temperature for hydrothermally derived BaTiO <sub>3</sub> .....	101
4-11.	SEM micrographs of hydrothermally derived ferroelectric PbTiO <sub>3</sub> powders: (a) at 0.1 M-150°C-18 hours; and (b) at 0.05 M-150°C-18 hours .....	102
4-12.	SEM micrographs of hydrothermally derived ferroelectric PLZT powders: (a) at 0.1 M-150°C-18 hours; and (b) at 0.05 M-150°C-18 hours .....	103
4-13.	X-ray diffraction patterns indicating morphotropic boundary between the tetragonal and rhombohedral PZT as a function of the molar ratio of Zr:Ti. The reactions were performed at 150°C for 18 hours .....	105
4-14.	Chemical modification process of titanium isopropoxide by acetylacetone where OPr <sup>i</sup> and OEt represent the propoxy and ethoxy group, respectively .....	106
4-15.	Schematic picture illustrating structure of the coprecipitated Ba-Ti complex gel .....	110
5-1.	Possible formation mechanisms in the hydrothermal particle synthesis .....	113
5-2.	Schematic picture of the hydrothermal reactor used for low temperature kinetic study .....	115
5-3.	X-ray diffraction patterns of (110, 101) reflection showing a change in crystallinity as a function of reaction time during the barium titanate formation process from the hydrous Ba-Ti complex gel at 75°C .....	118
5-4.	Crystallization curves for BaTiO <sub>3</sub> produced from the hydrous Ba-Ti complex gel under hydrothermal conditions .....	119
5-5.	Johnson-Mehl-Avrami plot for the kinetic data of BaTiO <sub>3</sub> formation from the hydrous Ba-Ti complex gel at 75°C (m is the exponent constant and r <sup>2</sup> is the correlation coefficient) .....	122
5-6.	TEM micrographs showing formation process of BaTiO <sub>3</sub> from the hydrous Ba-Ti complex gel at 75°C as a function of reaction time: (a) 5 min (BK-06); (b) 15 min (BK-10); (c) 25 min (BK-14); and (d) 60 min (BK-17), respectively .....	123
5-7.	HRTEM micrograph of the sample extracted at a temperature of 42°C, 5 min after the precursor solution was introduced to the reactor. A selected area diffraction pattern (B=[111]) is also shown .....	125
5-8.	Diffraction patterns taken from the same area of the sample collected at 42°C, 5 min as a function of beam exposure time, indicating interaction between the sample and electron beam .....	126
5-9.	HRTEM micrograph of the sample BK-06 .....	128

5-10. The pH variation behavior of the supernatant as a function of reaction time .....	130
5-11. Schematic picture illustrating a proposed formation mechanism of BaTiO <sub>3</sub> in the modified Ti alkoxide and barium acetate system .....	131
6-1. X-ray diffraction patterns of the various titanium precursors: (a) calcined at 600°C for 1 hour; (b) hydrothermally treated at 150°C for 30 min; (c) dried at 130°C for 24 hours; and (d) the as-received wet Ti gel .....	137
6-2. TEM micrographs showing morphology of the titanium precursors: (a) and (b) the as-received wet Ti gel and its selected area diffraction pattern; (c) and (d) the hydrothermally treated Ti precursor at 150°C, 30 min and its selected area diffraction pattern .....	138
6-3. TGA/DTA curves for the as-received wet Ti gel. Sample was heated to 800°C at a rate of 10°C/min in air .....	140
6-4. XRD patterns of the hydrothermally synthesized products: (a) as a function of the total feedstock concentration at 95°C; and (b) as a function of the reaction temperature at the feedstock concentration of 0.2 M .....	142
6-5. Crystallization curves for BaTiO <sub>3</sub> at 75°C prepared by reacting the different Ti precursors in barium hydroxide aqueous solution .....	144
6-6. Johnson-Mehl-Avrami plot for the kinetic data of BaTiO <sub>3</sub> formation using the (a) as-received amorphous Ti gel and (b) hydrothermally treated Ti precursor. The m is exponent constant and r <sup>2</sup> is correlation coefficient .....	146
6-7. TEM micrographs showing the formation process of BaTiO <sub>3</sub> from the as-received Ti gel and barium hydroxide as a function of reaction time: (a) 3 min (BA-01); (b) 9 min (BA-02); (c) 35 min (BA-06); and (d) SADP for BA-02, respectively .....	147
6-8. TEM micrographs showing the formation process of BaTiO <sub>3</sub> from the hydrothermally treated Ti precursor and barium hydroxide as a function of reaction time: (a) 5 min (BC-03); (b) 25 min (BC-06); (c) 60 min (BC-11); and (d) SADP for BA-03, respectively. The 'AN' and 'BT' represent reflection spots for the anatase and BaTiO <sub>3</sub> , respectively .....	148
6-9. HRTEM micrograph of the sample BA-01 including selected area diffraction pattern .....	150
6-10. TEM micrograph showing microstructure of the BaTiO <sub>3</sub> single particle (sample BA-05) .....	151
6-11. Schematic picture illustrating a proposed formation mechanism of BaTiO <sub>3</sub> in the amorphous Ti gel and barium hydroxide system .....	152
6-12. TEM micrographs showing the microstructure of BaTiO <sub>3</sub> particles (BC-05) embedded in aggregated anatase: (a) bright field image; and (b) dark field image .....	154

6-13. HRTEM micrograph of the sample BC-05 including selected area diffraction pattern. The double arrows indicate a split reflection spot for BaTiO<sub>3</sub> due to lattice misfit. The 'an' and 'bt' represent reflection spots for the anatase and BaTiO<sub>3</sub>, respectively ..... 155

6-14. Schematic picture illustrating a proposed formation mechanism of BaTiO<sub>3</sub> in the hydrothermally treated Ti gel and barium hydroxide system ..... 157

Abstract of Dissertation Presented to the Graduate School  
of the University of Florida in Partial Fulfillment of the  
Requirements for the Degree of Doctor of Philosophy

## HYDROTHERMAL PARTICLE SYNTHESIS OF BARIUM TITANATE AND PARTICLE FORMATION MECHANISM STUDY

By

Jooho Moon

August, 1996

Chairman: Dr. James H. Adair

Major Department: Materials Science and Engineering

A low temperature hydrothermal particle synthesis procedure for barium titanate has been developed. The use of chemically modified titanium isopropoxide by acetylacetone and barium acetate, produces homogeneously mixed Ba-Ti complex gels by addition into a KOH solution. The cubic BaTiO<sub>3</sub> particles from such precursor suspensions are directly precipitated at temperatures as low as 50°C. The pH condition is found to be a critical reaction parameter such that production of phase pure BaTiO<sub>3</sub> requires a highly alkaline condition (i.e., pH > 13). The chemically modified Ti alkoxide allows intimate mixing between the components, which reduces the diffusion distance for reactants and eventually enhances crystallization kinetics.

Particle formation mechanisms of BaTiO<sub>3</sub> in this particular hydrothermal system are also investigated. Samples extracted during isothermal reaction at 75°C are analyzed to monitor crystallization behavior and to examine microstructural evolution during transformation. Spherical 4 nm size nuclei are observed at the very early stages of reaction using a high resolution TEM. The Johnson-Mehl-Avrami kinetic analysis corroborates

microstructural evidence which indicates that the formation mechanism is dissolution and recrystallization.  $\text{BaOH}^+ + \text{Ti}(\text{OH})_4^0 \leftrightarrow \text{BaTiO}_3 + 2\text{H}_2\text{O} + \text{H}^+$  is proposed as the relevant chemical reaction, in which the hydroxyl species ( $\text{OH}^-$ ) play a kinetically important role in nucleation and growth.

Similar efforts are directed towards evaluating the influences of the Ti precursor characteristics on particle formation mechanisms. Crystallization kinetics of  $\text{BaTiO}_3$  at  $75^\circ\text{C}$  from two different Ti precursors (i.e., amorphous Ti gel and hydrothermally treated nanosize anatase) in aqueous  $\text{Ba}(\text{OH})_2$  solution are compared. The Ti precursor type significantly affects both the reaction kinetics and particle characteristics of the synthesized  $\text{BaTiO}_3$ . Relatively spherical 5 to 10 nm size  $\text{BaTiO}_3$  nuclei which grow from the amorphous Ti gel matrix are monitored in the early stage of process. In the case of  $\text{BaTiO}_3$  formation from the hydrothermally treated Ti precursor, on the other hand, 80 nm size  $\text{BaTiO}_3$  particles growing from the aggregated anatase are observed. A phase-boundary controlled mechanism in which the surface reaction is a rate controlling step is proposed in the former case. In contrast, a dissolution and recrystallization mechanism in which  $\text{BaTiO}_3$  nucleates heterogeneously on the anatase particles is predicted in the latter case.

## CHAPTER 1 INTRODUCTION

The outstanding dielectric and ferroelectric properties of barium titanate ( $\text{BaTiO}_3$ ) make it the desirable material for a variety of applications including multilayer capacitors, transducers, thermistors, and electrooptic devices [1-6]. The growing demand for fully utilizing these useful material properties with better functionality and performance has accelerated the development of powder synthesis techniques. Barium titanate is traditionally produced by solid-state reactions between  $\text{BaCO}_3$  and  $\text{TiO}_2$ , typically at temperatures greater than  $900^\circ\text{C}$  [7, 8]. However, this conventional method suffers from particle agglomeration and contamination problems during the high temperature calcination and subsequent milling steps. To overcome such limitations, several chemical solution synthesis routes as nonconventional powder preparation techniques have been developed [9]. These methods include thermal decomposition of coprecipitated barium titanyl oxalate [10], sol-gel [11], molten salts method [12], and hydrothermal synthesis [13, 14]. The principal benefits of solution synthesis include the intimate mixing between components on the atomic or molecular level in the solution state, which results in ultra-fine ceramic powders with high-purity and good chemical homogeneity at lower temperatures. It is demonstrated that such well-controlled physical and chemical properties of the powders can be inherited through subsequent ceramic processing and eventually allow the sintered ceramics to exhibit improved microstructure and performance [15, 16].

Among various solution synthesis methods, hydrothermal synthesis is particularly promising. Hydrothermal particle synthesis refers to processes in which aqueous homogeneous solutions or suspensions of precursors are treated at elevated temperatures in pressurized vessels [17, 18]. Because crystalline powders are directly produced during the

hydrothermal treatment, the need for high temperature calcination and milling procedures to remove aggregates is eliminated [19]. In other solution synthesis techniques such as coprecipitation and sol-gel, however, the post particle synthesis procedures are still necessary to crystallize the amorphous reaction product, similar to solid-state reactions. The same disadvantages associated with the conventional methods can be introduced to the powders chemically derived from such methods. In this regard, hydrothermal processing offers a potentially superior technique for low-cost and low-temperature production of advanced ceramic powders.

Extensive research has been directed towards the hydrothermal synthesis of barium titanate [20-26]. In general,  $\text{BaTiO}_3$  is hydrothermally synthesized by reacting Ti precursors such as anhydrous  $\text{TiO}_2$  oxide (rutile and anatase), hydrous amorphous Ti gel ( $\text{TiO}_2 \cdot x\text{H}_2\text{O}$ ), and Ti alkoxides in alkaline barium aqueous solution. Various barium salts including hydroxide, nitrate, acetate, and chloride can be used to prepare the aqueous  $\text{Ba}^{2+}$  solution. Except for barium hydroxide, the other barium salts require additional base reagents to control solution pH. Reaction temperatures range from 30 to  $500^\circ\text{C}$  depending upon the precursor type and reaction conditions. The reaction product is usually a metastable cubic perovskite  $\text{BaTiO}_3$  unless relatively large particles greater than  $1.0\text{ }\mu\text{m}$  are produced under special conditions of higher reaction temperature and increased reaction time [25].

Two possible formation mechanisms have been proposed so far for the hydrothermal synthesis of  $\text{BaTiO}_3$  [27-32]. The first entails dissolution and recrystallization in which  $\text{Ba}^{2+}$  aqueous species react with hydrolyzed Ti solution species such as  $[\text{Ti}(\text{OH})_6]^{2-}$  or  $[\text{Ti}(\text{OH})_4]^0$  to form nuclei [28-31]. Nucleation can occur either homogeneously from bulk solution or heterogeneously at the surface of  $\text{TiO}_2$  or related amorphous phases. Since homogeneous nucleation requires relatively higher supersaturation conditions, it is likely to occur when a highly reactive and relatively soluble hydrous Ti gel is involved. On the other hand, heterogeneous nucleation will predominate

when a sparingly soluble  $\text{TiO}_2$  oxide is used in which a solid surface locally dissolves and reacts with  $\text{Ba}^{2+}$  [29, 31]. The other mechanism is in-situ transformation which includes diffusion of  $\text{Ba}^{2+}$  into the undissolved  $\text{TiO}_2$  oxide, resulting in an outside layer of  $\text{BaTiO}_3$  with an unreacted  $\text{TiO}_2$  core [25, 31, 32]. Hertl proposed a topochemical process in which the rate limiting step is the reaction between  $\text{Ba}^{2+}$  and  $\text{TiO}_2$  at the interface, and the kinetic rate depends on the available surface area of  $\text{TiO}_2$  [32]. However, currently there is no direct microstructural evidence to differentiate these mechanisms. This difficulty is attributed to the closed nature of the hydrothermal reaction conducted at elevated temperature and pressure, making it difficult to identify solution species and to study reaction kinetics and underlying mechanisms [33]. Since the particles are prepared as a result of chemical reactions in solution phase, however, fundamental knowledge regarding the thermodynamics and solution chemistry is required to fully understand hydrothermal reactions.

The interaction between the solid and solution phases determines particle formation mechanisms, by which the physical characteristics of the resulting powders are also decided. In the  $\text{BaTiO}_3$  hydrothermal synthesis, dynamic reaction behavior of the Ti precursor towards  $\text{Ba}^{2+}$  and the surrounding environment plays an important role in determining the particle formation mechanism. At low temperatures (e.g.,  $< 100^\circ\text{C}$ ), in particular, it is believed that  $\text{BaTiO}_3$  forms via heterogeneous reaction between the stable solid Ti precursor and aqueous  $\text{Ba}^{2+}$  species due to the low solubility of titania in aqueous solution [31]. Under such conditions, it is relatively difficult to control the particle characteristics. With this point of view, the objective of the current research is to develop a hydrothermal synthesis method to produce well-defined barium titanate at lower temperatures. To accomplish such a goal, chemically modified Ti alkoxide is introduced to the hydrothermal synthesis. The chemical modification controls the hydrolysis and condensation behavior of the Ti alkoxide, resulting in a homogeneous solution when the barium acetate aqueous solution is added, instead of forming a polymeric Ti gel. From

such a precursor solution, the intimately mixed Ba-Ti complex gel is obtained, which subsequently transforms into well-crystalline  $\text{BaTiO}_3$  at lower temperatures, experiencing a decreased diffusion distance. In this material system, the effects of reaction conditions on the phase composition and particle characteristics are investigated. Dielectric properties of the sintered samples prepared with the hydrothermally derived  $\text{BaTiO}_3$  are also determined.

Another relevant objective of this study is to evaluate particle formation mechanisms of  $\text{BaTiO}_3$  under hydrothermal conditions. Special emphasis is directed toward investigating the influence of Ti precursor characteristics on the formation mechanisms. How reactivity differences in the Ti precursors lead to particle formation of  $\text{BaTiO}_3$  with different characteristics via different reaction kinetics is evaluated. The approach is to collect intermediate-stage samples reacted for varying durations at the isothermal condition for characterization by X-ray diffraction and transmission electron microscopy. Crystallization kinetics are analyzed by the Hancock and Sharp method. Microstructural features during reactions are monitored to provide evidence of a morphological relationship with the analyzed kinetics interpretation.

This dissertation is divided into six major chapters. Chapter 2 provides a detailed literature review on the phenomena of ferroelectricity and chemical synthesis methods. The fundamentals of precipitation processes are discussed with an emphasis on nucleation and growth theories in the later part of this chapter. Chapter 3 presents a theoretical thermodynamic approach to the hydrothermal synthesis of  $\text{BaTiO}_3$  to understand the significance of solution chemistry played in the hydrothermal reaction within the frame of the stability diagram and the aqueous chemistry of metal cations. Hydrothermal synthesis of  $\text{BaTiO}_3$  particles is the focus of Chapter 4. The study of  $\text{BaTiO}_3$  particle formation mechanisms is presented in Chapter 5 and 6. Finally, the conclusions and suggestions for future work are presented in Chapter 7.

## CHAPTER 2 LITERATURE REVIEW

### Introduction

Ferroelectrics are a special group of dielectric materials which exhibit a non-linear polarization behavior resulting in large dielectric constants [34]. The non-linearity in the polarization process results from reversible and spontaneous polarization unique to ferroelectric materials. A very wide range of materials show ferroelectric behavior, ranging from inorganic crystals (such as potassium dihydrogen phosphate), through organic crystals (such as triglycine sulphate), to polymers (such as polyvinylidene flouride) and liquid crystals [35]. However, by far the most widely used ferroelectrics are oxide single-crystals and ceramic materials including perovskite compounds such as  $\text{BaTiO}_3$ , tungsten-bronze compounds such as  $(\text{Sr},\text{Ba})\text{Nb}_2\text{O}_6$ , and the ilmenite compound  $\text{LiNbO}_3$  [36]. In the current chapter, the perovskite ferroelectric oxides are selected in order to explain ferroelectric spontaneous polarization and domain formation which are critical factors to understand the properties of ferroelectrics. To fabricate these ferroelectric ceramics with better functionality and performance via ceramic processing, the importance for starting powder materials is emphasized. Then, chemical solution synthesis methods for ferroelectric ceramic powders are reviewed. In the later section, special attention is drawn toward hydrothermal synthesis. Fundamentals of the precipitation process including nucleation and growth theories are also discussed in an attempt to better understand particle formation mechanisms underlying hydrothermal reactions.

### Perovskite Ferroelectric Materials

The perovskite ferroelectrics, named after the perovskite mineral,  $\text{CaTiO}_3$ , possess the generalized formula  $\text{ABO}_3$  and the crystal structure is shown in Figure 2-1 [37]. The B ions are octahedrally coordinated by oxygen ions and these oxygen octahedra are linked together by corners. The A ions occupy sites which are 12-fold coordinated by oxygen ions. A variety of ions can fit into this structure as long as both the charge balance and radius ratio criteria are satisfied, which indicates that a wide range of properties can be obtained. Examples of perovskite ferroelectrics which are widely used include  $\text{BaTiO}_3$ ,  $\text{PbTiO}_3$ , and  $\text{KNbO}_3$ . It is also possible to form a broad range of solid solutions between perovskite end-members, such as  $\text{BaTiO}_3$ - $\text{SrTiO}_3$  and  $\text{PbTiO}_3$ - $\text{PbZrO}_3$ , in addition to ternary and quaternary systems. The perovskite structure can also exist in the form of complex systems (i.e.,  $\text{AB}^{(\text{I})}\text{B}^{(\text{II})}\text{O}_3$ ) such as  $\text{Pb}(\text{Mg}_{1/3}\text{Nb}_{2/3})\text{O}_3$  and  $\text{Pb}(\text{Sc}_{1/2}\text{Ta}_{1/2})\text{O}_3$ .

### Crystallographic Aspects of Ferroelectricity

The seven basic crystal structures can be divided into 32 point groups depending on crystal symmetry operations (e.g., inversion, mirror image, and rotation) [34]. Eleven point groups are centrosymmetric and the remaining 21 are non-centrosymmetric. A lack of center of symmetry is required for the presence of piezoelectricity in which the polarization is caused by a net displacement of the positive and negative ions with respect to each other. All non-centrosymmetric point groups, except cubic 432, show inherent asymmetric effects (i.e., piezoelectricity). The piezoelectric crystals are those which become polarized when stressed; conversely, when an electric field is applied, crystals become strained. Of the 20 piezoelectric classes of crystals, 10 have a unique polar axis where none of the symmetry operations of the crystal point provides an identical operation [38]. The existence of a polar axis in a crystal allows appearance of a spontaneous polarization by mutual interaction between the dipoles, and these materials are denoted

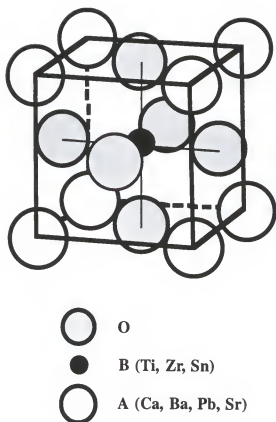


Figure 2-1. Crystal structure of the perovskite  $ABO_3$  unit cell.

pyroelectric. In the pyroelectric materials a change in temperature produces a change in the spontaneous polarization. A limited number of pyroelectric crystals exhibit the additional properties that the spontaneous polarization can be reoriented by applying an electric field, which defines ferroelectricity. Thus, all ferroelectrics are pyroelectric and piezoelectric. Similarly, all pyroelectrics are piezoelectric, but the reverse is not true. Relationships between these materials are shown in Figure 2-2.

### Structural Origin of the Ferroelectric State

The spontaneous alignment of dipoles which occurs at the onset of the ferroelectric state is associated with a crystallographic phase change from a centrosymmetric (i.e., paraelectric) to a noncentrosymmetric (i.e., ferroelectric) state [34].  $\text{BaTiO}_3$ , which was the first metal oxide ferroelectric to be discovered, is an excellent example to illustrate the structural considerations.  $\text{BaTiO}_3$  exhibits three ferroelectric phases as shown in Figure 2-3. The paraelectric, cubic (point group,  $m\bar{3}m$ ) phase transforms at approximately  $130^\circ\text{C}$  into a ferroelectric, tetragonal ( $4mm$ ) phase by the formation of a polar  $c$ -axis. At  $-5^\circ\text{C}$ , the unit cell converts into a ferroelectric, orthorhombic ( $mm2$ ) phase with the spontaneous polarization appearing along one of the  $[110]$  axes. Finally, the material changes structure into another ferroelectric, rhombohedral ( $3m$ ) state with the polar axes corresponding to one of the  $[111]$  directions. The  $\text{Ti}^{4+}$  ions in the perovskite  $\text{BaTiO}_3$  structure are surrounded by six oxygen ions in an octahedral configuration as shown in Figure 2-1. For cubic  $\text{BaTiO}_3$ , the thermal energy is sufficient to allow the  $\text{Ti}^{4+}$  atoms to move randomly around their central position, so there is no fixed asymmetry and thus no ferroelectricity. However, the open octahedral site in the paraelectric state allows the  $\text{Ti}^{4+}$  atoms to develop a large dipole moment in an applied field, giving rise to high dielectric constant. On cooling below the Curie temperature,  $\text{BaTiO}_3$  changes from cubic to tetragonal symmetry and is marked by the  $\text{Ti}^{4+}$  ion shift from the central to off-central position.

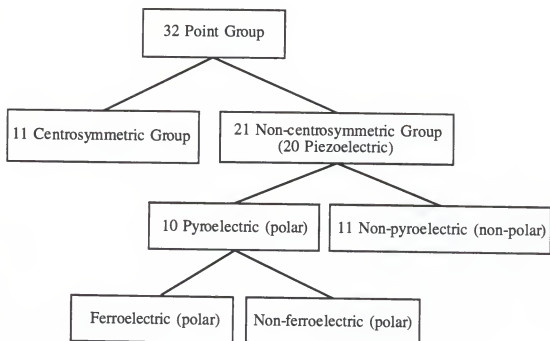


Figure 2-2. Interrelationship between piezoelectric, pyroelectric, and ferroelectric materials on the basis of crystal symmetry [38].

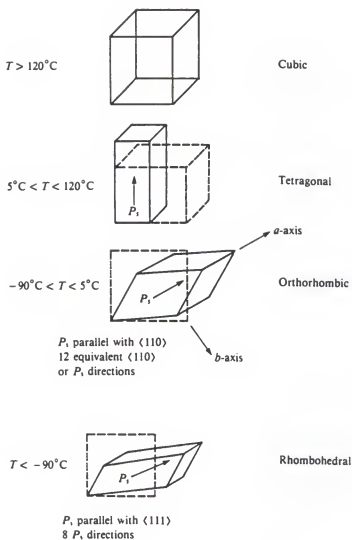


Figure 2-3. Crystallographic transformations in  $\text{BaTiO}_3$  [34].

The equilibrium position of the  $\text{Ti}^{4+}$  ion along the c-axis, depending upon the crystal structure, can be considered as a minimum energy state in the free energy diagram as shown in Figure 2-4 [39]. In the cubic phase, there is a single energy minimum occurring at the center of octahedra so that there is no net displacement compared to oxygen ion positions. In the case of the tetragonal phase, the energy curve exhibits two wells located at the off-centered positions so that a unilateral displacement of the positively charged  $\text{Ti}^{4+}$  against the negatively charged  $\text{O}^{2-}$  surroundings occurs. The result is a net permanent dipole in each octahedra. Furthermore, since distorted octahedra in the tetragonal structure are joined at their corners, not at edges or faces, additive coupling of the dipole moment associated with each octahedra is effective without canceling each other. The polarization direction can be readily reversed by applying an electric field in the opposite direction with sufficient strength to allow the energy for the  $\text{Ti}^{4+}$  ions to overcome the energy barrier between the two states.

An immediate consequence of the onset of spontaneous polarization in a material is the appearance of an apparent surface charge density and an accompanying depolarizing field ( $E_d$ ) as shown in Figure 2-5(a). The energy associated with the polarization in the depolarizing field is minimized by twinning, a process in which the crystal is divided into many oppositely polarized regions (i.e.,  $180^\circ$  domains) separated by a domain wall from a neighboring region of a different direction of polarization, as depicted in Figure 2-5(b) [39]. Thus the surface consists of a mosaic of areas carrying apparent charges of opposite sign, resulting in a reduction in  $E_d$  and in energy. The presence of a mechanical stress in a crystal also gives rise to the development of  $90^\circ$  domains configured so as to minimize the strain. Figure 2-6 shows  $90^\circ$  and  $180^\circ$  domain structures. The multi-domain state can be transformed into a single domain by applying a field parallel to one of the polar directions known as the poling process. However, it is usually inhibited by  $90^\circ$  domain switching while  $180^\circ$  domain switching can proceed to near completion. As a consequence, polycrystalline ferroelectric ceramics show lower saturation polarization when compared to

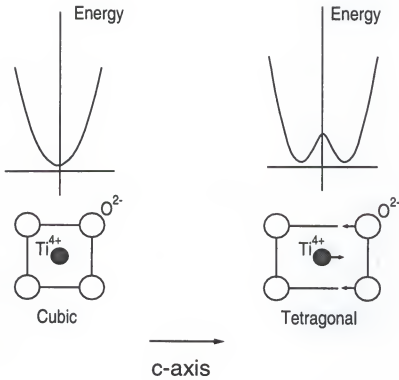


Figure 2-4. Free energy configurations as a function of  $\text{Ti}^{4+}$  position in cubic and tetragonal phases of  $\text{BaTiO}_3$ .

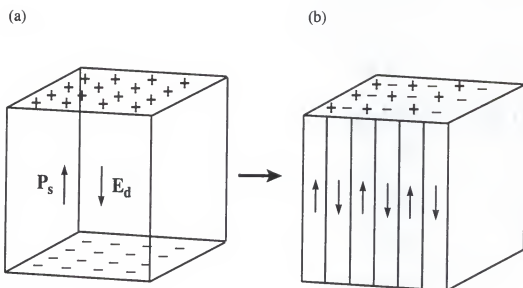


Figure 2-5. Domain structure development: (a) surface charge associated with spontaneous polarization; and (b) formation of  $180^\circ$  domains to minimize electrostatic energy [39].

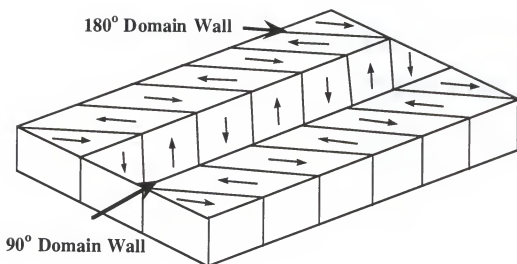


Figure 2-6. Schematic diagram of 180° and 90° domain structure in ferroelectrics [39].

their single crystal counterparts since the random directions of the crystallographic axes of the crystallites limit the extent to which spontaneous polarization can be developed.

The domain structure plays an important role in understanding ferroelectric materials [34, 40]. The ferroelectric hysteresis behavior results from a domain rotation and/or growth process. In Figure 2-7, a typical hysteresis loop and domain growth process under an applied field are illustrated. At low field strengths in an unpolarized ferroelectric material, the polarization ( $P$ ) is initially reversible and is nearly linear with the applied field ( $E$ ) (stage 1). At higher field strengths, the polarization increases considerably as a result of the rotation and growth of the ferroelectric domains (stage 2). At sufficient high field strengths, the change in polarization is small due to polarization saturation corresponding to nearly complete dipole alignment parallel with the applied field (stage 3). Extrapolation of the saturation curve to zero field gives the saturation polarization ( $P_s$ ). When the applied field continues to increase beyond the value required for saturation polarization, the polarization also continues to increase, albeit slowly and linearly with the field. It is because the individual  $[\text{TiO}_6]^{2-}$  polarizable units can be distorted continuously, thus, increasing the unit polarization. When the applied field is withdrawn, a finite polarization remains in the material, called the remnant polarization ( $P_r$ ) (stage 4). This is due to the inability of the oriented domains to return to the random state without an additional energy input. The strength of an oppositely directed field required to produce a zero net polarization is called the coercive field ( $E_c$ ).

#### Applications of Perovskite Ferroelectrics

Ferroelectric ceramics are widely used in many electronic and other devices [1, 36, 39]. This is because ferroelectric materials exhibit high dielectric constants, large piezoelectric coefficients and large pyroelectric coefficients. These materials can also show large nonlinearities with regard to dielectric behavior so that the permittivities and refractive indices are highly dependent on the applied electric field, leading to electro-optic

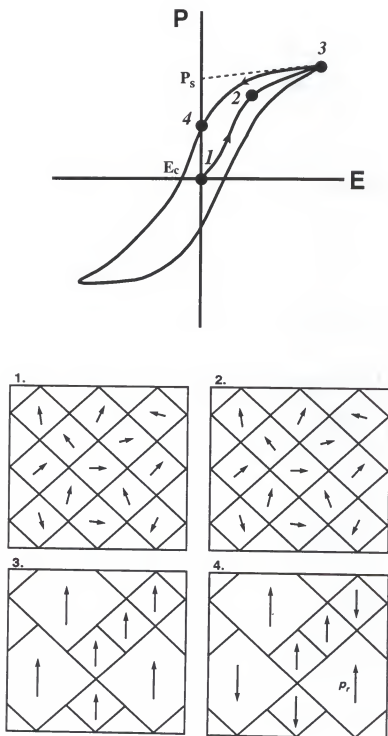


Figure 2-7. Hysteresis behavior of polarization as a function of the applied field and relevant domain rotation and growth process in the direction of an applied field ( $P_r$  is the remnant polarization) [34].

applications. Table 2-1 lists some of the applications of ferroelectrics and illustrates the evolution of materials over the last few decades.

One of the main applications of the ferroelectric ceramics includes dielectrics in the form of capacitors, for which the very high dielectric constants of the materials can very markedly reduce the volume required to achieve a given capacitance value. In particular, barium titanate is by far the most popular ferroelectric material, and is extensively used for multilayer ceramic (MLC) capacitors. The structure of the multilayer capacitor is schematically shown in Figure 2-8 [35]. Multilayer ceramic capacitors are generally manufactured by first making a green tape using a doctor blade technique starting from the doped-BaTiO<sub>3</sub>. Metals inks are then printed onto the tapes in the required patterns using a silk-screen process. The tapes are stacked together and consolidated under pressure, followed by dicing in a manner that the electrodes of successive layers are exposed at opposite end-faces, and by firing. The most important aspect in MLC processing relates to the electrode metal. Since the ceramic needs to be fired at about 1300°C in an oxidizing atmosphere, it is necessary to use noble metal electrodes, such as platinum or palladium, which are extremely expensive. Pd can be alloyed with silver, which is considerably cheaper. However, the melting point of this alloy decreases monotonically with the concentration of Ag, so that only 30 atomic % Ag can be included in the alloy. Another way to reduce the electrode cost is to use base metal such as Ni, Cu, or Fe. In this case, the sintering of the base metal capacitors should be performed in an inert atmosphere to prevent oxidation. Even when oxidized, under such a condition, only a small amount of base metal oxides can form and redissolve in BaTiO<sub>3</sub>, which acts as an electron acceptor compensating the charge of oxygen vacancies and subsequently reduces the semiconductivity of BaTiO<sub>3</sub> [41].

With the promise of higher dielectric constants and lower firing temperatures, and hence lower electrode cost, lead-based perovskite compositions (PbB<sup>(I)</sup>B<sup>(II)</sup>O<sub>3</sub>) have been studied [42]. Of particular interest are compositions in which B<sup>(I)</sup> is a divalent or trivalent

Table 2-1. Applications of Ferroelectrics since 1940 [35]

1940s	<i>Dielectric properties</i> Ceramic capacitors  <i>Piezoelectric properties</i> Underwater sonar (Rochelle salt, ADP)	1970s	<i>Pyroelectric properties</i> Intruder detection Fire alarms Thermal imaging  <i>Electro-optic properties</i> Large area shutters (transparent ceramics) Integrated optic devices Page composers  <i>Semiconducting properties</i> Self-stabilizing ovens Sensors
1950s	<i>Piezoelectric properties</i> Underwater sonar (Ceramic BaTiO <sub>3</sub> ) Phonograph pickups Gas Lighter Bulk wave filters  <i>Switching properties</i> Computer memories	1980s	<i>Pyroelectric properties</i> Multi-element arrays Solid state thermal imaging  <i>Electro-optic properties</i> Integrated optic modulators, switches, sensors Displays  <i>Switching properties</i> Memories (thin films)
1960s	<i>Piezoelectric properties</i> Surface acoustic wave devices Trapped energy filters Piezoelectric transformers  <i>Electro-optic properties</i> Bulk modulators Q switches		

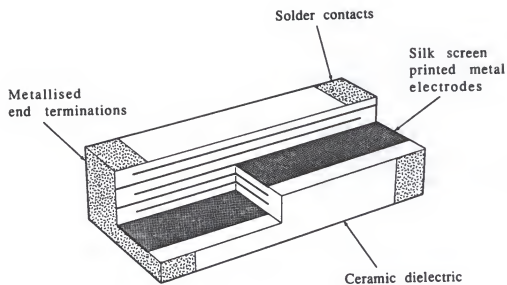


Figure 2-8. Structure of a multilayer capacitor [35].

cation such as  $\text{Mg}^{2+}$ ,  $\text{Zn}^{2+}$ ,  $\text{Ni}^{2+}$ , or  $\text{Fe}^{3+}$ , and  $\text{B}^{(\text{II})}$  is a high-valence ion such as  $\text{Nb}^{5+}$ ,  $\text{Ta}^{5+}$ , or  $\text{W}^{6+}$ . The most commonly studied material is  $\text{Pb}(\text{Mg}_{1/3}\text{Nb}_{2/3})\text{O}_3$  (PMN) which is known as a relaxor compound. These compounds exhibit a broad maximum in the dielectric constant, and the temperature of the dielectric maximum also increases with increasing frequency. The origin of this broad maximum is postulated to be caused by a distribution of the Curie points resulting from microcompositional fluctuation in the B-site cations (i.e., disordering) [43]. Another characteristic of relaxors is the frequency dispersion of the dielectric loss, which occurs at a slightly lower temperature than that of the normal ferroelectrics.

### Chemical Synthesis of Perovskite Ferroelectric Powders

Advanced ceramic materials offer a wide variety of physical and chemical characteristics. The performance of ceramics is essentially determined by the characteristics of the starting powders and the microstructure of the consolidated green body [16, 44]. Since ceramic products are usually formed by powder processing, typically starting with more than  $10^{12}$  particles per component, the properties of the sintered body are inherited from the characteristics of the initial powders [45]. Even careful forming and precise firing would not lead to the desired performance of the final products if inadequate raw materials are involved. This 'domino effect' is illustrated in Figure 2-9. Thus understanding and evaluating the properties of the starting powders are essential for improved control of the forming and firing operations. Ideal physicochemical characteristics of a ceramic powder include a submicron particle size, controlled particle size distribution, uniform and equiaxed shape, minimum degree of agglomeration, high degree of chemical purity, and controlled chemical and phase homogeneity [46]. In this regard, proper powder preparation methods are imperative for the reliable and reproducible production of advanced ceramics, especially ferroelectric ceramics. Extensive efforts have been employed to develop a new particle synthesis approach which leads to production of such powders. The fundamentals of

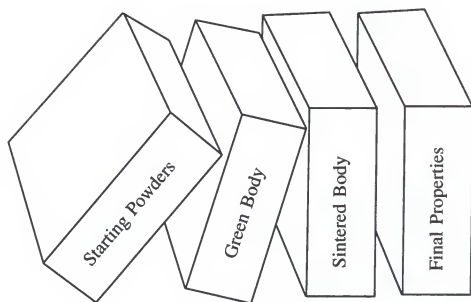


Figure 2-9. Domino effect in ceramic processing: the role of the starting powders [45].

powder materials including physical and chemical properties and characterization techniques of particulate materials, will be discussed, followed by descriptions of various chemical synthesis methods for ferroelectric ceramics.

### Definition of Particulate Materials

A particle can be defined as a small, discrete unit of solid matter that can be isolated from other similar units [47]. If the particle cannot be subdivided further, it is called a primary particle. A primary particle can be either a single crystal or polycrystalline as schematically shown in Figure 2-10. If, on the other hand, the particle has subdivisions including a network of interconnective pores, it is called an agglomerated particle. Primary particles do not always behave independently, but tend to behave as a group, i.e., in a unit larger than individual particles with decreasing particle size. Smaller particles have a greater probability of forming agglomerates because of the increased adhesion strength (i.e., van der Waals force) among particles, giving rise to a variety of undesirable properties including poor flowability. Agglomerated particles are also usually deleterious in obtaining uniform and dense ceramic products, but large agglomerates, granules, may be intentionally prepared to promote flowability for effective packing in a powder pressing processes.

### Properties and Characterization of Powders

Properties of ceramic powders can be classified into physical and chemical properties as summarized in Table 2-2 [48]. The most important physical properties include particle size distribution, particle morphology, surface area, and the state of agglomeration. These properties determine how well a powder can be packed during green body formation and eventually have an impact on sintering behavior. For example, powders containing hard agglomerates (those that do not break down during green body formation) are undesirable because they can lead to differential sintering that results in

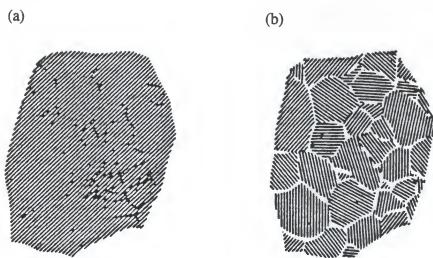


Figure 2-10. Structure of primary particle: (a) single crystal; and (b) polycrystalline [45].

Table 2-2. Characteristics of Ceramic Starting Powders [48]

Physical Characteristics	Chemical Characteristics
Primary particles	Bulk Chemical Composition
Size	Major element concentration
Shape	Minor impurities (10 ppm-1%)
Distribution of size and shape	Trace elements (<10 ppm)
	Composition of impurities
Agglomerates (secondary particles)	Crystal structure
Size	Crystallinity
Shape	Lattice constant
Porosity	Defects
Amount	
Size	Phase Composition
Shape	Crystalline phase
Density	Quantity
Specific surface area	Identification
Permeability	
Flowability	Surface composition
	Major elements
	Minor elements
	Trace elements
	Inorganic species
	Organic species
	Structural water

nonuniform microstructures and reduced densities [44].

There are numerous commercial instruments available for determining particle size distributions as presented in Table 2-3. The instruments utilize sizing techniques that are based on a variety of principles, including sedimentation, light scattering, electrical sensing, image analysis of electron micrographs, and hydrodynamic sieving. However, most determinations are performed on particles dispersed in a solution phase, so that the resulting data may not necessarily represent the actual particle state. The method of dispersion and conditions of the measurement may also significantly modify the results. Therefore the principles and assumptions underlying each instrument must be fully understood before choosing the appropriate method and interpreting the data obtained.

X-ray diffraction line broadening is often used to determine the average crystallite size ( $D$ ) of the particles based on the Scherrer formula[49]:

$$D = \frac{K\lambda}{B\cos\theta_B} \quad [2.1]$$

where  $B$  is a width at the full half maximum intensity,  $\lambda$  is the wavelength of X-ray,  $K$  is the shape factor, and  $\theta_B$  is the Bragg angle. It is applicable when crystallite sizes are less than 100 nm. Direct observation of particles with microscopes such as scanning electron microscopy (SEM) and transmission electron microscopy (TEM) often provides detailed information concerning particle size and shape. The characterization of powder agglomeration properties is much less standardized. Pore sizes in the range of ~1 - 100 nm associated within the agglomerate, including specific surface area information, can be determined by analysis of multipoint BET gas adsorption-desorption isotherms. Mercury intrusion porosimetry is also used in pore size determination for pores ranging from 2 nm to larger than 1000  $\mu\text{m}$ . However, this method is only applicable to powders that contain agglomerates or a green body that can withstand maximum intrusion pressures near 400 MPa.

Table 2-4 lists the analytical methods for determination of the chemical characteristics of powders. Analysis of impurities is important, as contaminants are

Table 2-3. Particle Size Analysis Methods and Size Ranges [48]

Method	Nominal particle size (μm)	Measurement parameter
<i>Coarse particles &gt; 10μm</i>		
Sieving		
Dry	>10	Geometric
Wet	>2	
<i>Fine particles &lt; 10μm</i>		
Field scanning		
Optical microscopy	0.5 - 1000	Image
Electron microscopy	0.01 - 10	
Gravity sedimentation		
Pipette	1 - 100	Stokes
Photoextinction	0.5 - 100	
X-ray Absorption	0.1 - 130	
Radiation scattering		
Laser scattering	0.03 - 900	Geometric
Stream scanning		
Resistivity	0.05 - 500	Dynamic/Stokes
Optical	1 - 500	
Ultrasonic attenuation	100 - 1000	
Column hydrodynamic chromatography	0.1 - 1.0	
Sedimentation field flow fractionation	0.01 - 1.0	
Laser Doppler velocimetry	0.01 - 3.0	
Centrifugal sedimentation		
Photoextinction	0.05 - 100	Dynamic/Stokes
Mass accumulation	0.05 - 25	
X-ray absorption	0.1 - 5	

Table 2-4. Analytical Methods for Determination of Chemical Characteristics [45]

---

Element Analysis	
<i>Major</i>	Wet chemistry, Gas analysis, Flame emission spectroscopy X-ray fluorescence
<i>Minor/trace</i>	Emission spectroscopy, Mass spectroscopy Atomic absorption spectroscopy, Ion chromatography Neutron activation analysis
<i>Small area</i>	Analytical electron microscope, Electron probe microanalyzer Electron energy loss spectroscopy, Ion microanalysis Energy dispersive X-ray spectroscopy
Surface Analysis	Auger electron spectroscopy Secondary ion mass spectroscopy X-ray photoelectron spectroscopy Rutherford backscattering spectroscopy
Phase Analysis	X-ray diffraction
Structure Analysis	Scanning electron microscopy Transmission electron microscopy Scanning transmission electron microscopy Electron/neutron diffraction, X-ray diffraction
Surface Charge	Electrophoretic method, Potentiometric titration

---

responsible for the physical properties of ceramic products as well as modifications in sintering behavior. An appropriate analytical method should be used, with regard to both the amount and the type of chemical species. Usually several techniques are utilized to supplement one another. The quantitative analysis of major components is performed via classical wet chemistry methods such as volumetric and gravimetric analyses. Trace amounts of constituents can be detected by spectroscopic techniques such as arc, spark, or inductive coupled plasma (ICP) emission, and atomic absorption. In most cases, specimens must be dissolved, by means of acids or fluxes to provide the required solution phase. Analytical electron or X-ray spectroscopy provides useful information on the chemical bonding states of each element and the composition of a material with high accuracy.

Crystal structure is studied by X-ray, electron and neutron diffraction. Infrared and Raman spectroscopies are used to investigate the surface characteristics of powders in air. The determination of the surface properties of powders suspended in solution is also important in a number of areas of ceramic processing, such as slip casting and injection molding, to understand and to control the dispersion of particle suspensions. The surface charge developed on particles in a liquid medium is usually characterized by an electrophoretic method in which the velocity of the moving particles is measured under an applied field.

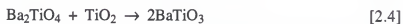
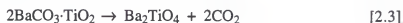
### Powder Synthesis Techniques

In this section, various chemical solution synthesis methods will be described in detail using  $\text{BaTiO}_3$  as the material of interest.

#### Solid-state reactions method

Conventional synthesis routes for ferroelectric ceramics involve solid-state reactions of mechanically mixed, separate metal oxide and/or carbonates above  $1200^\circ\text{C}$  and subsequent milling to reduce agglomerates. Solid-state reaction may proceed through

several intermediate steps. For instance, in the preparation of conventionally derived  $\text{BaTiO}_3$ , the following reactions between  $\text{TiO}_2$  (rutile or anatase) and  $\text{BaCO}_3$  are possible [50]:

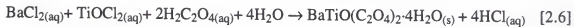
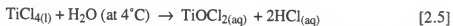


It is difficult to produce phase-pure multicomponent powders without undesirable intermediate phases unless reaction mechanisms and rate controlling steps are fully understood. High temperature calcination tends to produce chemical inhomogeneities in the solid products due to volatilization of the components, especially lead species. Furthermore, the milling process not only produces asymmetric particles, but also introduces impurities from the milling media. In this respect, the importance of chemically derived uniform multicomponent ferroelectric submicron powders is more easily appreciated. Atomic mixing, inherent to chemically derived powders, avoids the large concentration gradients present in conventionally processed systems and facilitates precise and uniform compositional control of major and minor powder constituents.

#### Precipitation/calcination method with metal salts

Coprecipitation commonly involves the addition of a precipitating agent to a solution of soluble metal salts to form a sparingly soluble metal hydrous oxide or salt. Precipitation often takes places at a faster rate than the time required for mixing of the reagents. For example,  $\text{La}(\text{NO}_3)_3$ ,  $\text{ZrOCl}_3$ ,  $\text{TiCl}_4$  and  $\text{H}_2\text{O}_2$  are dissolved in water at  $40^\circ\text{C}$  in the preparation of PLZT,  $\text{Pb}(\text{NO}_3)_2$  [51]. Precipitation is induced by the addition of  $\text{NH}_4\text{OH}$  to this solution to maintain a pH of  $\sim 9$ . The precipitate, a mixture of various hydroxides, is filtered from suspension, washed free of soluble species with hot distilled water, and dried at  $100^\circ\text{C}$ . Calcination at a temperature of  $650^\circ\text{C}$  is necessary to form the metal oxides, followed by subsequent milling to break up aggregates formed during precipitation and calcination.

The common ion effect and different precipitate solubilities are factors that can lead to chemical and phase heterogeneities in coprecipitated materials [46]. The common ion effect can cause solution homogeneity problems in a multicomponent solution when one of the soluble salts has an anion that renders one of the components insoluble. Different solubilities of the various precipitating phases affect the precipitation kinetics of each component, causing the stoichiometry of the precipitate to vary with reaction time. In the coprecipitation of BaTiO<sub>3</sub> from inorganic salt solution, the rapid condensation reactions between Ti-OH groups in an alkaline medium involve the growth of TiO<sub>2</sub>·xH<sub>2</sub>O dense particles, resulting in a mixture of separate TiO<sub>2</sub> and BaCO<sub>3</sub> [30]. To minimize segregation during coprecipitation and optimize control of the stoichiometry, complex multicomponent salts such as oxalates of fixed stoichiometry can be precipitated. Stoichiometric Ba-Ti oxalate complexes can be produced as follows:



Transformation of such complex coprecipitates into the desired final products usually involves heat treatment of the intermediates, similar to the conventional solid state reaction process [52]. The proposed models for BaTiO(C<sub>2</sub>O<sub>4</sub>)<sub>2</sub>·4H<sub>2</sub>O include a nanosized crystallite mixture model consisting of BaCO<sub>3</sub> and TiO<sub>2</sub> and an amorphous-like structure model in which Ba<sup>2+</sup> is incorporated in a Ti-O-Ti polymer network [53]. It was determined that oxalate ligands provide an atomic level contact between the metal ions thus resulting in enhanced transformation, and prevent formation of other crystalline phases such as Ba<sub>2</sub>TiO<sub>4</sub> or BaTi<sub>2</sub>O<sub>5</sub>. In the synthesis of nonstoichiometric oxides such as Sr<sub>0.33</sub>Ba<sub>0.65</sub>TiO<sub>3</sub>, multicomponent oxalates can be used. However, there is no guarantee that initial solution composition corresponds to that of the oxalate precipitates as the number of cations involved is increased. To form an oxalate precipitate with the desired stoichiometry, for example, Saegusa et al. have shown that the reaction of soluble (NH<sub>4</sub>)<sub>2</sub>TiO(C<sub>2</sub>O<sub>4</sub>)<sub>2</sub> with lead and barium acetate solutions allows an ion exchange between

the ammonia ion and metal ions, and produces the Ba-Pb-Ti oxalate precipitates [54].

Another undesirable effect is coprecipitated anion impurities (e.g., nitrates, chlorides, and sulfates). These impurities can be incorporated into the particles as lattice defects or can adsorb onto powder surfaces. In addition, soluble species in solution can be retained within agglomerates of the particles. While such impurities are difficult to remove with a washing process, failure to remove these ions may adversely affect the later stages of ceramic processing such as sintering or the final material performance.

#### Metal alkoxide decomposition methods

Anion contamination problems can be avoided with the use of anionless precursors such as metal alkoxides, which are organo-metallic compounds with the general formula  $M^{z+}(OR)_z$ , where M is a metal, z is the valence state of the metal, R is an alkyl group ( $C_mH_{2m+1}$ ), and m is an integer [55]. Metal alkoxides react with water to precipitate ceramic polymers by hydrolysis and condensation within the liquid phase. The OR group in the metal alkoxide is a strong Lewis base, undergoing hydrolysis to form hydrous metal oxides (e.g.,  $MO_2 \cdot xH_2O$ ), hydrates (e.g.,  $MO(OH)$  or  $M(OH)_2$ ), or transparent gels by polymerization (the sol-gel process), depending upon reaction conditions and the characteristics of the metal species.

Powders can be synthesized starting from either the single metal alkoxides or the mixed metal salts and metal alkoxide through thermal decomposition. It was determined that the reaction pathway of the gel-to-powder conversion depends on the hydrolysis content, aging condition, and drying temperature. Various transformation mechanisms such as the thermally activated collapse of the amorphous gel structure, direct crystallization, or the presence of reactive intermediate phases have been proposed [11]. For example,  $BaTiO_3$  can be prepared in various ways from the metal alkoxides [28, 30]. First, a mixture of barium and titanium alkoxides in an alcohol solution is simultaneously hydrolyzed with the addition of  $H_2O$  [56]. Secondly, hydrolysis of the titanium alkoxide in an aqueous solution of either  $Ba(OH)_2$  or  $Ba(CH_3COO)_2$  in alkaline conditions produces

the precipitates which transform into crystalline cubic  $\text{BaTiO}_3$  during further heat treatment [24]. Crystalline  $\text{BaTiO}_3$  can also be directly precipitated by hydrolyzing either titanium isopropoxide in an aqueous solution of  $\text{Ba}(\text{OH})_2$  [57] or single crystal of the barium-titanium double alkoxide complex at elevated temperatures [58]. These reactions must be performed in a moisture-free and  $\text{CO}_2$ -free atmosphere to prevent premature hydrolysis of the alkoxides and  $\text{BaCO}_3$  formation, respectively.

The sol-gel method can lead to production of ultrafine multicomponent powders (usually  $< 0.1 \mu\text{m}$ ) with high purity, homogeneity, increased sinterability and reproducibility. However, alkoxide precursors are expensive and extremely sensitive to moisture, heat, and light [55]. Similar to solid state reactions and the coprecipitation method, the calcination step, required to induce crystallization, remove residual carbon, and cause a phase transformation, usually also increases the possibility for contamination and the loss of volatile species. Furthermore, hydrolyzing a mixture of alkoxides that do not have reasonably compatible hydrolysis reaction rates with one another results in preferential precipitation of a more reactive alkoxide. In this case, double or triple complex alkoxide precursors are often necessary.

#### Polymeric metal organic-gel method (Pechini process)

Polymeric metal organic precursors prepared from water-soluble metallic salts of polyfunctional acids are useful in the production of multicomponent ceramics. Typically,  $\alpha$ -hydroxy acids (e.g., hydroxybutyric acid and citric acid) and/or  $\alpha,\beta$ -unsaturated acids (e.g., maleic acid and acrylic acid) are mixed with metal salts to form a uniform solution of metal cation complexes [46]. The clear solution can be dehydrated to yield an amorphous solid precursor which subsequently forms the desired compounds after firing at elevated temperature. Ethylenediaminetetraacetic acid (EDTA) can also be used as a strong complexing agent for the metal species.

In the Pechini process, also known as the liquid mix technique, chemical complexation of metal salts is accomplished with hydroxycarboxylic acids to form a

homogeneous aqueous solution [59]. Subsequently, a polyhydroxyl alcohol (usually ethylene glycol) is introduced, and the solution is heated to approximately 80°C to achieve homogeneity. As the temperature increases above 80°C, the alcohol esterifies the complexed and uncomplexed carboxylic acid and generates water. Since both the acid and alcohol are polyfunctional, cross-linking can occur, and an organic polymer network is established with the chelated cations atomically distributed along the backbone. Upon removal of the water, a resin is formed that yields an oxide when calcined at temperatures ranging from 500 to 900°C.

#### Precipitation from homogeneous solution (PFHS)

Precise control of physical powder characteristics requires uniform supersaturation in solution [60, 61]. When this is achieved, nucleation precedes growth and aging, and these latter processes occur uniformly throughout the reaction medium. The PFHS utilizes chemical reactions with rate kinetics which control the release of reaction species. In order to obtain a phase homogeneous powder with the intended cation stoichiometry, careful attention must be paid to the preparation of a homogeneous solution and the types of multicomponent metal complexes formed. For example, stable aqueous solutions of titanium and barium complexes can form via chelation with EDTA. Depending upon aging at 60°C for 2 hours in the presence of  $\text{H}_2\text{O}_2$ , decomposition of these metal chelates results in a controlled release of  $\text{Ba}^{2+}$  and  $\text{Ti}(\text{O}_2)(\text{OH})_4^{2-}$ , which eventually leads to homogeneous nucleation of amorphous spherical  $\text{BaTiO}_3$  particles with a narrow size distribution in an alkaline media [62, 63]. In non-aqueous media, controlled hydrolysis of metal alkoxides with dilute alcoholic solutions can also provide a simple means of synthesizing a spherical monodisperse powder.

For PFHS, however, precipitation must occur at a concentration typically less than 0.05 M and at a pH near the solubility minimum of the precipitate. At high concentrations, increased morphology variation and agglomeration results. These phenomena sometimes limit the applicability of this technology.

### Hydrothermal synthesis

Hydrothermal particle synthesis involves the treatment of aqueous homogeneous solutions or suspensions of precursors at elevated temperature and pressure [64]. Pressure is required to maintain a solution phase at an elevated temperature, so that diffusion coefficients are greater than those found in solid state reactions, promoting rapid phase transformations. The combined effect of pressure and temperature can also reduce energies for various equilibria-stabilizing phases that might not be stable under atmospheric conditions. Therefore, hydrothermal synthesis is fundamentally a solution process rather than a solid state reaction, in which the solution chemistry plays an important role in the formation of particles.

Hydrothermal synthesis is a potentially superior method for the low-cost and low-temperature production of ceramic powders, especially for multicomponent electronic ceramics as compared to other chemical processes, such as the metal alkoxide decomposition and coprecipitation processes [19]. The major advantage of this method is the direct production of anhydrous crystalline metal oxides without a calcination step that invariably produces agglomeration. Another advantage includes the use of relatively inexpensive raw materials such as oxides, hydroxides, chlorides and nitrates in contrast to relatively expensive starting materials such as the alkoxides. It is possible to produce crystalline powders with controlled particle size, controlled stoichiometry, and in some cases controlled particle shape [65]. Powders produced by this method have been demonstrated to be highly reactive towards sintering [15].

Although the relatively high temperatures and pressures (e.g., 100-500°C and 0.1-14 MPa) prohibit in most cases the use of *in-situ* systems to monitor the course of reactions, possible formation mechanisms for the hydrothermal reactions are considered to occur by either *in-situ* gel transformation by the removal of structural water, or dissolution of the precursors followed by reprecipitation, depending upon the precursor characteristics [27, 31]. The former mechanism can be obtained in a dispersion when suspended particles

undergo a polymeric or chemical phase transformation. For instance, titanium hydrous gel can be transformed into polycrystalline anhydrous anatase spheres by aging in an alkaline media at 100°C. A dissolution-precipitation mechanism plays a role when suspended particles dissolve into solution, supersaturate the solution phase, and subsequently precipitate particles from homogeneous solution [46]. Uniform particles are produced by a short nucleation time followed by particle growth, similar to PFHS. In most cases, however, the suspended solids are not very soluble in water, so that solubilizing components (mineralizers) such as acids, bases, or other complex-forming substances must be added.

#### Molten salt synthesis

Molten salt synthesis is a suitable method for the preparation of complex oxide powders with shape anisotropy [66]. A mixture of reactant oxides or carbonates is heated with mixed salts such as KCl-NaCl above the melting point. The molten salt acts as an inert reaction aid or medium. Since the solubilities of the starting reactant and product oxides in salt melts are usually quite small, liquid and solid phases coexist during the process. The liquid phase accelerates formation of the complex oxide and its particles grow due to enhanced mass transport rates. Particle shape depends on the relative dissolution characteristics of the individual components into the molten salt. When one reactant dissolves faster than another, the reaction product precipitates on the surface of the slower dissolving component. Uni-directional diffusion of the more soluble component through the product layer carries the process to completion, resulting in a particle with a morphology reflective of the more slowly dissolving component. When the reactants have comparable dissolution rates, on the other hand, the metal oxide formation takes place somewhere in the molten salt, producing either well-defined or lumpy particles depending upon the degree of interaction between the product and salt. To produce anisotropically shaped particles in such a case, an anisotropically shaped reactant oxide is necessary to convert to a complex oxide, causing preservation of the starting material shape. For

instance, needle-like  $\text{BaTiO}_3$  has been synthesized by the reaction between needle-like  $\text{TiO}_2 \cdot n\text{H}_2\text{O}$  and  $\text{BaCO}_3$  at  $700^\circ\text{C}$  for 1 hr in a chloride bath [12].

#### Pyrolysis method

Pyrolysis processes form a ceramic powder by solid state decomposition of a solid or molten precursor (typically a molecular or polymeric compound) in the presence of an inert (e.g., vacuum or argon) or reactive (e.g., oxygen) atmosphere [46]. Mechanistic studies of the decomposition and its interaction with the processing variables are essential to control the characteristics of the pyrolysis product. For example, agglomeration and excessive crystallite growth can result from excessive exothermic decomposition. Decomposition residue (e.g., carbon) can be a result of several factors such as poor choice and control of pyrolysis atmosphere, improper gas flow rates, and furnace design.

Metal-organic molecular compounds such as carboxylates are useful materials for preparing multicomponent oxides. Neodecanoate salts of various metals form uniform solutions in xylene. These solutions can be pyrolyzed to form submicron powders. For instance,  $\text{BaTiO}_3$  can be prepared from a solution of dimethoxytitanium dineodecanoate  $((\text{CH}_3\text{O})_2\text{Ti}(\text{C}_9\text{H}_{19}\text{COO})_2)$  and barium neodecanoate  $(\text{Ba}(\text{C}_9\text{H}_{19}\text{COO})_2)$  by pyrolyzing at temperatures of approximately  $600^\circ\text{C}$  [67, 68].

Salient features of each chemical solution synthesis method have been described using  $\text{BaTiO}_3$  as the material of interest. References [69-90] for solution synthesis of other ferroelectric ceramics including  $\text{PbTiO}_3$ , PZT and PMN are presented in Table 2-5.

#### Mechanisms of Precipitation Process from Solution Phase

As described previously, hydrothermal reactions are sometimes referred to as PFHS systems since uniform solutions of aqueous complexes can form under elevated temperature and pressure conditions to precipitate ceramic powders. To better understand particle formation mechanisms and control particle characteristics during hydrothermal

Table 2-5. Summarized References for Chemical Derived Perovskite Ferroelectrics Powders

Materials	Solid-state reaction	Coprecipitation /Oxalates	Alkoxide-salts	Sol-gel	PFHS	Hydrothermal	Molten salt
PbTiO <sub>3</sub>	69	70, 72	72	73	74	75 - 77	78
PZT	69	78 - 81	72	82, 83		84 - 86	87
PMN	42, 69, 88, 89			90			91

synthesis, it is worth while to examine the fundamental aspects of the precipitation process. In this section, theoretical nucleation and growth theories including physical growth mechanisms for monodisperse particle formation are provided.

### General Aspects of Precipitation Processes

Precipitation of a particle from solution proceeds through various stages each of which is different in nature and very different in kinetics as follows: (i) formation of the solutes in solution phase; (ii) nucleation and growth of isolated primary particles; (iii) aggregation of the primary particles; (iv) ripening or aging of a stable crystal [91-95]. Each stage in the precipitation process does not necessarily follow the above order. Several stages can occur simultaneously and some stages may persist throughout the process.

Once nucleation occurs, the rate of nucleation rapidly increases and the precipitation process becomes uncontrolled. The kinetics of precipitation can then be divided into two stages - formation of the crystal nuclei and crystal growth. Nucleation can be either homogeneous, which occurs in the absence of a pre-existing solid surface, or heterogeneous, which may be initiated on any foreign surface. If the nucleation occurs in the presence of a growing solid surface, this process is called secondary nucleation. The properties and characteristics of precipitates depend on the rates and mechanism of the prevalent precipitation processes, but how and when one or the other of the processes become rate controlling depend on the experimental conditions under which precipitation is conducted. For example, the number of particles and the size distribution of particles are influenced by the mechanism and relative rates of these precipitation processes, and are basically a function of the supersaturation and time. Unless well-controlled methods to manipulate the overall processes of precipitation by physical or chemical ways are employed, polydisperse particles are produced.

### Definition and Driving Force of Precipitation

Precipitation is defined as a process in which a new phase is formed as a result of a chemical reaction of two or more components in solution [94]. A solid phase is precipitated if the chemical potential of the solid phase is less than that of the dissolved components to be precipitated from solution. A solution in which the chemical potential of the dissolved component is the same as that of the corresponding solid phase is in equilibrium with the solid phase under the given conditions and is termed a saturated solution. This equilibrium state is defined by the concentration of the dissolved components in the saturated solution at a given temperature, i.e., by the solubility. In order for precipitation to proceed, the concentration of the solution ( $C$ ) must be greater than the corresponding equilibrium concentration ( $C_o$ ). This excess concentration, which is the driving force for precipitation, is called the supersaturation ( $\Delta C$ ). The ratio of the bulk concentration to the saturated concentration is also called the supersaturation ratio ( $S = C/C_o$ ). For a saturated solution, the supersaturation ratio is greater than 1. The relative supersaturation ( $\sigma$ ) can be also defined as

$$\sigma = \frac{C - C_o}{C_o} = \frac{C}{C_o} - 1 = S - 1 \quad [2.7]$$

In the non-ideal solution case, the driving force for precipitation is the chemical potential difference ( $\Delta\mu$ ). Since  $\mu = \mu_o + RT \ln a$ , where  $\mu_o$  is the chemical potential of the standard state and  $a$  is the activity,  $\Delta\mu = RT \ln (a/a_o) = RT \ln S$  [95].

### Nucleation Theory

When the supersaturation is created by a chemical reaction, the solution becomes unstable. The system attempts to achieve thermodynamic equilibrium through nucleation and growth. More details concerning nucleation process are provided in this section, followed by description of various growth theories.

### Classical theory

The homogeneous nucleus is conceived as an aggregate (cluster) of critical size, which is unstable in a supersaturated solution [96, 97]. At a concentration below some critical level the cluster grows or dissolves reversibly, while irreversible growth ensues by accretion of an additional ion or molecule at the critical concentration. An intrinsic assumption of such theory is that macroscopic properties such as surface tension can be assigned to the nucleus. The energetics of nucleation include the formation energy for the cluster and creation of its surface area. Thus, the formation free energy ( $\Delta G_f$ ) for a spherical cluster with a radius of  $r$  can be represented as

$$\Delta G_f = \frac{4}{3}\pi r^3 \Delta G_v + 4\pi r^2 \gamma^2 \quad [2.8]$$

where  $\gamma$  is the solid-liquid interfacial energy and  $\Delta G_v$  is the volume free energy. According to the Gibbs-Kelvin equation,  $\Delta G_v$  can be related to the supersaturation as follows:

$$\Delta G_v = \frac{\Delta\mu}{V_m} = \frac{\rho}{M} RT \ln S \quad [2.9]$$

where  $\rho$  is the density of the solid phase,  $M$  is the molecular weight, and  $V_m$  is the molecular volume. The critical size of the cluster ( $r^*$ ) is determined by minimizing the free energy of formation with respect to the radius:

$$r^* = -\frac{2\gamma}{\Delta G_v} = -\frac{2\gamma V_m}{kT \ln S} \quad [2.10]$$

where  $k$  is the Boltzmann constant. For the critical size cluster, the free energy of formation is thus:

$$\Delta G_f^* = \frac{16\pi\gamma^3 V_m^2}{3(kT \ln S)^2} \quad [2.11]$$

By assuming that the rate of forming critical size clusters has an Arrhenius form similar to chemical reaction kinetics, the rate of nucleation is given by:

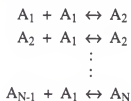
$$J = K \exp\left[-\frac{\Delta G_f^*}{kT}\right] = K \exp\left[-\frac{16\pi\gamma^3 V_m^2}{3k^3 T^3 (\ln S)^2}\right] \quad [2.12]$$

where  $K$  is the constant which relates to a diffusional energy barrier and jump frequency. Once a critical supersaturation is attained, an exponential burst of nucleation occurs. The

nucleation rate increases with increasing supersaturation and temperature, and decreases with an increase in surface energy.

### Kinetic theory

A kinetic theory of nucleation in a supersaturated solution, which does not employ the macroscopic concept of interfacial tension, but rather is based on molecular interactions, was recently developed [98-100]. This model assumes the formation of a cluster involving  $N$  atoms results from step-wise atomic or molecule collisions:



As a cluster attains the critical size, i.e., consists of  $N$  atoms, further growth to macroscopic size is allowed. If a critical size is not attained, the cluster eventually dissolves into the solution. Therefore, dynamic equilibrium between the rates of growth and dissolution is achieved in a given system. In this context, nucleation and growth reactions can be represented as follows:



Assuming a square-well interaction potential between a molecule and cluster, general equations were derived for (i) the rate of dissociation of molecules from the cluster, (ii) the radius of the critical cluster, and (iii) the rate of nucleation. For a pseudo-steady state, the net nucleation rate can be expressed:

$$J = \frac{f(1)n(1)}{1 + \sum_N \prod_{i=1}^N \frac{b(i)}{f(i)}} \quad [2.13]$$

where  $f(i)$  is the rate that a cluster containing  $i$  molecules grows to  $i+1$  molecules,  $b(i)$  is the rate that a cluster containing  $i$  molecules loses a molecule,  $n(i)$  is the concentration of such a cluster, and  $I$  is a sufficiently large number [101].

#### 2.4.4. Growth Theory

Crystal growth from solution occurs by a series of consecutive steps: transport of the solvated solute by bulk diffusion, surface adsorption at the solid-solution interface, surface diffusion to energetically favorable sites such as a step or kink, and finally integration into the crystal lattice by chemical reaction [95]. The rate of crystal growth is controlled by the slowest of these processes. The solute must be desolvated prior to the incorporation step, and the solvent must counter-diffuse away from the surface. In addition, the solute can be a variety of units such as atoms, molecules, ions, dimers, trimers, and polymers with different degrees of solvation and exhibiting different structures. Diffusion processes for crystal growth are strongly influenced by the type and molecular structure of the diffusing species. However, little is yet known about these solution species.

Two extreme cases of complex crystal growth are mass-transfer controlled and surface-reaction controlled depending upon the system, state of flow, and supersaturation. There exists an adsorbed layer of the solute on the surface of a growing crystal. Although the exact nature is yet to be determined, it is believed that the layer consists of partially ordered solute clusters formed in supersaturated solution, as shown in Figure 2-11 [102]. If this adsorbed layer is sufficiently thick, growth can be controlled by diffusion of the solute through this boundary layer rather than bulk transportation. Growth rate can be represented by the simple mass transfer equation (i.e., Fick's law). The mass ( $M$ ) flux density directed towards crystal surface due to the solute concentration gradient is

$$\frac{dM}{dt} = \frac{D}{\delta} A(C - C_o) \quad [2.14]$$

where  $D$  is a diffusion coefficient,  $\delta$  is a diffusion boundary thickness,  $A$  is the surface area of the crystal, and  $C - C_o$  is the supersaturation. If the growth rate ( $G$ ) is considered in terms of characteristic dimension  $L$  of the crystal rather than mass, the above equation is reduced to

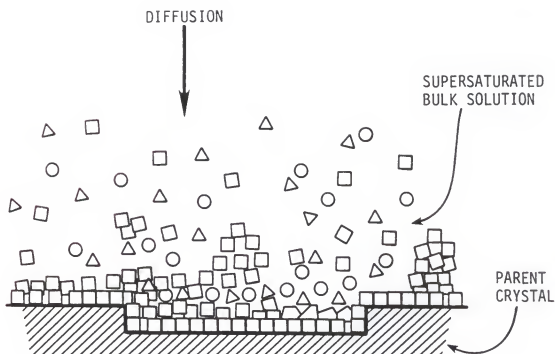


Figure 2-11. Adsorbed layer of the solute on the surface of a growing crystal [102]. The square, sphere, and triangle represent the crystal AB, hydrated cation  $A^+$ , and hydrated anion  $B^-$ , respectively.

$$G = \frac{dL}{dt} = K_1(C - C_o) = K_1S \quad [2.15]$$

The thickness of the absorbed layer is related to the relative rates of diffusion and surface integration. In many non-agitated systems, diffusion-limited growth is indeed the rate controlling mechanism. Under such conditions, the crystal growth rate increases and reaches a maximum as the velocity of supersaturated solution (i.e., stirring rate) is increased. With a further increase in the velocity, the growth rate remains constant, at which point, a surface reaction controls crystal growth. If diffusion of the solute takes place rapidly and the diffusion boundary layer is relatively thin, the growth is determined by the incorporation reaction at the crystal surface. There are many theories describing the actual integration step, which are presented in detail in the following sections.

#### Continuous growth model

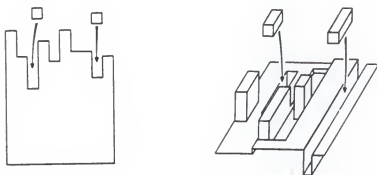
In the simplest case, the crystal surface is assumed to be rough on the atomic scale so that the growth unit is easily and continuously integrated at a site of the lowest energy such as a kink, as shown in Figure 2-12(a). Under this condition, the growth rate can be represented as the same equation of [2.15].

#### Two-dimensional nucleation and growth theory

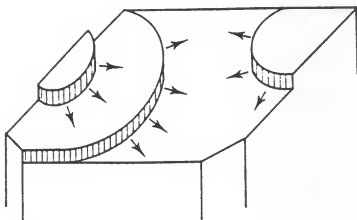
When crystals have no defects and perfectly flat surfaces, growth takes place by two-dimensional nucleation [102-104]. In order to create a 2-D nucleus, the solute species need to adsorb on the surface and coalesce by surface diffusion. Once the nucleus exceeds a critical size, it grows to exhibit some kink or step positions where the growth units can be preferentially incorporated as shown in Figure 2-12(b). The 2-D nucleus spreads across the surface and the crystal grows layer-by-layer.

For small crystals growing at low supersaturation, the time needed to spread across the surface is much shorter than the time needed for nucleation. Consequently, growth is controlled by nucleation. This mechanism is known as mononuclear growth. For large crystals and higher supersaturation, the time required to fill up a monolayer is much greater

(a)



(b)



(c)



Figure 2-12. Growth models: (a) continuous growth mechanism; (b) two dimensional growth mechanism; and (c) spiral growth mechanism [102, 103]. The arrows indicate the growth direction of the crystal plane.

than the time for nucleation reaction. A polynuclear mechanism then applies (i.e., the surface is at all times covered by slowly intergrowing nuclei). Between the two extremes of the mononuclear model in which the spreading velocity is infinite, and the polynuclear model in which is zero, is a model call the birth and spread model. The birth and spread model allows the spreading of nuclei at a finite constant rate that is assumed to be independent of crystal size. A growth rate expression for this model is

$$G = K_2(S - 1)^{2/3} [\ln S]^{1/6} \exp \left[ -\frac{K_3}{T^2} \ln S \right] \quad [2.16]$$

where  $K_2$  and  $K_3$  are constants [97].

Additional 2-D nuclei are necessary for further crystal growth at a new layer. Therefore, crystal growth becomes a non-continuous process in which the formation of the 2-D nucleus is the rate limiting step. Furthermore, this theory completely ignores both bulk diffusion and any surface reactions, and fails to explain crystal growth at very low supersaturation.

#### Screw dislocation theory (BCF theory)

The Burton-Cabrera-Frank (BCF) theory proposed a self-perpetrating growth model in which growth initiates at a screw dislocation acting as a source of new steps, as shown in Figure 2-12(c) [105]. Molecules adsorb on the crystal surface and diffuse to the top step of the two planes of the screw dislocation. The surface becomes a spiral staircase. After one layer is complete, the dislocation is still present, it is simply a layer higher. In this model, surface nucleation is not required for growth and growth could occur at a finite rate, even at very low supersaturation. In the two limiting cases, growth rate can be expressed as follows:

$$\begin{array}{ll} G = K_4(S^2/S_c) & \text{Low supersaturation} \\ G = K_5S & \text{High supersaturation} \end{array}$$

where  $K_4$ ,  $K_5$  and  $S_c$  are characteristic constants. These represent a parabolic dependence at low supersaturation and a linear dependence at high supersaturation [101]. In this theory, growth is controlled by surface diffusion and the distance between kinks or surface steps, which is a function of the supersaturation and crystal size.

By taking into account bulk mass transfer limitations, Chernov modified the BCF theory to explain the difference between crystal growth from solution and from the vapor phase [97]. Crystal growth from the vapor phase is not limited by mass transfer, since such transfer proceeds very rapidly. On the other hand, crystal growth from solution is inhibited by the presence of solvent, and therefore mass transfer of solute molecules to the growing crystal surface may proceed more slowly than the diffusion of adsorbed molecules across the crystal surface. Consequently, the controlling step is bulk diffusion. This model also predicts that the growth rate follows a parabolic relation with supersaturation at relatively low supersaturation. Furthermore, it indicates the importance of hydrodynamic conditions and stirring rate in the crystal formation process.

#### Surface reaction theory

Neilson [106] and Estrin [107] described the kinetics and mechanisms for ionic crystal growth from solution involving less soluble solutes. Several models have been offered to explain experimentally observed growth rates based on the assumption that the rate limiting step is the surface reactions:

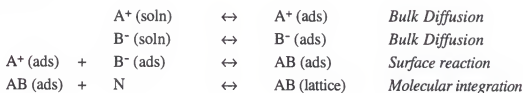
$$G = K_6(S-1)^q \quad [2.17]$$

where  $K_6$  is the constant and  $q$  is the growth rate order. It was determined that the parabolic rate law (i.e.,  $q=2$ ) prevails for sparingly soluble salts such as  $\text{BaSO}_4$ ,  $\text{CaCO}_3$ , and  $\text{CaC}_2\text{O}_4 \cdot \text{H}_2\text{O}$ .

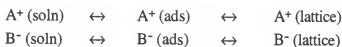
Recently, crystal growth has modeled with a chemical point of view by Chiang and Donohue [104, 108]. For an ionic crystal, lattice sites at the surface are recognized as reactant species so that growth proceeds by chemical reaction with the adsorbed ions rather than molecules. Therefore, by taking into account the linear adsorption isotherm obtained from the consideration of the electrical double layer between the growing crystal and incorporating ionic species, this model explains the observed second order dependence of growth rate on supersaturation. The most plausible growth mechanisms for ionic crystals are the surface reaction/molecular integration model (Mechanism I) and sequential ionic

integration (Mechanism II). These models represent the growth of ionic crystal AB as follows:

#### Mechanism I



#### Mechanism II



where  $A^+ \text{ (soln)}$  and  $A^+ \text{ (ads)}$  symbolize the positive ion in solution and the ion adsorbed on the surface, respectively, and  $N$  number of lattice growth sites.

#### Morphological theory

A knowledge of particle morphology is of essence to many applications as well as to the fundamental studies of the properties and reactions of solids [109]. As a nucleus develops and transforms into a crystal, it exhibits a crystallographic habit, while amorphous particles are generally spherical due to their isotropic growth. Crystal habit is a function of both the internal crystal structure and the external conditions of growth such as pH, temperature, reactant concentration, the nature of anions and additives, and agitation. Therefore, it is difficult to predict the crystal morphology.

The relation of crystal habit with internal structure was of main interest in the early investigations of crystal growth. Gibbs suggested that a polyhedral crystal in equilibrium with the surroundings would assume a shape with the minimum surface free energy. This idea was formulated by Wulff (1901) as follows [110]:

$$\frac{\gamma_1}{r_1} = \frac{\gamma_2}{r_2} = \dots = \frac{kT}{2V_m} \ln \frac{p}{p_0} \quad [2.18]$$

where  $\gamma_i$  is the specific surface energy of the  $i$  face of the polyhedral crystal,  $r_i$  is the distance of the face,  $k$  is the Boltzmann constant,  $p$  is the vapor pressure of the polyhedral

crystal, and  $p_0$  is the vapor pressure of a crystal of infinite dimensions. If the vapor pressures are replaced by the solubilities or equilibrium activities for a crystal in the solution, the equilibrium crystal form with its minimum surface energy may be expected [111]. Donnay and Harker (1937) developed a theory in which the linear growth velocity is inversely proportional to the interplanar spacing [112]. Hartman and Perdok (1955) first incorporated surface energy at the growing interface by introducing the concept of periodic bond chains (PBC) which are defined as an uninterrupted chains of strong bonds running through the crystal lattice [113, 114]. They divided the crystal faces into three types as shown in Figure 2-13. Flat faces contain at least 2 PBC, stepped faces 1 PBC and kinked faces 0 PBC. Growth was predicted to be fastest in the direction of the strongest chains. Thus, the flat faces (F-face) are the slowest growing planes which appear in crystals grown at low supersaturation, whereas the kinked faces are the fastest growing planes which do not exhibit in equilibrium crystal habit. More recently, Hartman and Bennema (1980) investigated attachment energy for a particular crystal plane as a habit-controlling factor [115, 116]. The attachment energy is defined as the energy per molecule released when one layer of thickness  $d_{hkl}$  crystallizes onto a crystal face (hkl). It was determined that the relative growth velocity always increases with increasing attachment energy. However, this relationship depends on the mechanism of crystal growth and processing variables such as supersaturation and the type of adsorbates.

A major weakness in the morphological prediction described above is that such models can only be used to represent vapor-grown crystals. However, unlike the vapor, the solvent is not inert and unreactive toward the crystal [117]. Solvent-solid interactions modify surface energetics and hence modify the shape of the crystal produced from a specific solvent. The shape of a crystal is determined by the difference in relative growth rates of the individual crystal planes, and the resulting particles are normally bound by facets with the lowest growth rate constant (growth form) under a certain supersaturation. It is frequently observed that specific adsorption of ions, complexes, and organic

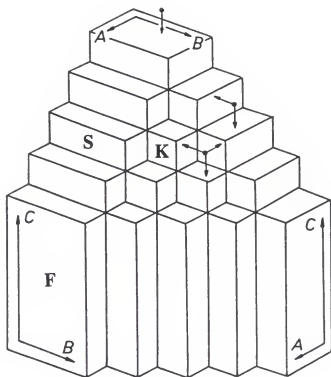


Figure 2-13. Hypothetical crystal structure showing flat (F), stepped (S), and kinked (K) faces [113]. The A, B, and C represent three different directions of the periodic bond chain.

compounds gives rise to significant modification in crystal shape by restraining, or sometimes promoting, the growth of the facets to which they are adsorbed [118, 119].

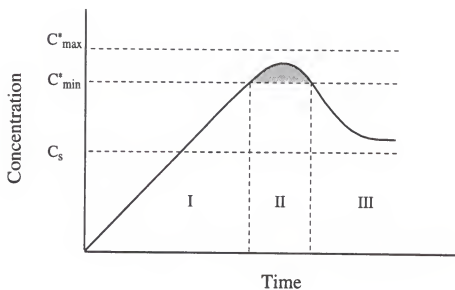
### Physical Growth Mechanism for Monodisperse Particle Formation

The preparation of uniform particles with a narrow size distribution is very important in ceramic processing as described in section 2.3. In addition, well-defined colloidal dispersions are essential for the evaluation of properties of particle matter such as the optical, magnetic properties as well as for theoretical understanding of powder properties such as the interactions that occur between particles [120, 121]. Stober et al. developed a synthesis procedure which leads the production of monodisperse colloidal silica by the hydrolysis of a silicon alkoxide in a mixed solvent of alcohol and water [122]. Matijevic et al. also demonstrated the possibility to generate a variety of materials with controlled size and particle shape by precipitation from homogeneous solution [60, 109].

To explain the monodispersity, the introduction of different physical models which can provide mechanisms about how to combine and control precipitation processes are required, in addition to the separate theoretical descriptions of nucleation and growth processes. As a simple picture, it can be assumed that complex precipitation processes can be divided into the elementary steps of nucleation and growth, free from secondary nucleation and aggregation [123, 124]. LaMer and Dinegar first explained qualitatively the mechanism of formation of monodisperse sulfur sols by the decomposition of sodium thiosulfate in acidic solution which is illustrated in Figure 2-14 [125].

The concentration of solutes is built-up in stage I, for instance, by slow decomposition of inert compounds, or the formation of some sparingly soluble complexes. During this state, no precipitation takes place. When the concentration  $C$  reaches  $C^*_{\min}$ , the nucleation stage (stage II) sets in. In this stage,  $C$  still keeps climbing for a while and then decreases as result of the consumption of solutes by nucleation. When  $C$  reaches  $C^*_{\min}$  again, nucleation ends. Finally, the growth stage (stage III) ensues until the

(a)



(b)

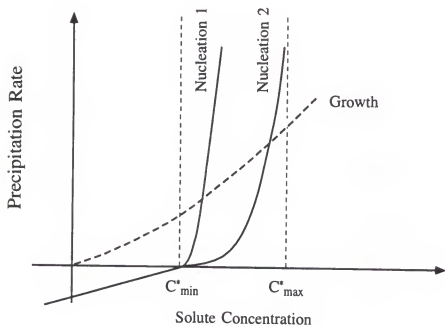


Figure 2-14. The LaMer-Dineger model for monodisperse particle formation: (a) solute concentration as a function of precipitation time; and (b) precipitation rate for nucleation and growth as a function of solute concentration where I pre-nucleation stage, II nucleation stage, and III growth stage [111].

concentration is lowered close to the solubility level  $C_s$ . The rate of both the nucleation and the growth should be also considered [111]. If the nucleation rate soars as sharply as nucleation curve 1 when the solute concentration exceeds  $C_{min}^*$ , the separation between nucleation and growth is ideally achieved. If the nucleation rate is not sufficiently high, similar to nucleation curve 2, on the other hand, particle growth will occur at the same time.

Although this mechanism is simple and reasonably assumed, it applies only to the initial stage of the precipitation process. There are two further developed models for monodisperse particle formation based on the LaMer-Dinegar model: the monomer addition model and aggregative growth model.

#### Monomer addition model

This model was originally developed for monodisperse silica particles prepared by the Stober process [126, 127]. Reaction between two reactive monomers over an initial period occurs to form a colloiddally stable nuclei and then after a finite time the monomer reacts growing nuclei rather than others. This leads to the uniformity in size distribution. Nucleation is complete when the rate of monomer addition to particles exceeds the rate at which the two monomers react (i.e., the concentration of soluble species has dropped below the critical nucleation concentration). The reaction preference of the monomer, toward either other monomer for nucleation or the surface of the existing nuclei for growth is determined by a balance of the competing nucleation and condensation rates of the silicon alkoxide. Once all nuclei have formed, growth continues by the addition of monomer with no further nucleation. At this stage of the process, the monomer addition rate onto the nuclei in a given system determines the mass of the final size and size distribution. The production of monomers is a rate limiting step.

#### Aggregative growth model

The aggregative growth model is characterized by the incorporation of colloidal stability in the growth mechanism and is similar to the growth mechanism of polymer particles predicted by Flory-Stockmayer [128, 129]. Compared to the stable nuclei

formation assumption in the LaMer-Dinegar model and monomer addition model, this model suggests the generation of unstable primary particle formation which leads to aggregation. Particle growth proceeds by the aggregation of unstable primary particles that are slowly produced during the entire reaction period. This aggregation process is controlled in the sense that once the aggregates have reached a certain size, a certain colloidal stability is acquired because of surface charge, and the growth continues only by aggregations of clusters and not by collisions with other larger particles. The production of primary particles is a rate limiting step. In this model, nucleation may proceed independently of the presence of particles later in the reaction. To achieve monodispersity, the rate at which the nuclei attach to the growing particles is sufficiently high to prevent any of the smaller primary particles from growing to a colloiddally stable size.

### Summary

Ferroelectrics are a special group of advanced electronic materials which are spontaneously polarized and possess the ability to switch their internal polarizations under an applied field. The onset of ferroelectric states is closely related to the nature of crystal structure in which each permanent dipole arranges with the direction of an electric field in a cooperative manner at the temperature where the randomizing effect of thermal energy is overcome. As a result, ferroelectric materials possess very large dielectric constants ( $k > 1000$ ), large piezoelectric coefficients and large pyroelectric coefficients. Used in various forms ranging from single crystal to thin films, the applications of ferroelectric materials include multilayer capacitor, transducers, pyroelectric sensors, and electro-optic devices.

Recently, the growing demand for ferroelectric ceramics with better functionality and performance accelerates the development of powder synthesis techniques. The goal in the preparation of ferroelectric powders is to achieve ceramic powders which, after consolidation, yield a product satisfying specified performance standards. A secondary goal is to produce a powder that can be densified at lower temperatures. Both physical and

chemical properties of the powders must be well defined and characterized where control of homogeneity, purity, particle size and stoichiometry are important. To accomplish this purpose, a wide variety of chemical solution techniques as an alternative to conventional solid state reaction methods has been developed. One of the principal advantages of chemical synthesis is the high degree of chemical homogeneity attained with a very complex composition. This homogeneity can be on the atomic scale in the solution phase, and the goal of the subsequent ceramic processing is to retain as much of that homogeneity as possible in the ceramic powder and ultimately in the fabricated and sintered ceramic body.

In particular, hydrothermal processing offers a potentially superior technique for low-cost and low-temperature production of ferroelectric ceramic powders as compared to other solution synthesis methods. Because crystalline powders are directly produced by the hydrothermal treatment, the need for high temperature calcination and milling procedures to remove aggregates is eliminated. By controlling reaction conditions, in addition, it is possible to produce crystalline powders with controlled particle size, controlled stoichiometry, and in some cases controlled particle shape. To understand and control such capabilities, the overall precipitation processes must be well understood.

Precipitation process proceeds by either successive or simultaneous reactions such as nucleation, growth, Ostwald ripening, aggregation, and aging. The characteristics and properties of precipitates is mainly determined by the rates and mechanisms by which each above process undergoes, depending on the experimental conditions. In order to produce well-defined particles with uniform size distribution, the overall precipitation processes must be controlled. Formation of monodisperse particles is usually achieved by precipitation from homogeneous solution. The separation between the nucleation and growth reaction is necessary to allow only a limited number of nuclei to grow by addition of a molecular solute in solution phase, ensuring monodispersity.

## CHAPTER 3

### THERMODYNAMIC APPROACH TO HYDROTHERMAL SYNTHESIS OF BaTiO<sub>3</sub>

#### Introduction

Hydrothermal particle synthesis is a complex process requiring a fundamental understanding of the interactions between solid state chemistry, interfacial reactions and kinetics, and solution chemistry. The solution phase is a solvation medium through which the dissolved species can diffuse into the solid phase, and at the same time a chemical agent by which the solution species undergo chemical reactions such as hydrolysis, condensation, and complexation. Furthermore, the solution phase acts as a phase boundary with the precipitating solid so that a surface charge on the solid can develop and complex species can adsorb, thus modifying the interfacial behavior. The interaction between the solid and solution phases determines the physical characteristics of the resulting powder. These many aspects result in complicated nature of hydrothermal reactions. The solvent-solid interaction depends on chemical process variables such as temperature, pressure, reactant concentration, and pH. Therefore, thermodynamic knowledge is required to understand and control hydrothermal particle formation mechanisms. In the current Chapter, the fundamental role that solution chemistry based on thermodynamics plays in the hydrothermal synthesis will be discussed.

#### Stability Diagram for the Ba-Ti-H<sub>2</sub>O System

Hydrothermal synthesis is a promising method for preparing multicomponent electronic ceramics. Phase-pure agglomerate-free well-crystalline ceramic powders can be hydrothermally synthesized in a single experimental step, as described in Chapter 2. To take full advantage of such capabilities, the synthesis procedures must be well defined.

The design of appropriate synthesis conditions is currently a matter of trial. The process variables such as reagent concentration, pH, temperature, and pressure must be optimized to produce cost-effectively the desired ceramic powders. However, this optimization is a time-consuming process due to the large number of variables involved [130, 131].

Thermodynamic prediction of the conditions under which hydrothermal reactions for the desired product solids will proceed can be obtained by calculating the Gibb's free energy for the balanced reaction in water as a function of pH and temperature. Calculations for the aqueous system are much more complex than calculations for solid-state reactions because solution species may undergo complexation during chemical reactions. Thus, many different soluble species may be present and in turn many different reactions are permissible. A useful representation regarding this information is the log [Me]-pH diagram which is called the stability diagram, where [Me] is the concentration in the aqueous solution of the metal cations of interest. Such a stability diagram delineates the stability domains of relevant aqueous species and solid compounds at given temperature and pressure.

The simplest stability diagram can be constructed by assuming that the aqueous solution behaves as an ideal solution [132]. In these calculations, the solution is considered sufficiently dilute so that all activities are equal to the respective specie concentrations. The formation free energy ( $\Delta G_f$ ) for all the possible reactions which may occur in a given material system needs to be calculated using the Gibbs free energy of formation of each species at the temperature and pressure of interest. For the purpose of demonstration, the BaTiO<sub>3</sub> stability diagram at 25°C is considered. All possible reactions for the hydrothermal synthesis of BaTiO<sub>3</sub> are summarized in Table 3-1 and 3-2. The standard free energies for both the solid and aqueous phases which are used to calculate the reaction constants are also summarized Table 3-3 [131, 133]. In the reaction of  $\text{Ba}^{2+}_{(\text{aq})} + \text{H}_2\text{O} = \text{BaO}_{(\text{s})}$ , for instance,  $\Delta G_{rxn}^{\circ}$  can relate to the reaction constant (K) as follows:

$$\Delta G_{rxn}^{\circ} = -RT \ln K \quad [3.1]$$

Table 3-1. Reaction Constants for the Ti-H<sub>2</sub>O System at 25°C

Compound	pH	Ti	H <sub>2</sub> O	$\Delta G_p^\circ$ (kJ/mole)	Log K
Ti(OH) <sub>3</sub> <sup>+</sup>	+	Ti <sup>4+</sup>	3H <sub>2</sub> O	-963.43	168.78
Ti(OH) <sub>4</sub> <sup>o</sup>	+	Ti <sup>4+</sup>	4H <sub>2</sub> O	15.2	-2.66
TiOH <sup>3+</sup>	+	Ti <sup>4+</sup>	H <sub>2</sub> O	22.57	-3.95
HTiO <sub>3</sub> <sup>-</sup>	+	Ti <sup>4+</sup>	1H <sub>2</sub> O	-110.05	19.28
TiO <sub>2</sub> (rutile)	+	Ti <sup>4+</sup>	2H <sub>2</sub> O	62.02	-10.87
TiO <sub>2</sub> (anatase)	+	Ti <sup>4+</sup>	2H <sub>2</sub> O	54.59	-9.56

Table 3-2. Reaction Constants for the Ba-Ti-H<sub>2</sub>O System at 25 °C

Compound	pH	Ba	H <sub>2</sub> O	Rutile	$\Delta G_f^\circ$ (kJ/mole)	Log K
BaOH <sup>+</sup>	+	=	H <sub>2</sub> O		-81.31	-14.24
BaO	+	=	H <sub>2</sub> O		-272.68	47.77
Ba(OH) <sub>2</sub>	+	=	2H <sub>2</sub> O		-180.11	31.55
Ba(OH) <sub>2</sub> ·8H <sub>2</sub> O	+	=	10H <sub>2</sub> O		-153.38	26.87
BaTiO <sub>3</sub>	+	=	H <sub>2</sub> O	+ TiO <sub>2</sub>	-116.33	20.38
Ba <sub>2</sub> TiO <sub>4</sub>	+	=	2H <sub>2</sub> O	+ TiO <sub>2</sub>	-353.86	61.99

Table 3-3. Standard Free Energy Formation in the Ba-Ti-H<sub>2</sub>O System

Solid Species	$\Delta G_f^\circ$ (kJ/mole)
TiO <sub>2</sub> (rutile)	-890.70
TiO <sub>2</sub> (anatase)	-883.27
BaO	-525.35
Ba(OH) <sub>2</sub>	-855.17
Ba(OH) <sub>2</sub> ·8H <sub>2</sub> O	-2779.90
BaTiO <sub>3</sub>	-1572.40
Ba <sub>2</sub> TiO <sub>4</sub>	-2132.90
Aqueous Species	$\Delta G_f^\circ$ (kJ/mole)
H <sub>2</sub> O	-237.25
H <sup>+</sup>	0.0
OH <sup>-</sup>	-157.30
Ti <sup>4+</sup>	-354.18
HTiO <sub>3</sub> <sup>-</sup>	-955.88
Ti(OH) <sub>3</sub> <sup>+</sup>	-102.50
Ti(OH) <sub>2</sub> <sup>2+</sup>	-869.56
TiOH <sup>3+</sup>	-614.00
Ti(OH) <sub>4</sub> <sup>0</sup>	-1318.38
Ba <sup>2+</sup>	-560.78
BaOH <sup>+</sup>	-716.72

After converting to logarithmic notation, the equation reduces to

$$\text{Log}[Ba^{2+}] - \text{Log}[H^+] = \text{Log}K = -\frac{2.303}{RT} \Delta G_{rxn}^{\circ} \quad [3.2]$$

By plotting  $-\text{Log}[H^+]$  on the x-axis while  $\text{Log}[Ba^{2+}]$  on the y-axis, a phase boundary line in which  $BaO_{(s)}$  is in equilibrium with the aqueous barium species can be determined. Similar calculations are necessary for all the possible reactions in solution in order to generate the stability diagram. Figure 3-1 shows the stability diagram for the Ti-H<sub>2</sub>O system at 25°C under ideal solution conditions. TiO<sub>2</sub> is very stable over most of the pH range in which the dominant solution species is  $Ti(OH)_4(aq)$ . At pH below 2, TiO<sub>2</sub> becomes soluble and  $Ti(OH)_2^{2+}$  is the dominant species in solution. It is determined that the solubility of anatase is 10<sup>-7</sup> mole/liter while 10<sup>-8</sup> for rutile. Since titania is very stable in water, its solution species can be ignored in the calculations for the stability diagram of the Ba-Ti-H<sub>2</sub>O system at 25°C. As shown in Figure 3-2, it is predicted that BaTiO<sub>3</sub> is stable only at a highly alkaline condition in which the dominant solution species is BaOH<sup>+</sup>. However, the Ba<sup>2+</sup> is preferentially leached out of BaTiO<sub>3</sub> leaving behind a TiO<sub>2</sub> rich surface layer when the pH decreases below 11.

For the ideal solution assumption to be valid, the solution is required to have an ionic strength of zero, which is not possible in the real system. This approximation becomes especially inaccurate when concentrated electrolyte solutions are utilized or when a multitude of competing reactions occur in a solution, thus making the equilibrium concentration of various species strongly dependent on activity coefficients. Recently, Lenka and Riman developed a comprehensive thermodynamic model that simulates hydrothermal reactions for various perovskite materials including BaTiO<sub>3</sub>, PbTiO<sub>3</sub>, SrTiO<sub>3</sub>, and CaTiO<sub>3</sub> [131, 134-136]. This thermodynamic model offers a more rigorous approach due to the incorporation of realistic estimate of the activity coefficients for all possible solid and solution species. It was determined that the solution pH and metal concentrations are important thermodynamic variables for the synthesis of phase-pure perovskite materials. They demonstrated that BaTiO<sub>3</sub> is thermodynamically stable only

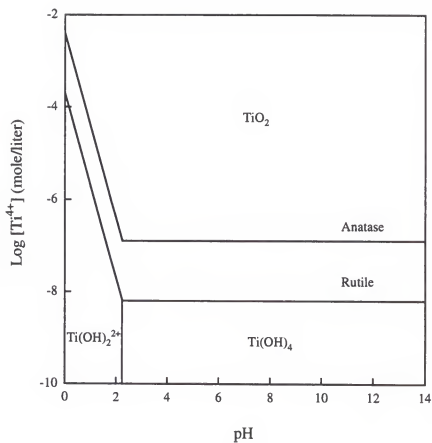


Figure 3-1. Theoretical phase stability diagram for the Ti-H<sub>2</sub>O at 25°C based on the ideal solution approximation.

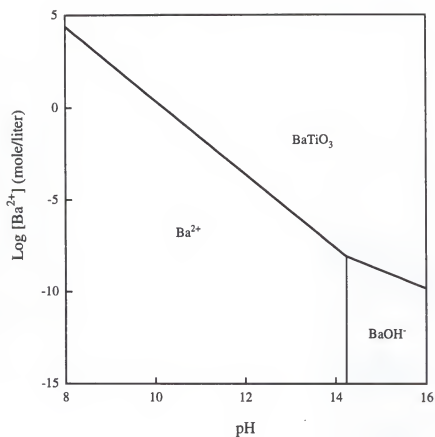


Figure 3-2. Theoretical phase stability diagram for the Ba-Ti-H<sub>2</sub>O at 25°C based on the ideal solution approximation.

in highly alkaline conditions ( $\text{pH} > 11$ ) and at barium concentrations greater than  $10^{-5}$  mole/liter as shown in Figure 3-3(a). Using this comprehensive modeling, the influence of synthesis environment can also be easily taken into account for predicting the behavior of the desired product under hydrothermal conditions. For example, the stability of  $\text{BaTiO}_3$  significantly decreases in the presence of  $\text{CO}_2$  by forming a contaminant  $\text{BaCO}_3$ . It was predicted that  $\text{BaCO}_3$  predominantly forms instead of  $\text{BaTiO}_3$  precipitation, as shown in Figure 3-3(b). This tendency suggests that synthesis of  $\text{BaTiO}_3$  must be performed in a  $\text{CO}_2$ -free atmosphere using  $\text{CO}_2$ -free aqueous solutions.

In comparison with the results from a rigorous thermodynamic computation, the magnitude of the phase stability boundaries obtained based on the ideal solution assumption is relatively inaccurate, as indicated in Figure 3-3(a). However, the general trend in the phase stability of a given material system can be revealed by the simple calculations. It should be noted here that comprehensive thermodynamic computations may also be misleading due to the lack of thermodynamic data and/or inaccurate data. In addition, neither formation of metastable crystalline nor amorphous products due to sluggish reaction kinetics can be inferred from thermodynamic computations [137].

### Aqueous Solution Chemistry

Hydrolysis and condensation reactions of metal cations are difficult to control in aqueous solution since water behaves both as a solvent and a hydrolysis agent. Several monomeric or oligomeric metal species can form simultaneously in aqueous solution. These solution species are in rapid equilibrium, and it is not easy to predict which species will undergo condensation and eventually nucleate the solid phase. Little information on such aqueous solution complexes is available in the literature, especially at elevated temperatures which are of importance in most preparation procedures. In this regard, the theoretical background for aqueous chemical reactions will be provided in this section based on the Partial Charge Model (PCM) by Livage et al. in order to understand

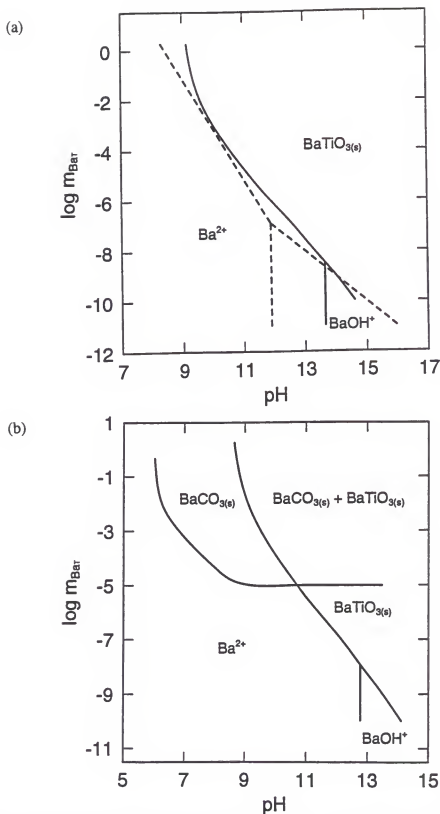
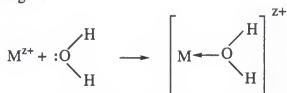


Figure 3-3. Phase stability diagram for the Ba-Ti-H<sub>2</sub>O system at 65°C including activity coefficients: (a) CO<sub>2</sub> free condition; and (b) in the presence of CO<sub>2</sub>. The dashed line indicates the results from the ideal solution approximation [131].

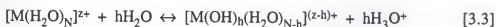
the behavior of metal-inorganic complexes in aqueous solution [137, 138].

### Hydrolysis

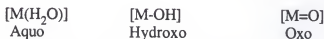
When dissolved in aqueous solutions, metal cations  $M^{z+}$  are solvated by dipolar water molecules according to:



Water behaves as a Lewis base so that charge transfer occurs from the filled symmetric bonding orbital of the water molecule to the empty orbital of the metal cation. The exact nature of the coordination of water molecules (i.e., hydration number  $N$ ) around the cations is not fully resolved. It is generally accepted, however, that there is more than one coordination sphere and six water molecules arrange octahedrally in the first coordination sphere of most metal cations as illustrated in Figure 3-4 [139]. Solvation increases the partial charge of the hydrogen, making the water more acidic, i.e., weakening  $O^{\delta-} \cdots H^{\delta+}$  bonds of the water molecule. Spontaneous deprotonation, which is defined as hydrolysis, then takes place as follows [55]:



Depending on the degree of hydrolysis, the above equation defines the three types of ligands:



The precise nature of these aqueous complexes depends on the charge ( $z$ ), hydration number ( $N$ ), and electronegativity ( $\chi_M^0$ ) of the metal, and the temperature and pH of the aqueous solution. Livage and coworkers have developed the partial-charge model (PCM) in order to predict the nature of the aqueous complexes (i.e., the degree of hydrolysis). The PCM is based on the electronegativity equalization principle in which proton exchange between the precursor and the solution proceeds until the mean

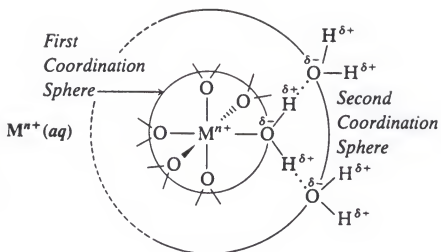


Figure 3-4. Schematic picture illustrating the solvated metal cation [139].

electronegativity of the hydrolyzed precursor ( $\bar{\chi}_p$ ) becomes equal to the mean electronegativity of the aqueous solution ( $\bar{\chi}_w$ ). By assuming a linear relationship between  $\bar{\chi}_w$  and the solution pH (i.e.,  $\bar{\chi}_w = 2.732 - 0.035 \text{ pH}$ ), the partial charge ( $\delta_i$ ) of each atom  $X_i$  in a given precursor can be calculated. For precursor  $(p_1X_2 \cdot p_2X_2 \dots p_iX_i)$ , the  $\bar{\chi}_p$  and  $\delta_i$  are given as follows:

$$\bar{\chi}_p = \frac{(\sum_i p_i \sqrt{\chi_i^0}) + 1.36z}{(\sum_i p_i / \sqrt{\chi_i^0})} \quad [3.4]$$

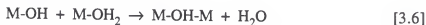
$$\delta_i = \frac{(\bar{\chi} - \chi_i^0)}{1.36\sqrt{\chi_i^0}} \quad [3.5]$$

where  $p_i$  is the number of atom  $X_i$  and  $\chi_i^0$  is the Pauling electronegativity for atom  $X_i$  expressed in the frame of Allred-Rochow's model [139].

As a consequence, the degree of hydrolysis ( $h$ ) for the aqueous metal species can be predicted as a function of pH, as shown Figure 3-5. This diagram explains why the hydrolysis of low-valence cations ( $z < 4$ ) yield aquo, hydroxo, or aquo-hydroxo complexes over the complete pH range, whereas high-valence cations ( $z > 4$ ) form oxo or oxo-hydroxo complexes.

### Condensation

Condensation between hydrolyzed mononuclear species in aqueous solutions only becomes possible when at least one M-OH bond is present in the precursor, that is, in the intermediate domain of Figure 3-5 [138]. Condensation is usually initiated via pH variations by adding a base to low valence aquo cations or an acid to high-valence oxo anions. Condensation proceeds via either olation or oxolation mechanisms. First of all, olation is a nucleophilic attack of a negatively charged OH group onto a positively charged metal cation. This leads to the departure of one coordinated water molecule and the formation of a hydroxyl bridge as (-OH-) as follows:



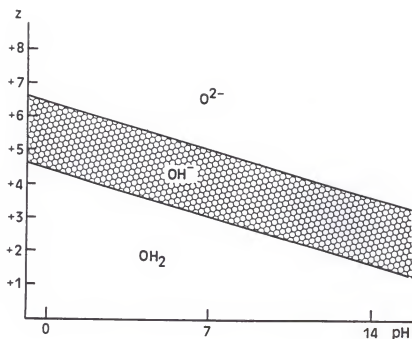


Figure 3-5. The charge-pH diagram indicating the type of solution species formed in aqueous solution as a function of the valence state of metal cation [137].

Secondly, in the case of oxolation, two hydroxo groups react together forming a water molecule and an oxo bridge (-O-) as follows:



The oxolation reaction involves a proton transfer between two OH groups within the transition state ( $\text{M-OH}\cdots\text{HO-M}$ ) in order to form the departing water molecule. It is therefore kinetically slower than ololation.

On the other hand, the M-OH bonds themselves may undergo chemical reaction in an aqueous solution depending upon the electronegativity and charge of the metal cations. When the metal is more electronegative than hydrogen, acid dissociation occurs:



Reversely, base dissociation occurs when  $\chi_{\text{M}}^0 < \chi_{\text{H}}^0$ :



Condensation can occur through ololation and/or oxolation only when the M-OH bond remains stable against both either acid or base dissociation. Therefore, the critical electronegativities corresponding to all possible reactions in aqueous solution including condensation, acid, or base dissociation can be calculated in the frame of the PCM. This approach results in a charge-electronegativity diagram in which five groups of cations are distinguished as shown in Figure 3-6: Region I: the elements undergo basic ionization, resulting in inorganic bases which do not condense in aqueous solutions; Region II: the elements condense only via ololation leading to hydroxide  $\text{M}(\text{OH})_2$  precipitation; Region III: the elements condense both through ololation and oxolation leading to hydrous oxide  $\text{MO}_{2/2} \cdot x\text{H}_2\text{O}$  precipitation; Region IV: the elements condense only through oxolation, resulting in molecular poly-acid formation; Region V: the elements undergo acid dissociation, giving rise to inorganic acids which are not able to condense in aqueous solutions [137].

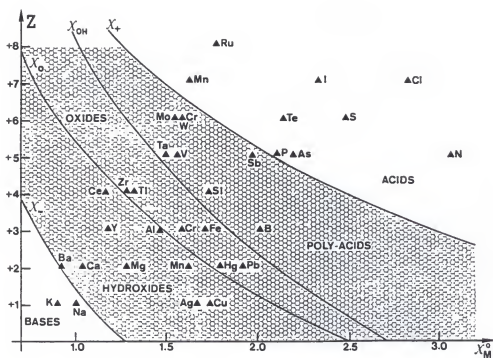
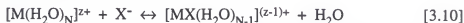


Figure 3-6. The charge-electronegativity diagram illustrating the five different regimes of condensed species for the various metal cations [137].

### Complexation by Anion Species

Chemical species other than water, proton or hydroxyls, can play an important role in the formation of condensed phases from aqueous solutions. For instance, the size, shape, and phase of particles produced from solution phase can be controlled by various types of anions [140]. Negatively charged anionic species react with positively charged metal cations  $M^{z+}$  to give new metal complexes as follows:



where  $X^-$  corresponds to monovalence monodentate anionic species such as  $Cl^-$  and  $CH_3COO^-$ . This complexation can be described as the nucleophilic substitution of a water molecule by the anion. The complexing ability of anion  $X^-$  towards metal cation  $M^{z+}$  depends upon the electronegativities of the M-X complexes ( $\chi_{MX}$ ), the anion  $X^-$  ( $\chi_{X^-}$ ), and its protonated form HX ( $\chi_{HX}$ ) [138]. The complexation is usually effective only over a certain range of pH:

$$pH [\chi_{HX}] < pH < pH [\chi_{X^-}] \quad [3.11]$$

where  $pH [\chi_i]$  indicates the pH value corresponding to the electronegativity of the solution species  $i$ . Below  $pH [\chi_{HX}]$ , the HX molecule cannot interact with the cation, which is too electronegative to be polarized by the anion. Above  $pH [\chi_{X^-}]$ , the  $X^-$  anion behaves as a counter ion and the cation is not electronegative enough to polarize the electronic cloud of the anion.

### Modeling of the Ba-Ti-H<sub>2</sub>O System

Following the PCM, it can be assumed that electron transfer between the precursor  $[M(OH)_h(H_2O)_{N-h}]^{(z-h)+}$  of mean electronegativity  $\bar{\chi}_p$  and the aqueous solution of mean electronegativity  $\chi_w$  goes on until both values become equal:

$$\bar{\chi}_p = \bar{\chi}_w = 2.732 - 0.035 \text{ pH} \quad [3.12]$$

The hydrolysis ratio of aquo species can then be calculated at any pH using the equations

[3.1] and [3.2] since the total charge  $+(z-h)$  of the precursor must be equal to the sum of all partial charges as follows:

$$h = (z - N\delta_o - 2N\delta_H - \delta_M) / (1 - \delta_H) \quad [3.13]$$

The hydrolysis ratio diagrams for both Ba(II) and Ti(IV) as a function of pH were generated as shown in Figure 3-7. The hydration number  $N$  for the Ba and Ti was assumed to be 4 and 6, respectively. All the aqueous solution species of both Ba and Ti depending upon the hydrolysis ratio are summarized in Table 3-4.

Table 3-4. Possible Hydrolyzed Species of Barium and Titanium in Aqueous Solution

Hydrolysis Ratio (h)	Hydrolyzed Species	
	Ba	Ti
1	$[\text{Ba}(\text{OH})(\text{H}_2\text{O})_5]^+$	
2	$[\text{Ba}(\text{OH})_2(\text{H}_2\text{O})_4]^0$	$[\text{Ti}(\text{OH})_2(\text{H}_2\text{O})_4]^{2+}$
3		$[\text{Ti}(\text{OH})_3(\text{H}_2\text{O})_3]^+$
4		$[\text{Ti}(\text{OH})_4(\text{H}_2\text{O})_2]^0$
5		$[\text{Ti}(\text{OH})_5(\text{H}_2\text{O})]^-$
6		$[\text{Ti}(\text{OH})_6]^{2-}$

For the Ba(II) ions, the solvated  $[\text{Ba}(\text{H}_2\text{O})_4]^{2+}$  without hydrolysis is stable below  $\text{pH} < 6$  while  $[\text{Ba}(\text{OH})(\text{H}_2\text{O})_5]^+$  becomes dominant in the pH range from 6 to 13. The neutral  $[\text{Ba}(\text{OH})_2(\text{H}_2\text{O})_4]^0$  species is stable only at strong alkaline conditions (i.e.,  $\text{pH} > 14$ ). It is predicted that the solvated  $\text{Ba}^{2+}$  cannot be deprotonated and remains as a monomeric species without undergoing condensation in aqueous solution. Instead,  $[\text{Ba}(\text{OH})(\text{H}_2\text{O})_5]^+$  will condense only through ololation, leading to  $\text{Ba}(\text{OH})_2$  precipitation in alkaline medium. For the Ti (IV) ions, the possible hydrolysis ratio (h) ranges from 2.7 to 6.3. As a result,  $[\text{Ti}(\text{OH})_2(\text{H}_2\text{O})_4]^{2+}$  and  $[\text{Ti}(\text{OH})_6]^{2-}$  are stable only at strong acidic ( $\text{pH} <$

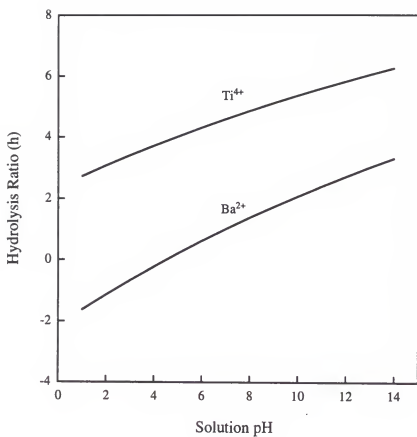
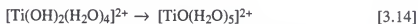
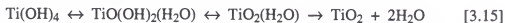


Figure 3-7. The calculated hydrolysis ratio of both barium and titanium metal cations as a function of pH.

1) and basic (pH >14) conditions, respectively. As the pH increases from 2 to 13, the stable aqueous species of Ti change from  $[\text{Ti}(\text{OH})_3(\text{H}_2\text{O})_3]^+$  through  $[\text{Ti}(\text{OH})_4(\text{H}_2\text{O})_2]^0$  to  $[\text{Ti}(\text{OH})_5(\text{H}_2\text{O})]^-$ . The  $[\text{Ti}(\text{OH})_2(\text{H}_2\text{O})_4]^{2+}$  undergoes a spontaneous intramolecular oxolation at strong acidic conditions (pH < 1) leading to the formation of titanyl ions  $[\text{TiO}]^{2+}$  as follows [138, 141]:



At  $5 < \text{pH} < 9$ ,  $[\text{Ti}(\text{OH})_4(\text{H}_2\text{O})_2]^0$  is expected to be responsible for the precipitation of hydrous titania. Instead of forming  $\text{Ti}(\text{OH})_4$ -based hydroxides, the  $[\text{Ti}(\text{OH})_4(\text{H}_2\text{O})_2]^0$  precursors rearrange structure to form water molecules which are easily withdrawn due to a positive partial charge as follows [138, 142]:



Simultaneous oxolation and ololation occur subsequently during nucleation and growth forming amorphous hydrous oxides  $\text{TiO}_2 \cdot x\text{H}_2\text{O}$  where the number  $x$  of water molecules depends on experimental conditions.

The complexing abilities of various anions with respect to both Ba(II) and Ti(IV) were also predicted using the PCM. In order to calculate the pH ranges for complexation, the same electronegativity equalization principle was applied, which provides a quantitative guide to determine whether complexation occurs as a function of pH as follows:

$$2.732 - 0.035 \text{pH} = \frac{\chi_q(\Delta + 5.732\alpha + 2.064q) - 4.071(3.507\alpha + 2.064q)}{\Delta + (1.408\alpha + 0.507q)\chi_q - (3.507\alpha + 2.064q)} \quad [3.15]$$

$$\text{where } \Delta = z - 2.225N - (4.071 - \chi_M^0)/(1.36\sqrt{\chi_M^0}) \quad [3.16]$$

The  $\alpha$  corresponds to the number of water molecules which are replaced by one anionic ligand. For example,  $\alpha=1$  for monodentate ligands like  $\text{Cl}^-_{(\text{aq})}$  and  $\alpha=2$  for bidentate ligands such as  $\text{SO}_4^{2-}_{(\text{aq})}$ . Both cases are called inner sphere complexation, whereas complexation occurs in the outer coordination sphere when  $\alpha=0$ . The  $q$  is the number of protonation in the anionic species  $\text{X}^{n-}$  where  $0 \leq q \leq n$ .

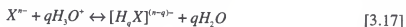


Table 3-5. Electronegativities for Selected Species [139]

Atoms	Pauling Electronegativity
H	2.2
C	2.5
O	3.5
N	3.07
S	2.44
Ba	0.97
Ti	1.32
Cl	2.83
Aqueous Species	Calculated Electronegativity
$\text{CH}_3\text{COO}^-$	2.29
$\text{Cl}^-$	2.46
$\text{SO}_4^{2-}$	2.28
$\text{HSO}_4^-$	2.66
$\text{NO}_3^-$	2.76
$\text{CH}_3\text{COOH}$	2.55
HCl	2.50
$\text{HNO}_3$	3.11

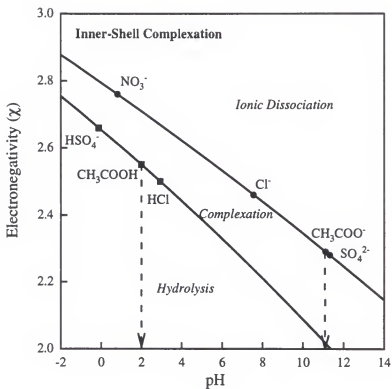
For example, the  $q$  values for HCl and  $\text{Cl}^-$  are 1 and 0, respectively. The electronegativity data used in the current calculations are summarized in Table 3-5. The electronegativity-pH diagrams for both the Ba(II) and Ti(IV) cations were generated as presented in Figure 3-8 and Figure 3-9.

The complexing pH ranges for various anionic species with the metal cations are summarized in Table 3-6. It is predicted that the [Ti-Cl] complexes are stable in the pH range 4 to 8. In the neutralization process of  $\text{TiCl}_4$  at this pH range, therefore, chloride ions are expected to be retained within the  $\text{TiO}_2 \cdot x\text{H}_2\text{O}$  precipitates, which requires an extensive washing procedure to remove. Furthermore, the type of complexing anions can influence phases of the precipitates. For instance, hydrolysis of  $\text{TiCl}_4$  in the presence of HCl leads to the formation of rutile. Below pH 3,  $\text{Cl}^-$  is not involved in the hydrolyzed aqueous species of Ti. Under these conditions, ololation between  $[\text{Ti}(\text{OH})_2(\text{H}_2\text{O})_4]^{2+}$  first gives linear chains made of edge-sharing  $[\text{TiO}_6]$  octahedra [137, 143]. Oxolation then gives corner-sharing octahedra chains which is typical of the rutile structure. On the other hand, anatase forms in the presence of  $\text{HSO}_4^-$ . Strong bidentated chelating prevents linear condensation, and ololation leads to the formation of skewed  $[\text{TiO}_6]$  chains characteristic of the anatase phase.

Table 3-6. The pH Range for Stable Metal-Anion Complexation

Complexes	Inner-Sphere Complexation	Outer-shell Complexation
[Ba- $\text{CH}_3\text{COO}^-$ ]	$2.00 < \text{pH} < 11.11$	$1.66 < \text{pH} < 12.63$
[Ba- $\text{Cl}^-$ ]	$2.93 < \text{pH} < 7.56$	$2.88 < \text{pH} < 7.77$
[Ba- $\text{SO}_4^{2-}$ ]	$-0.12 < \text{pH} < 11.32$	$-1.04 < \text{pH} < 12.91$
[Ba- $\text{NO}_3^-$ ]	$-9.84 < \text{pH} < 0.81$	$-12.40 < \text{pH} < -0.8$
[Ti- $\text{CH}_3\text{COO}^-$ ]	$2.51 < \text{pH} < 11.37$	$2.23 < \text{pH} < 12.63$
[Ti- $\text{Cl}^-$ ]	$3.52 < \text{pH} < 7.59$	$3.47 < \text{pH} < 7.77$
[Ti- $\text{SO}_4^{2-}$ ]	$0.24 < \text{pH} < 11.58$	$-0.52 < \text{pH} < 12.91$
[Ti- $\text{NO}_3^-$ ]	$-10.01 < \text{pH} < 0.52$	$-12.14 < \text{pH} < -0.80$

(a)



(b)

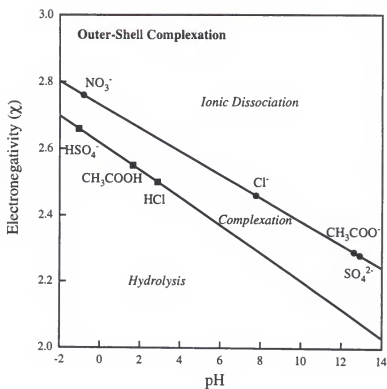


Figure 3-8. The electronegativity-solution pH diagram for [Ba-anions] complexation: (a) complexation in inner-shell coordination; and (b) complexation in outer-shell coordination.

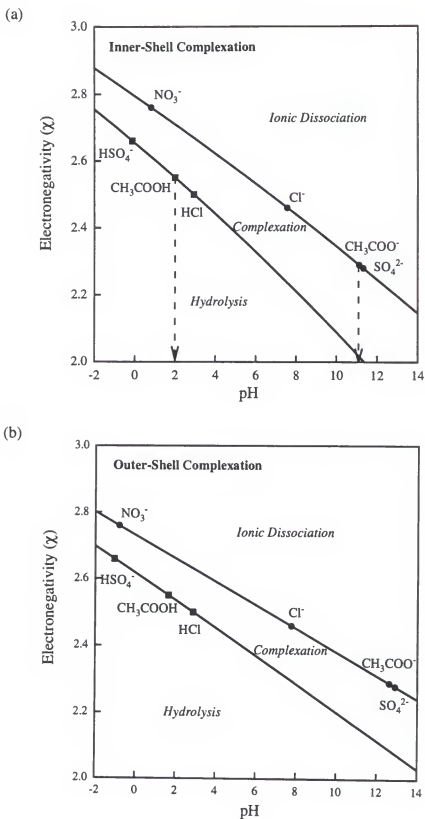


Figure 3-9. The electronegativity-solution pH diagram for [Ti-anions] complexation: (a) complexation in inner-shell coordination; and (b) complexation in outer-shell coordination.

Complexation of barium by acetate anions is expected to occur over almost the entire range of pH. Hydrolysis and condensation leading to formation of  $\text{Ba(OH)}_2$  is prevented in the neutralization of barium acetate aqueous solution. Instead, it is believed that the strong complexation tendency gives rise to the formation of amorphous barium acetate gels. On the other hand, the  $[\text{Ba-Cl}]$  complexes are stable only at  $3 < \text{pH} < 8$ . As a result, the precipitation of barium hydroxide from  $\text{BaCl}_2$  solution will proceed from  $[\text{Ba(OH)(H}_2\text{O)}_5]^+$  in strong alkaline medium in which  $\text{Cl}^-$  acts as a counter ion in solution. In the case of  $\text{BaTiO}_3$  particle formation, it is expected that  $\text{BaTiO}_3$  forms in an alkaline medium by either homogeneous reaction between the aqueous species  $[\text{BaOH}]^+$  and  $[\text{Ti(OH)}_4]^0$  or heterogeneous reaction between the aqueous species  $[\text{BaOH}]^+$  and solid  $\text{TiO}_2 \cdot x\text{H}_2\text{O}$  depending upon reaction conditions and type of precursors. This is in good agreement with the prediction of the phase stability diagram as shown in Figure 3-3. The anionic species involved in the hydrothermal reaction must also be properly selected since they can significantly influence behavior of the aqueous species.  $\text{BaTiO}_3$  with different particle morphology or surface characteristics can be produced by controlling the type of anionic species present.

### Conclusions

Thermodynamic modeling approaches to simulate hydrothermal synthesis can serve as road maps for establishing reaction paths for material synthesis, or as predictive tools on the behavior of a given phase in different aqueous environments. Modeling can be used to evaluate and select the appropriate precursor system which should be both reactive and cost-effective in a given reaction condition. However, validity of the phase stability diagram significantly depends on the availability and accuracy of the thermodynamic data for the relevant reaction species, especially aqueous solution complexes. Unfortunately, little information on the essential solution complexation is available in the literature, especially at elevated temperatures and pressures. In this regard, the Partial Charge Model

provides a basic understanding of the aqueous chemistry of metal cations. It shows how hydrolysis, condensation, and complexation reactions can be described in terms of three parameters such as the charge of the cation, the pH of solution, and the mean electronegativity of the chemical species. However, other important chemical parameters such as temperature, pressure, ionic strength or metal concentration must be incorporated in this model. Therefore, a combination of the two theoretical approaches is required to fully understand the chemical reactions and particle formation mechanisms in hydrothermal particle synthesis, although both give no hint of kinetic feasibility.

## CHAPTER 4 HYDROTHERMAL SYNTHESIS OF BaTiO<sub>3</sub>

### Introduction

Significant efforts are focused on reducing particle synthesis temperatures. The primary advantage of low temperature particle synthesis includes the cost-effective production of small grained powders. The stability diagram of Ba-Ti-H<sub>2</sub>O system predicted that BaTiO<sub>3</sub> is thermodynamically stable even at room temperature in a highly alkaline medium, as shown in Figure 3-2. However, sluggish reaction kinetics usually prevent crystallization of BaTiO<sub>3</sub> at 25°C. To decrease the synthesis temperature, therefore, a more reactive precursor system is required in which the reaction components are intimately mixed and which in turn experiences a shorter diffusion pathway during chemical reaction.

Amorphous Ti gels (TiO<sub>2</sub>·xH<sub>2</sub>O) are preferred over relatively insoluble anhydrous titanium oxide in the low temperature hydrothermal synthesis of BaTiO<sub>3</sub>. Hydrous gels are generally prepared by neutralization from TiCl<sub>4</sub>. Such gels were determined to be more reactive since they have a larger surface area and open structure [144]. Titanium alkoxides have also been utilized in order to lower synthesis temperatures and to prevent anionic contamination, particularly by chloride ions, even though the metal alkoxides are relatively expensive. However, the high reactivity of the alkoxides towards moisture tends to result in undesirable, uncontrolled hydrolysis and condensation reactions, and eventually may cause chemical inhomogeneity in the final ceramic product [145, 146]. To solve this problem, chelating agents such as glacial acetic acid or acetylacetone have been used to modify the reactivity of the alkoxide in the sol-gel synthesis [145-148]. However, there have been no previous studies on barium titanate hydrothermal synthesis involving modified metal alkoxide precursors. In the current chapter, an acetylacetone-modified

titanium isopropoxide is used as the Ti source. From this modified Ti alkoxide and barium acetate, the hydrous Ba-Ti complex gel suspension has been prepared and hydrothermally treated under an open or closed system in an inert atmosphere.

### Background

Reaction behavior of the transition metal alkoxides is determined by both the intrinsic and extrinsic aspects of the alkoxides and the thermodynamic system in which they reside. The inherent characteristics of the metal such as the radii, electronegativity, and oxidation state are important as well as the environment of the metal such as the nature of alkoxy group and any substitutional ligands [149]. A change in the reaction activity of the alkoxide can give a different molecular structure and reaction pathway and substantially result in particles with different morphologies and even phases, depending upon the environments of the starting metal alkoxides [140]. Thus, the chemical factors that permit better control of hydrolysis and condensation of precursors will play a critical role in alkoxide-based solution synthesis.

Chemical control of the alkoxide can be performed by adding complexing reagents that react with metal alkoxides at a molecular level, giving rise to new molecular precursors of different structure, reactivity, and functionality. Chemical modifiers include hydroxylated nucleophilic ligands, such as carboxylic acids and  $\beta$ -diketones. The  $\beta$ -diketones generally exist as an equilibrium mixture of the tautomeric keto and enol forms as shown in Figure 4-1 [150]. Among  $\beta$ -diketones, in particular, a small addition of acetylacetone (2,4-pentanedione [ $\text{CH}_3\text{-CO-CH}_2\text{-CO-CH}_3$ ]) significantly changes the hydrolysis and condensation behavior of the alkoxides [151]. Its enolic form contains hydroxyl groups and reacts with metal alkoxides as a chelating ligand. Acetylacetone behaves as a nucleophilic reactant and replaces the alkoxy group. In the hydrolysis reaction of acetylacetonate alkoxides, less electronegative ligands (alkoxy groups) are rather quickly withdrawn while the more electronegative ligands (acetylacetonate groups) persist as a

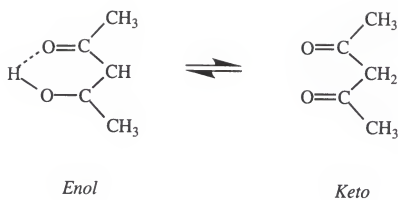


Figure 4-1. Tautomerism of acetylacetone [150].

complex ion within the metallic group [152, 153]. Such modified alkoxides have been used in the preparation of powders, thin films, and fibers with the additional advantages of handling, and long term storage in conjunction with their strong stability against hydrolysis [147, 154, 155]. It was demonstrated that the use of a modified organometallic precursor leads to better homogeneity, enhanced mechanical and physical properties, and a reduction in synthesis temperature. In the present study, hydrothermal synthesis of phase-pure perovskite  $\text{BaTiO}_3$  characterized by the use of a modified titanium alkoxide by acetylacetone was developed.

### Materials and Methods

The general procedure used to synthesize barium titanate is shown in Figure 4-2. To prepare the coprecipitated gel for synthesis, barium acetate<sup>1</sup> was dissolved in  $\text{CO}_2$ -free deionized water. Throughout the process,  $\text{CO}_2$ -free deionized water was used in the preparation of all the aqueous solutions. Preliminary experiments indicated that the use of water without minimizing  $\text{CO}_2$  invariably resulted in the formation of  $\text{BaCO}_3$  as a contaminant in the hydrothermally treated feedstock, as predicted in the stability diagram in Figure 3-3(b). The aqueous barium acetate solution was filtered through 0.22  $\mu\text{m}$  filter paper.<sup>2</sup>

The modification of titanium (IV) isopropoxide<sup>3</sup> was achieved by adding acetylacetone<sup>4</sup> (denoted as acacH) in a ratio of  $\text{Ti}:\text{acacH} = 1:1$ . The modified alkoxide was diluted with ethanol to obtain a stable sol solution through an alcohol interchange reaction between the ethoxy and propoxy groups, followed by filtration through 0.22  $\mu\text{m}$  filter paper. Each standard solution was mixed to the desired Ba:Ti ratio ( $\text{Ba}:\text{Ti} = 1:1$ ). Metal hydrous precursors were precipitated by addition of the yellow homogeneous sol solution into KOH while stirring under an inert Ar atmosphere. To control the pH of the precursor

<sup>1</sup>Fisher Scientific, Pittsburgh, PA.

<sup>2</sup>MSI, Westboro, MA.

<sup>3</sup>Aldrich Chemical Co., Milwaukee, WI.

<sup>4</sup>Aldrich Chemical Co., Milwaukee, WI.

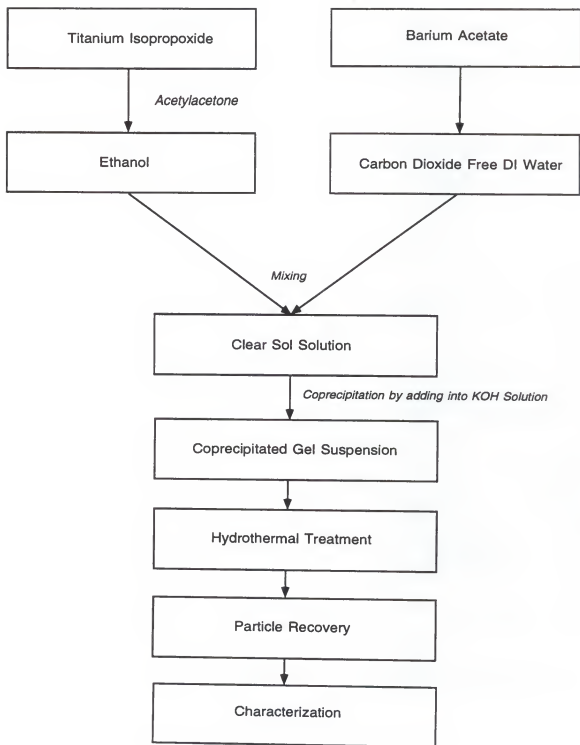


Figure 4-2. Processing procedure used for preparing BaTiO<sub>3</sub> powder by hydrothermal method.

suspension, the concentration of KOH solution was varied from 0.1 M to 1.0 M. After coprecipitation, the suspension pH was measured and recorded. Characteristics of the coprecipitated gel were examined by transmission electron microscopy (TEM),<sup>5</sup> thermal gravimetry analysis, and differential thermal analysis (TGA/DTA).<sup>6</sup>

Hydrothermal reactions were performed at temperatures ranging from 40°C to 150°C in either a 23 ml Teflon lined acid digestion bomb or 600 ml-capacity autoclave with a magnetically driven stirrer,<sup>7</sup> as shown in Figure 4-3. The feedstock concentration ranges from 0.025 to 0.1 M. The resulting hydrothermally treated powders were repeatedly washed by centrifugation and decantation with pH adjusted deionized water (pH 9.5 - 9.6) and dried in a vacuum oven for 24 hours at 120°C. The phase composition of the recovered products was determined by X-ray diffractometry (XRD)<sup>8</sup> over a  $2\theta$  range from 20-60° at a scan rate of 2.4°/min. Morphology of the particles was determined using a scanning electron microscope.<sup>9</sup> Particle size analysis was performed by a centrifugal sedimentation technique.<sup>10</sup>

The synthesized BaTiO<sub>3</sub> powders were uniaxially-pressed at 80 MPa into discs with a 6.4 mm in diameter and approximately 2 mm in thickness. The sample was sintered in a tube furnace in air at 1300°C for 3 hours. Bulk density was measured by standard Archimedes method in methanol. The sintered pellet was polished using 0.3  $\mu$ m alumina paste. The polished sample was ultrasonically cleaned in an acetone for 30 min and thermally etched at 1200°C for 1 hour for microstructural examination using SEM. To determine dielectric properties, an Au-Pd electrode layer was sputter coated on the polished sample followed by coating with a silver paste. The capacitance and dissipation factor were measured as a function of temperature and frequency using AC impedance analyzer.<sup>11</sup>

---

<sup>5</sup>JEOL 200CX, Boston, MA.

<sup>6</sup>Seiko SSC5200, Chiba, Japan.

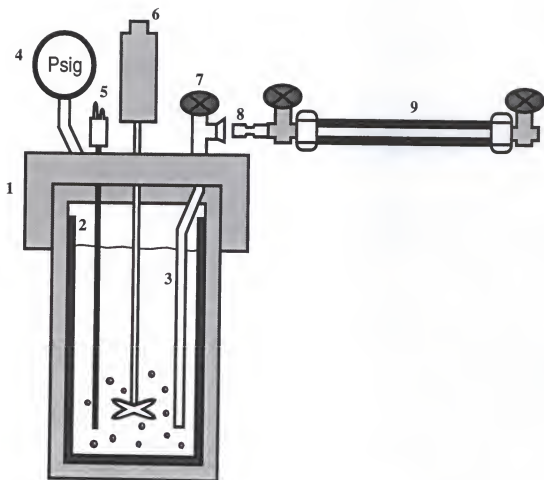
<sup>7</sup>Model 4560, Parr Instrument Company, Moline, IL.

<sup>8</sup>Philips APD 3720, Mahwah, NJ.

<sup>9</sup>JEOL JSM 6400, Boston, MA.

<sup>10</sup>Horiba CAPA-700, Irvine, CA.

<sup>11</sup>HP 4192A, LF Impedance Analyzer, Hewlett Packard. Co., San Francisco, CA.



- |                        |                                   |
|------------------------|-----------------------------------|
| 1. 316 Stainless Steel | 6. Magnetically Driven Stirrer    |
| 2. Teflon Liner        | 7. Valve                          |
| 3. Dip Tube            | 8. Quick Connect Joint            |
| 4. Pressure Gauge      | 9. High Temperature Sampling Unit |
| 5. Thermocouple        |                                   |

Figure 4-3. The schematic diagram showing a 600 ml-capacity hydrothermal reactor used for preparing  $\text{BaTiO}_3$  powders.

## Results and Discussion

### Characteristics of the Coprecipitated Ba-Ti Complex Gel

The obtained coprecipitated gels were dried at 100°C for 18 hours prior to analysis. Phase of the as-precipitated Ba-Ti gel was determined as amorphous under both X-ray and electron beam conditions based on observation of broad scattering peaks and diffuse ring structures, respectively. As shown in the TEM micrograph of Figure 4-4(a), the current precursor exhibited a very fine structure with the typical morphology of the gel. For TGA/DTA analysis, the sample was heated to 800°C under atmospheric conditions at a rate of 10°C/min. TGA/DTA curves of Figure 4-4(b) indicate that the dried amorphous gel had 35.5 % total weight loss. The weight loss around 200°C is due to the dehydration from the hydrous amorphous gel structure and the weight loss at about 400°C is related to the decomposition of the residual organic groups. It is believed that the sharp DTA peak at 600°C results from phase transformation from amorphous gel to cubic BaTiO<sub>3</sub>.

### Influence of Reaction Conditions on Phase Composition

The pH of the reaction medium has a significant effect on the formation of barium titanate. The precursor suspensions with six different pH values (from 9 to 14) were hydrothermally treated at 150°C for 18 hours. Detailed reaction conditions are summarized in Table 4-1. From X-ray analysis, it was determined that the production of phase-pure BaTiO<sub>3</sub> requires highly alkaline conditions (pH>13) as shown in Figure 4-5. Below a pH value of 13, the products were amorphous except for minor barium carbonate phase. However, barium titanate began to form above pH 13 and well-crystallized phase-pure BaTiO<sub>3</sub> was synthesized in solutions above pH 14. Other titanates such as Ba<sub>2</sub>TiO<sub>4</sub> or BaTi<sub>2</sub>O<sub>5</sub> were not observed.

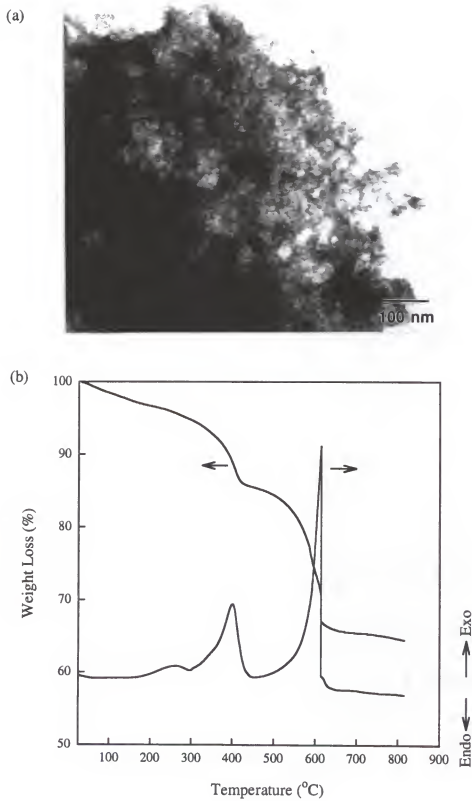


Figure 4-4. Characterization of the coprecipitated Ba-Ti gel: (a) TEM micrograph; and (b) TG/DTA curves.

Table 4-1. Influence of pH of Hydrothermal Reaction Medium on the Phase Composition

Sample ID	BAT-1	BAT-2	BAT-3	BAT-4	BAT-5	BAT-6
Molar Ratio (Ba:Ti:acacH <sup>a</sup> )	1:1:1	1:1:1	1:1:1	1:1:1	1:1:1	1:1:1
Concentration	0.1M	0.1M	0.1M	0.1M	0.1M	0.1M
Hydrothermal Reaction Conditions	150°C, 18h	150°C, 18h	150°C, 18h	150°C, 18h	150°C, 18h	150°C, 18h
Initial pH	9.23	10.12	11.02	12.01	13.05	14.20
Final pH	5.88	8.30	10.78	11.80	12.90	14.19
Primary Phase	AM <sup>b</sup>	AM	AM	AM	BT <sup>d</sup>	BT
Minor Phases		BC <sup>c</sup>	BC	BC		

acacH<sup>a</sup> : AcetylacetoneAM<sup>b</sup> : Amorphous PhaseBC<sup>c</sup> : BaCO<sub>3</sub>BT<sup>d</sup> : Cubic BaTiO<sub>3</sub>

Differences in the X-ray intensities in Figure 4-5 underscore the importance of the solution pH (i.e., the concentration of  $\text{OH}^-$ ) in formation of barium titanate. The thermodynamically calculated stability diagram of the Ba-Ti system in Figure 3-3(a) predicts that barium titanate can be precipitated in a wide pH range from 9 to 14 at appropriately selected synthesis conditions, such as  $\text{Ba}^{2+}$  concentration and  $\text{CO}_2$  environment [130, 134]. As indicated in Figure 4-5, however, a highly alkaline condition ( $\text{pH} > 13$ ) is necessary to promote  $\text{BaTiO}_3$  formation within a reasonable reaction time. To initiate transformation from solution with a low degree of supersaturation, in particular, higher pH is required as compared to high feedstock concentration condition [134]. Therefore, the higher solution pH values required to synthesize  $\text{BaTiO}_3$  imply that the hydroxyl species ( $\text{OH}^-$ ) has an important kinetic role in the formation of barium titanate under hydrothermal conditions. However, hydrothermal synthesis at a highly alkaline condition can cause problems. The purity of the product can be deteriorated by the KOH mineralizer used to control the pH. Furthermore, a considerable amount of  $\text{H}_2\text{O}$  and  $\text{OH}^-$  can be incorporated into the lattice, as demonstrated by Vivekanandan and Kutty. [156]. The occupation of  $\text{OH}^-$  species at the oxygen lattice sites gives rise to formation of cation vacancies, which in turn introduce microstrains in the hydrothermally derived barium titanate.

To determine the lowest synthesis temperature, the feedstock suspensions with  $\text{pH} > 13.5$  were aged at room temperature and placed in an oven at temperatures of  $40^\circ\text{C}$ ,  $50^\circ\text{C}$ , and  $60^\circ\text{C}$  using 23 ml acid digestion bombs for 12 hours. As shown in Figure 4-6, the phase of the sample aged at room temperature was amorphous and a small amount of barium titanate formed in the case of the sample treated at  $40^\circ\text{C}$  although the majority was barium carbonate. At  $50^\circ\text{C}$ , phase pure  $\text{BaTiO}_3$  was synthesized, but it was mixed with unreacted amorphous precursor whereas well-crystallized  $\text{BaTiO}_3$  was obtained at  $60^\circ\text{C}$  within this reaction time. Transformation of amorphous Ba-Ti gel into the crystalline  $\text{BaTiO}_3$  will involve a breakage of Ti-O-Ti bonds and incorporation of  $\text{Ba}^{2+}$  in the

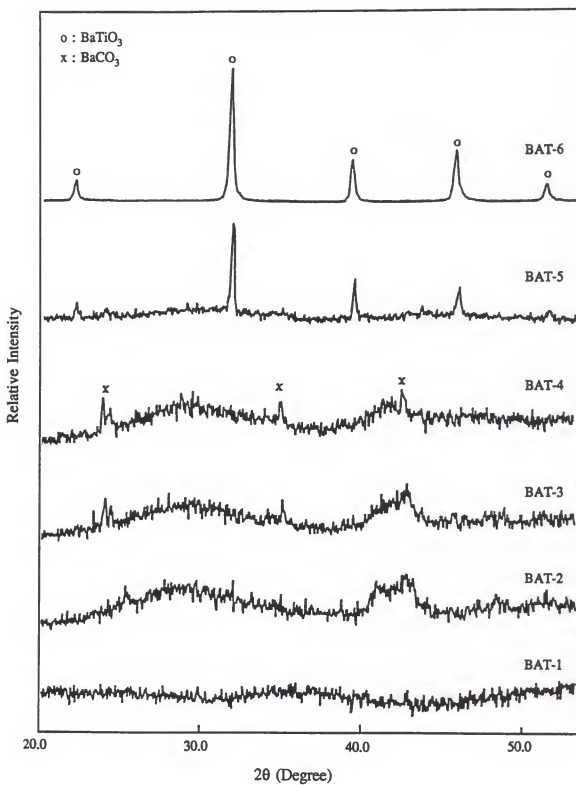


Figure 4-5. XRD patterns of the products prepared as a function of pH at  $150^\circ\text{C}$  for 18 hours.

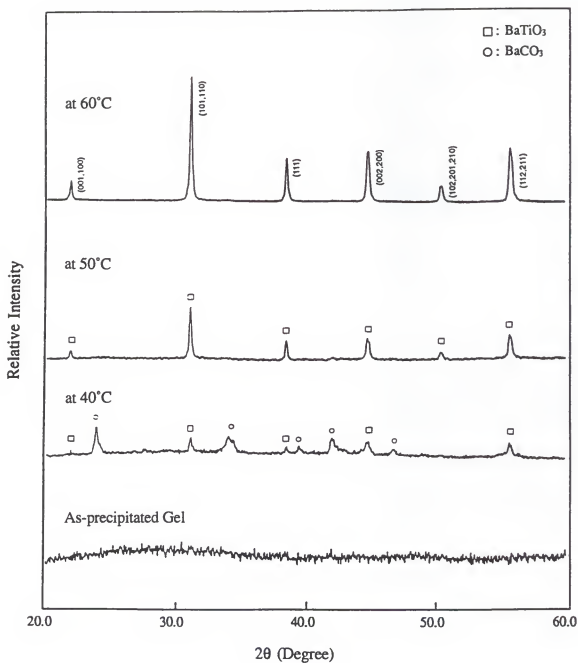


Figure 4-6. XRD patterns of the products prepared as a function of synthesis temperature at the solution  $\text{pH} > 13.5$  reacted for 12 hours.

perovskite lattice structure regardless of formation mechanism [157]. For such a transformation, the energy barrier, which is closely related to the nature of the rate controlling step in the dominant formation process, must be overcome. In the current material system, the transformation temperature from amorphous gel to crystalline barium titanate is taken to be around 50°C and fast conversion requires greater thermal energy to overcome the energy barrier for crystallization.

### Influence of Reaction Conditions on Particle Size

SEM micrographs of the hydrothermally derived BaTiO<sub>3</sub> at different reaction conditions are shown in Figure 4-7. Barium titanate has a relatively spherical shape and particle size ranging from 0.05 to 0.35 µm, as estimated by SEM. It was determined that the average particle size was controlled by reaction conditions such as reaction concentration, temperature, and time. An increase in particle size was observed as a function of reaction time at low temperature while there was no such tendency at high temperature. At the concentration of 0.1 M, for example, the particle size of BaTiO<sub>3</sub> synthesized at 75°C for 30 min was approximately 0.05 µm, which increased to 0.09 µm after 4 hours of further reaction. However, the product particle size (~0.15 µm) prepared at 150°C for 1 hour remained nearly constant relative to a hydrothermal treatment at 150°C for 4 hours. This is because particle growth is very fast at high reaction temperatures and the reaction is virtually complete within 1 hour. Reaction concentrations also influenced the particle size. The size of barium titanate particles obtained from 0.05 M feedstock concentration at 150°C for 1 hour was approximately 0.20 µm while the size produced by a 0.025 M feedstock at 150°C for 1 hour was 0.35 µm.

Barium titanate obtained from a 0.1 M feedstock at 150°C for 4 hours was selected to evaluate the particle size distribution. The particle size distribution is shown in Figure 4-8. Particles were suspended in methanol and then analyzed. Based on the cumulative volume frequency, the probability *t* values were collected from the Standard Mathematical

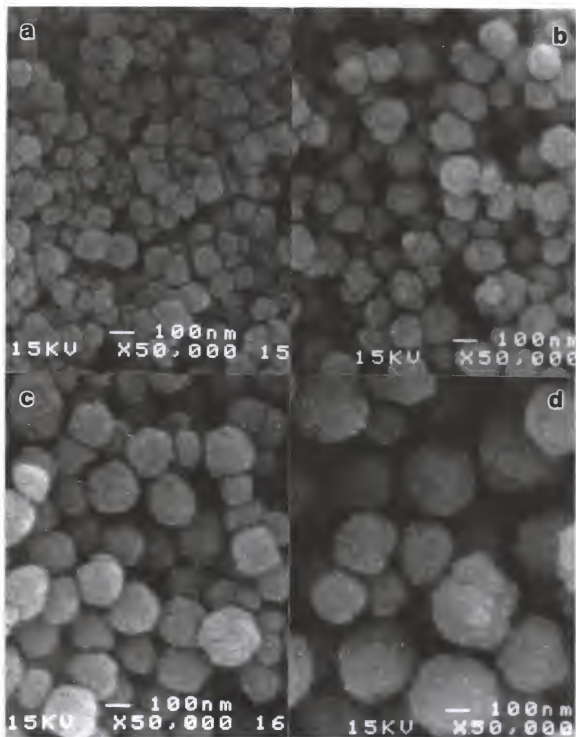


Figure 4-7. SEM micrographs of the prepared  $\text{BaTiO}_3$  powders as a function of reaction parameters such as reaction concentration, temperature, and time, respectively: (a) 0.1 M-75°C-4 hours; (b) 0.1 M-150°C-1 hour; (c) 0.05 M-150°C-1 hour; and (d) 0.025 M-150°C-1 hour.

table for the normal distribution [158, 159]. Subsequently, a linear regression was performed on the plot of log normal probability of particle size on the y-axis against the probability t-values on the x-axis in the range of cumulative percent from 15% to 85%. From the obtained line equation, the value at  $t=0$  (i.e., 50% of cumulative frequency) is a median equivalent spherical diameters ( $X_{50}$ ) and the difference in the values at  $t=0$  and  $t=1$  is the standard deviation ( $\sigma$ ). Barium titanate particles have a median diameter of  $0.23\ \mu\text{m}$  and standard deviation of  $\pm 0.13$ .

If crystallites of materials are smaller than a certain critical size, the high temperature phase can be stable below the thermodynamic stability range.  $\text{BaTiO}_3$  has a phase transition from the paraelectric cubic phase to ferroelectric tetragonal structure at around  $120^\circ\text{C}$  as shown in Figure 2-2. However, the phase of the synthesized submicron  $\text{BaTiO}_3$  particles is usually cubic perovskite unless the particle size is larger than  $1\ \mu\text{m}$ . The critical particle size to exhibit tetragonality is known as  $0.12\ \mu\text{m}$  and this tetragonality increases with increasing particle size as demonstrated by Dutta et al. [25, 160-162]. Furthermore, sintered  $\text{BaTiO}_3$  shows cubic structure at  $25^\circ\text{C}$  with decreasing grain size below  $1\ \mu\text{m}$ , exhibiting unique ferroelectric domain structure and dielectric behavior [163]. It was proposed that this room-temperature stabilization of cubic phase is attributed to a surface effect of particle or grain size [54, 161]. To verify such a relationship between crystallite size and material properties, the particulate material system is appropriate due to the absence of residual stress, unlike the sintered material. High purity, homogeneous particles are necessary to avoid the complications caused by impurities or inhomogeneities. In this regard, the current hydrothermally derived  $\text{BaTiO}_3$  can be an ideal system in which a wide range of synthesizable particle sizes can allow systematic study of the particle size effect on the crystal structure and related dielectric properties.

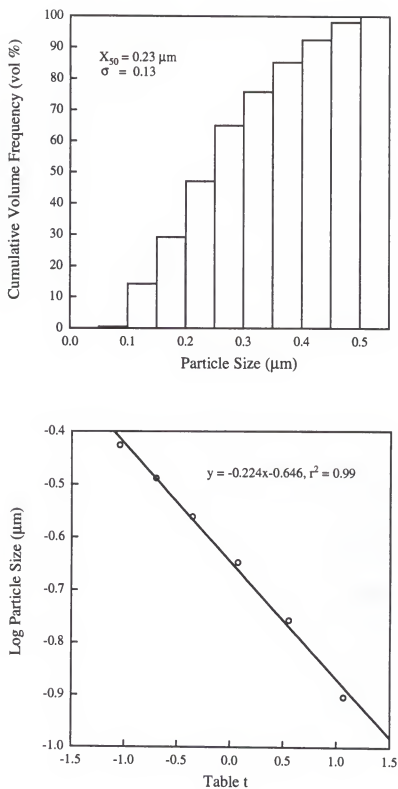


Figure 4-8. Particle size distribution of the synthesized particles.

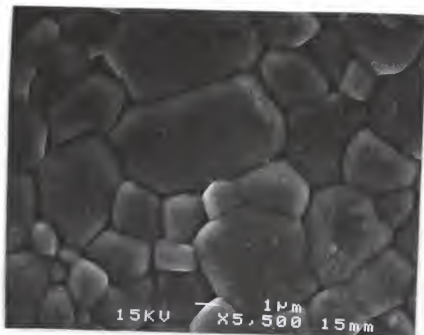
### Dielectric Properties of Hydrothermally Derived Barium Titanate

As part of the evaluation of the hydrothermally derived  $\text{BaTiO}_3$  from the coprecipitated Ba-Ti gel, the sintering behavior and the dielectric properties were investigated. The cubic  $\text{BaTiO}_3$  synthesized at  $150^\circ\text{C}$  for 4 hour was used. Figure 4-9 shows the microstructure of the sintered  $\text{BaTiO}_3$  at  $1300^\circ\text{C}$  for 3 hours including both the fractured and polished surfaces. The distribution of grain sizes are relatively broad ranging from 2 to 8  $\mu\text{m}$ , indicating the presence of abnormal grain growth as shown in Figure 4-9[a]. The density of the sintered pellet was  $5.38 \text{ g/cm}^3$ , which corresponds to 89.1% of the theoretical density. Pores were preferentially located between the grains (i.e., intergranular porosity). The dielectric constant and dissipation factor for this sample are shown in Figure 4-10(a) and (b). The dielectric constant and dissipation factor at 1 kHz,  $26^\circ\text{C}$  was 1923 and 0.7 %, respectively. Dielectric constants exhibited a sharp peak around  $125^\circ\text{C}$  ( $\pm 5$ ), reflecting the Curie temperature for cubic-to-tetragonal phase transition occurs near this temperature region.

### Hydrothermal Synthesis of Other Ferroelectric Ceramics

The currently developed hydrothermal procedure has been applied to synthesize other titanium-based perovskite ferroelectric ceramics such as  $\text{SrTiO}_3$ ,  $\text{PbTiO}_3$ , PZT, and PLZT. Starting from the acetylacetone-treated Ti isopropoxide and metal acetate salts, such ferroelectrics particles were hydrothermally produced at much lower temperatures than previously reported. The lowest synthesis temperature for  $\text{SrTiO}_3$ , PZT, and PLZT was  $110^\circ\text{C}$  while  $150^\circ\text{C}$  for  $\text{PbTiO}_3$ . Solution pH plays an important role in determining phase composition of the hydrothermal reaction products. The phase-pure ferroelectric powders with perovskite structure were prepared only at a highly alkaline condition, similar to the synthesis of  $\text{BaTiO}_3$ . Particle size and morphology were also significantly influenced by reaction concentration as shown in Figure 4-11 and 4-12. The particle size of the hydrothermally derived ferroelectrics decreases as the feedstock concentration increases. It

(a)



(b)

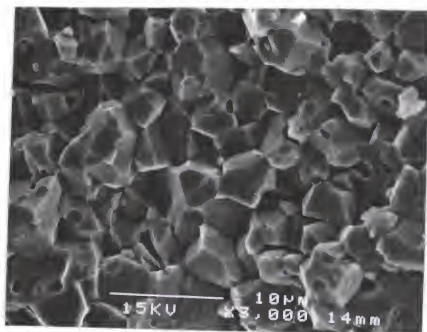


Figure 4-9. SEM micrographs showing the microstructure of the sintered BaTiO<sub>3</sub> at 1300°C for 3 hours followed by thermal etching 1200°C for 1 hour: (a) polished surface; and (b) fractured surface.

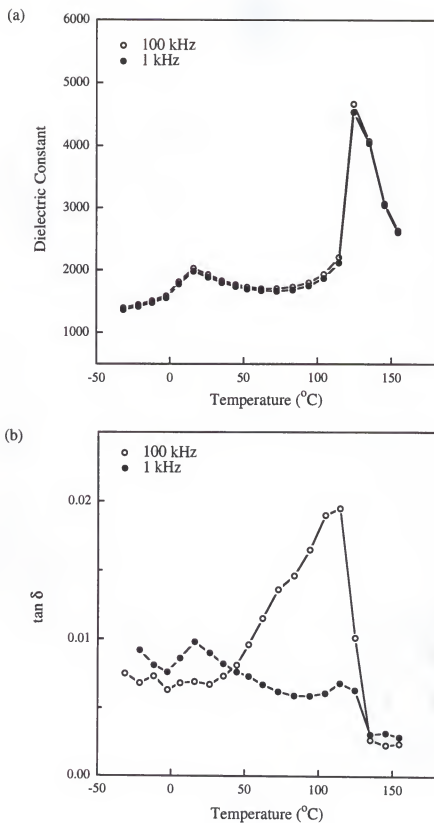
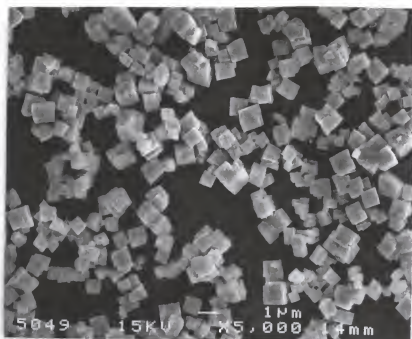


Figure 4-10. Dielectric constant and dielectric loss as a function of temperature for the hydrothermally derived  $\text{BaTiO}_3$ .

(a)



(b)

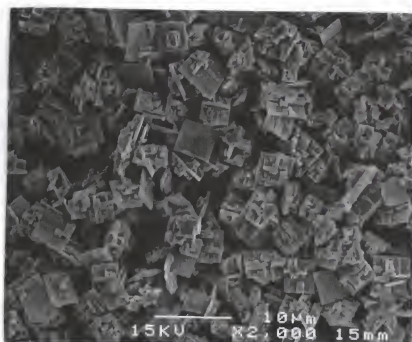
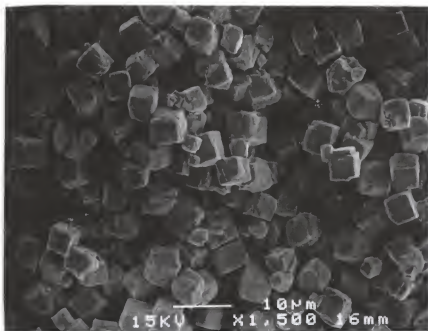


Figure 4-11. SEM micrographs of the hydrothermally derived ferroelectric  $\text{PbTiO}_3$  powders: (a) at 0.1 M-150°C-18 hours; and (b) at 0.05 M-150°C-18 hours.

(a)



(b)

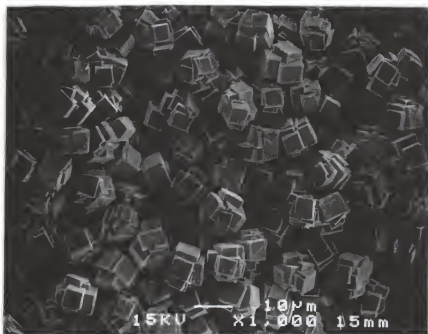


Figure 4-12. SEM micrographs of the hydrothermally derived ferroelectric PLZT powders: (a) at 0.1 M-150°C-18 hours; and (b) at 0.05 M-150°C-18 hours.

is probably because increased number of the small particles tend to precipitate rapidly from a highly saturated solution with greater driving force, as indicated in the equation [2.10]. Furthermore, it was demonstrated that stoichiometry of the ferroelectric powders can be precisely controlled in this hydrothermal synthesis process. For instance, the morphotropic phase boundary between the tetragonal and rhombohedral phases for PZT was observed at the molar ratio of Zr:Ti = 0.49:0.51 as shown in Figure 4-13.

### Influence of the Chemically Modified Titanium Precursor

The ability to synthesize ferroelectric ceramic powders at low temperatures can be related to the unique molecular structure of the current precursor system. Acetylacetone (acacH) reacts with titanium (IV) isopropoxide as a chelating agent. For a stoichiometric reaction of Ti/acac = 1, the nucleophilic reaction of acacH leads to formation of a new monomeric Ti precursor as follows:



Leaustic et al. investigated the molecular structure of titanium isopropoxide during chemical modification using X-ray absorption near edge spectroscopy (XANES) and extended X-ray absorption Fourier spectroscopy (EXAFS) [152, 153]. It was shown that the coordination number of titanium increases from four ( $\text{Ti}(\text{OPr}^i)_4$ ) to five ( $\text{Ti}(\text{OPr}^i)_3\text{acac}$ ) by the modification with acetylacetone, then to six ( $\text{Ti}(\text{OH})_x(\text{OEt}^i)_{3-x}\text{acac}$ ) with oligomeric species formed during the dilution with ethanol. Chemical modification significantly increases the stability of the titanium alkoxide against moisture, leading to a water-soluble titanium precursor instead of forming an extensively polymerized Ti gel [147]. As a consequence, such modified Ti alkoxide is hydrolyzed and condensed in a relatively controlled manner so that stable colloidal titania forms in a wide range of pH from 2 to 10. It was determined that the colloidal  $\text{TiO}_2$  has an anatase-like structure and its particle size ranges from 3 to 6 nm. The acetylacetonate modification processes for titanium isopropoxide followed by dilution with ethanol and hydrolysis are schematically depicted in Figure 4-14.

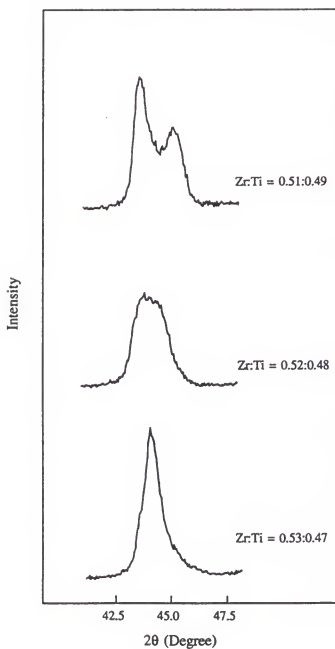


Figure 4-13. X-ray diffraction patterns indicating morphotropic boundary between the tetragonal and rhombohedral PZT as a function of the molar ratio of Zr:Ti. The reactions were performed at 150°C for 18 hours.

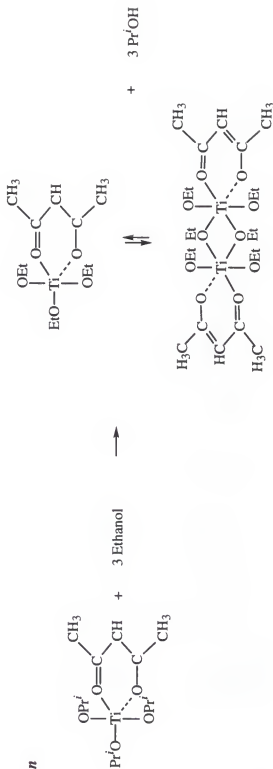
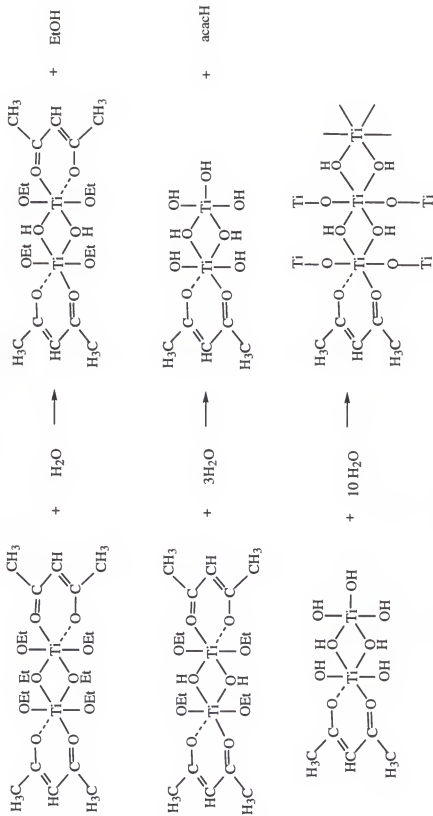
**Modification****Dilution**

Figure 4-14. Chemical modification process of titanium isopropoxide by acetylacetone where  $\text{OPr}^i$  and  $\text{OEt}$  represent the propoxy and ethoxy group, respectively [149].

## Hydrolysis

Figure 4-14. (continued) Chemical modification process of titanium isopropoxide by acetylacetone where  $\text{OEt}$  represents the ethoxy group [149].

The chemical modification process of titanium isopropoxide can be understood in the frame of charge distributions in the Ti precursors which are calculated based on the partial charge model, as described in Chapter 3 [137, 148]. It was determined that titanium has a high positive charge ( $\delta = +0.66$ ) in  $\text{Ti}(\text{OPr}^i)_4$  and the full coordination of Ti is not yet satisfied. Therefore nucleophilic addition of acacH is possible giving rise to the transition state  $\text{Ti}(\text{OPr}^i)_4(\text{acacH})^*$ . The charge distribution in this state suggests that acacH is negatively charged ( $\delta = -0.52$ ) while  $\text{Pr}^i\text{OH}$  is positively charged ( $\delta = 0.05$ ). The propoxy group is then removed leading to the substituted alkoxide  $\text{Ti}(\text{OPr}^i)_3(\text{acac})$ . Hydrolysis of this modified precursor proceeds via nucleophilic addition of  $\text{H}_2\text{O}$  involving the transition state  $\text{Ti}(\text{OPr}^i)_3(\text{acac})(\text{H}_2\text{O})^*$ . The charge distribution calculation indicates that both acacH and  $\text{H}_2\text{O}$  are negatively charged ( $\delta = -0.52$  and  $-0.26$ , respectively) while the  $\text{Pr}^i\text{OH}$  is positively charged ( $\delta = 0.12$ ). Consequently, another  $-\text{OPr}^i$  group is replaced first instead of  $-\text{acac}$ . The acetylacetonate group is not easily removed through hydrolysis and condensation due to strong complexing ability. This partial charge model is in well agreement with the above experimental observations for chemical modification. The calculated partial charge distribution in the Ti precursor during modification is summarized in Table 4-2.

In the current synthesis procedure, the use of this modified titanium isopropoxide allows homogeneous solution mixing without forming heterogeneous precipitation when the aqueous barium solution is introduced. The subsequent addition of such clear precursor solution into KOH results in a stoichiometric coprecipitated hydrous gel (i.e.,  $[\text{BaTi}(\text{OH})_x\text{O}_y(\text{acac})_z]$ ) in which Ba and Ti species are intimately incorporated in the nanometer scale instead of forming individual titanium hydrous gel and barium acetate gel. It is expected that the barium ions are absorbed on the surface of the amorphous Ti gel without incorporation in the network structure of Ti gel. Schematic picture illustrating a proposed structure of the coprecipitated Ba-Ti gel is presented in Figure 4-15. In this gel

Table 4-2. Charge Distribution in Ti Precursor during Chemical Modification by Acetylacetone

Species	$\bar{\chi}_p$	$\delta(\text{Ti})$	$\delta(\text{OPr})$	$\delta(\text{Pr}^i\text{OH})$	$\delta(\text{acac})$	$\delta(\text{acacH})$	$\delta(\text{H}_2\text{O})$	$\delta(\text{OH})$
$\text{Ti}(\text{OPr})_4$	2.35	0.66	-0.16	-	-	-	-	-
$\text{Ti}(\text{OPr})_4(\text{acacH})^*$	2.37	0.67	-0.04	0.05	-0.60	-0.52	-	-
$\text{Ti}(\text{OPr})_3(\text{acac})$	2.37	0.67	-0.03	0.06	-0.59	-0.51	-	-
$\text{Ti}(\text{OPr})_3(\text{acac})(\text{H}_2\text{O})^*$	2.38	0.68	0.03	0.12	-0.52	-0.43	-0.26	-
$\text{Ti}(\text{OPr})_2(\text{acac})(\text{OH})$	2.39	0.68	0.07	0.16	-0.47	-0.38	-0.25	-0.34

\*Transition state

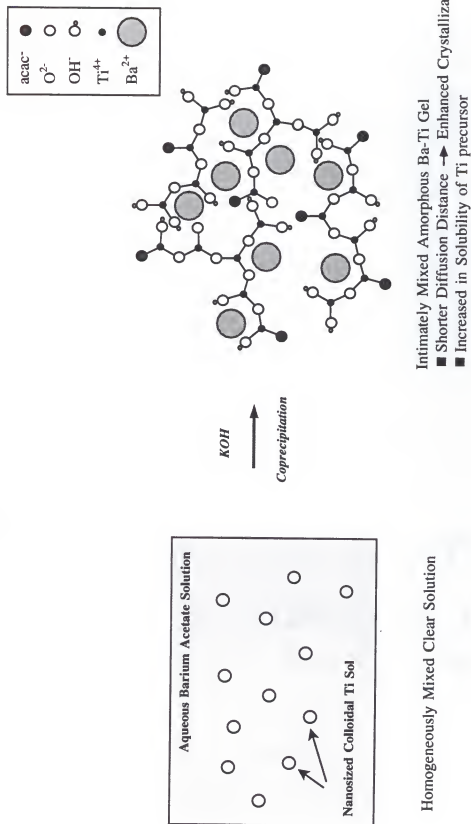


Figure 4-15. Schematic picture illustrating structure of the coprecipitated Ba-Ti complex gel.

structure, however, the acetate group may still exist in the form of  $\text{Ba}(\text{CH}_3\text{COO})^+$  due to its strong complexing ability as shown in Figure 3-8. Furthermore, it is likely that the acetylacetonate group is still attached to the Ti. As shown in the TGA/DTA curves (Figure 4-4), as a result, substantial weight loss between 400 and 600°C is probably associated with decomposition of these acetylacetonate and acetate groups.

During hydrothermal treatment of the current coprecipitated metal hydrous gel, it is believed that barium species have a shorter diffusion distance for reaction with the Ti gel. More possibly, the strong complexing ability of acetylacetone towards Ti may increase the solubility of the hydrous Ti gel at elevated temperature and pressure. Therefore, this combined effect significantly reduces the hydrothermal synthesis temperature.

### Conclusions

The use of stable modified titanium alkoxide with acetylacetone and barium acetate has led to an amorphous Ba-Ti hydrous gel in which the reacting species are homogeneously mixed. From these precursors, barium titanate with a cubic perovskite structure has been synthesized under hydrothermal conditions. It was demonstrated that  $\text{BaTiO}_3$  can be obtained at temperatures as low as 50°C. For the formation of phase-pure  $\text{BaTiO}_3$ , the critical conditions are that the pH of initial reaction medium be above pH 13 and  $\text{CO}_2$  content within the atmosphere be minimized. The resulting products have the average particle sizes ranging from 0.05 - 0.35  $\mu\text{m}$  depending upon reaction parameters such as reaction concentration, temperature and time. Sintering of the hydrothermally derived  $\text{BaTiO}_3$  at 1300°C for 3 hours led to a relatively broad grain structure with exaggerated grain growth. The dielectric properties were determined to be comparable to the conventionally prepared  $\text{BaTiO}_3$ . The dielectric constant and dissipation factor at 1 kHz, 26°C were 1923 and 0.7%, respectively.

## CHAPTER 5

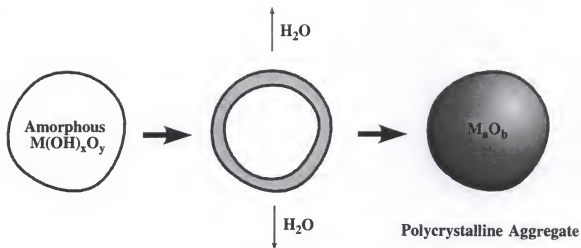
### PARTICLE FORMATION MECHANISMS OF $\text{BaTiO}_3$ UNDER HYDROTHERMAL CONDITIONS

#### Introduction

It is possible to produce crystalline powders with controlled particle size, controlled stoichiometry, and, in some cases, controlled particle shape via a hydrothermal technique. To have the capability to control such particle characteristics in a given material system, particle formation mechanisms must be well understood. However, understanding of the hydrothermal reaction is complex and requires a fundamental knowledge about thermodynamics of solution, solution-solid interactions, and solution chemistry. The theoretical approaches as discussed in Chapter 3 relatively well-establish the thermodynamic foundation for the  $\text{BaTiO}_3$  hydrothermal system. As a consequence, the synthesis conditions for a phase-pure barium titanate from aqueous solution can be easily predicted from the phase stability diagram. However, detailed reaction pathways by which the transformation proceeds are yet to be well-recognized, even though two possible formation mechanisms (i.e., in situ transformation, and dissolution and recrystallization) have been proposed so far, as shown in Figure 5-1. Furthermore, the relatively high temperature and pressure involved in the hydrothermal reactions prohibit in most cases the use of in situ systems to monitor the course of reactions.

Fortunately, the current precursor system, characterized by the unique intimately mixed Ba-Ti complex gel system, can undergo crystallization at temperatures as low as  $50^\circ\text{C}$ , as described in Chapter 4. This low temperature process allows easier sampling throughout the reaction to monitor crystallization behavior and makes it possible to observe microstructural evidence for the reaction mechanism. In the present chapter, therefore, reaction kinetics of  $\text{BaTiO}_3$  from such precursors under hydrothermal conditions is

### *In-situ Transformation*



### *Dissolution and Recrystallization*

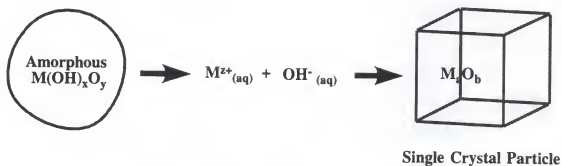


Figure 5-1. Possible formation mechanisms in the hydrothermal particle synthesis [27].

investigated with an emphasis on monitoring microstructural evolution during transformation.

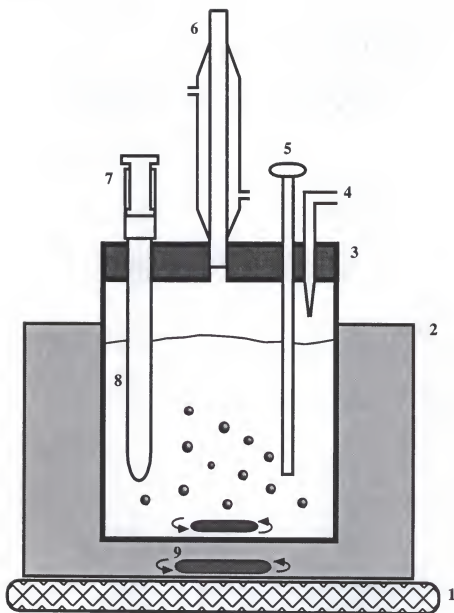
### Materials and Methods

A hydrous coprecipitated gel suspension was prepared as described in Figure 4-2. 1.0 M KOH solution was used to precipitate the hydrous gel from the Ba-Ti precursor sol solution. The pH of the precursor suspension was above 14 and the feedstock concentration was 0.1 M. To monitor the progress of the crystallization below 100°C, a 600 ml teflon reaction vessel fitted with a condenser, thermocouple, gas inlet, and sampling dip tube was used as shown in Figure 5-2. The teflon reactor was submerged into an oil bath which was heated using a hot plate. The reaction was performed at 75°C by adding precursor suspension into the hot reaction vessel under an Ar environment. It took 25 minutes to reach a stabilized reaction temperature and the time at this moment was taken as a zero reaction time to include only isothermal reactions in the kinetic analysis. Samples of 4 ml were collected by syringe as a function of time during the process. The temperature and time, including the pH of the supernatant, were recorded when collecting each sample. In the case of the kinetic study for reaction at 150°C, a 600 ml stainless steel autoclave with sampling capability was used. The solid portion was immediately separated from the mother liquor by centrifugation followed by repeated washing with pH adjusted deionized water (pH 9.5-9.6) to remove the unreacted Ba species. The degree of crystallinity of the product solids were determined by weight-averaged integrated intensity of the (110, 101) X-ray reflection. Commercial barium titanate<sup>1</sup> and starting precursor gels were used as the standard for the fully reacted product and unreacted materials, respectively. Reaction products collected at various reaction times were examined by analytical transmission electron microscopy (TEM) and high resolution TEM (HRTEM).<sup>2</sup>

---

<sup>1</sup>BT-10, Cabot Performance Materials, Boyertown, PA.

<sup>2</sup>JEOL 4000FX, Boston, MA.



- |                  |                     |
|------------------|---------------------|
| 1. Hot Plate     | 6. Condenser        |
| 2. Oil Bath      | 7. Syringe          |
| 3. Teflon Beaker | 8. Dip Tube         |
| 4. Ar Gas Inlet  | 9. Magnetic Stirrer |
| 5. Thermocouple  |                     |

Figure 5-2. Schematic picture of the hydrothermal reactor used for low temperature kinetic study.

### Results and Discussion

Detailed conditions of the extracted samples including reaction time, temperature, and pH of the mother liquid are summarized in Table 5-1. X-ray powder diffractions for the BaTiO<sub>3</sub> crystallization process at 75°C as a function of reaction time are presented in Figure 5-3. The starting precursor was amorphous and transformed into crystalline BaTiO<sub>3</sub> with time. The degree of crystallization in a material can be represented by the gross intensity ( $I_{\text{gross}}$ ) associated with the area under XRD peak. The gross intensity is defined as:

$$I_{\text{gross}} = (\text{Integrated phase counts} / \text{Scan time}) \times (\Delta 2\theta) \quad [5.1]$$

The gross intensity of the (110, 101) reflection in the  $2\theta$  range from 30.2° to 32.5° for each extracted sample was measured using XRD. Crystallization behavior of barium titanate at two different reaction temperatures is shown in Figure 5-4. Qualitatively, the kinetic curve at 75°C exhibits an induction period followed by rapid crystallization and then decreasing conversion reaction. Total reaction was completed within 2 hours at 75°C. On the other hand, much faster crystallization behavior is observed at 150°C without an induction period. This is probably because formation of BaTiO<sub>3</sub> already occurs during heat-up to reaction temperature. Thus, phase-pure BaTiO<sub>3</sub> with the cubic perovskite structure can be synthesized within 5 minutes at 150°C. In order to gain further insight into the formation mechanism of crystalline BaTiO<sub>3</sub>, a Johnson-Mehl-Avrami analysis was performed on the obtained kinetic data based on the following equation [164]:

$$\ln[-\ln(1-f)] = \ln(r) + m \ln(t) \quad [5.2]$$

where  $f$  is the fraction crystallized isothermally at time  $t$ ,  $r$  is the rate constant that partially depends on nucleation frequency and growth rate and is very sensitive to temperature, and  $m$  is the exponent constant that is independent of temperature but sensitive to the time dependence of the nucleation and growth rate and geometry of the particle. Hancock and Sharp have shown that for reactions obeying a single theoretical rate expression, plots of

Table 5-1. Kinetic Data of BaTiO<sub>3</sub> Formation Process at 75°C from the Modified Ti Precursor and Barium Acetate

Sample ID	Reaction time (min)	Temperature (°C)	pH of the supernatant	Fractional crystallinity
BK-01	0	74	13.95	0
BK-02	1	75	13.94	0
BK-03	2	75	13.94	0
BK-04	3	76	13.93	0
BK-05	4	76	13.93	0
BK-06	5	76	13.92	0
BK-07	8	75	13.92	0
BK-08	10	75	13.91	0
BK-09	12	75	13.91	0.220
BK-10	15	75	13.90	0.350
BK-11	17	75	13.90	0.409
BK-12	19	75	13.89	0.490
BK-13	22	75	13.89	0.650
BK-14	25	75	13.88	0.795
BK-15	35	75	13.87	0.825
BK-16	45	74	13.86	0.862
BK-17	60	74	13.83	0.916
BK-18	100	75	13.80	0.970

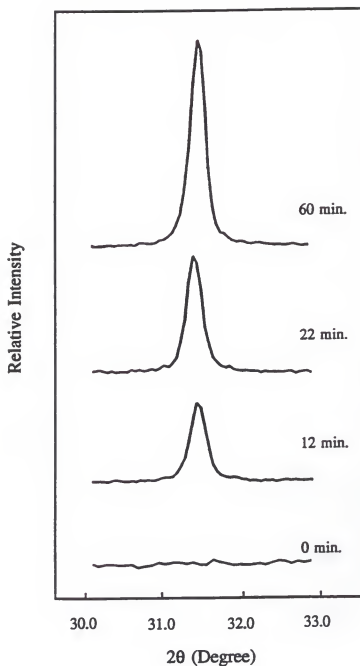


Figure 5-3. X-ray diffraction patterns of (110, 101) reflection showing a change in crystallinity as a function of reaction time during barium titanate formation process from the hydrous Ba-Ti complex gel at 75°C.

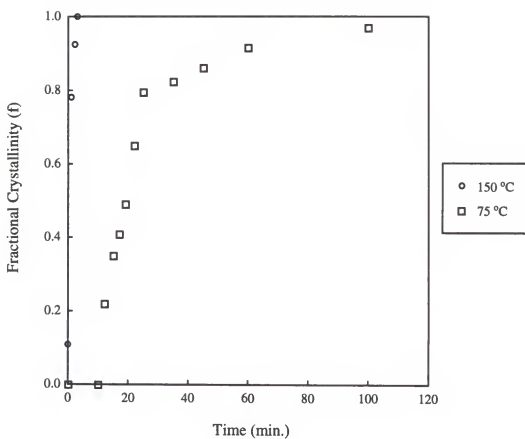


Figure 5-4. Crystallization curves for  $\text{BaTiO}_3$  produced from the hydrous Ba-Ti complex gel under hydrothermal conditions.

$\ln[-\ln(1-f)]$  against  $\ln(t)$  over  $f = 0.15 - 0.50$  yield approximately straight lines with slopes  $m$  having a value falling within a range characteristic of three distinct reaction mechanisms, as summarized in Table 5-2 [33, 165, 166]. When  $m = 0.54 - 0.62$ , diffusion is the rate-limiting step, while a zero-order, first-order, or phase boundary controlled mechanism is indicated for  $m = 1.0 - 1.24$ . A mechanism involving nucleation and growth control is implied when  $m = 2.0 - 3.0$ . Kinetic analysis was applied only to the kinetic data obtained at 75°C due to a lack of the early crystallization data for the high temperature reaction (i.e., initial fractional crystallinity  $> 0.7$ ). In the current analysis, linear regression in the complete data range was performed instead of applying only to the early stage of crystallization.

The result of kinetic analysis is presented in Figure 5-5. The crystallization kinetics are described by a two-stage kinetic rate law. The first stage is characterized by  $m = 2.30$  followed by a transition at approximately  $f = 0.6$  to a second stage which is identified by  $m = 0.70$ . Formation kinetics of the first stage indicate a nucleation and growth mechanism, which means that the product phase is growing from randomly distributed nuclei within the reactant phase, although the  $m$  value for the second region does not belong to any of the three mechanisms. The currently analyzed solid state nature of the transformation indicates the dissolution and recrystallization mechanism in the solution phase. However, this kinetic analysis was originally designed for isothermal solid-state transformation such as the dehydroxylation of brucite [166]. It is difficult to achieve literal mechanistic interpretation simply based on the  $m$  values. Despite these limitations, careful application of their simple solid-state kinetic treatments is often helpful in developing a qualitative understanding of the dominant processes in the early stage even in solution phase, particularly if corroborated against microstructural evidence [33].

Therefore, microstructural evolution during the crystallization process at 75°C was investigated using TEM. Figure 5-6 presents TEM micrographs showing the barium titanate formation process as a function of reaction time. Crystalline  $\text{BaTiO}_3$  particles of

Table 5-2. Solid-State Reaction Rates Equations [33]

Function	Implied mechanism	Equation	m
$D_1(f)$	Diffusion controlled	$f^2 = kt$	0.62
$D_2(f)$	Diffusion controlled	$(1-f)\ln(1-f) + f = kt$	0.57
$D_3(f)$	Diffusion controlled	$[1-(1-f)^{1/3}]^2 = kt$	0.54
$D_4(f)$	Diffusion controlled	$1-2f/3-(1-f)^{2/3} = kt$	0.57
$F_1(f)$	First order	$-\ln(1-f) = kt$	1.00
$R_2(f)$	Phase boundary	$1-(1-f)^{1/2} = kt$	1.11
$R_3(f)$	Phase boundary	$1-(1-f)^{1/3} = kt$	1.07
$Z_1(f)$	Zero order	$f = kt$	1.24
$A_2(f)$	Nucleation and growth	$[-\ln(1-f)]^{1/2} = kt$	2.00
$A_3(f)$	Nucleation and growth	$[-\ln(1-f)]^{1/3} = kt$	3.00

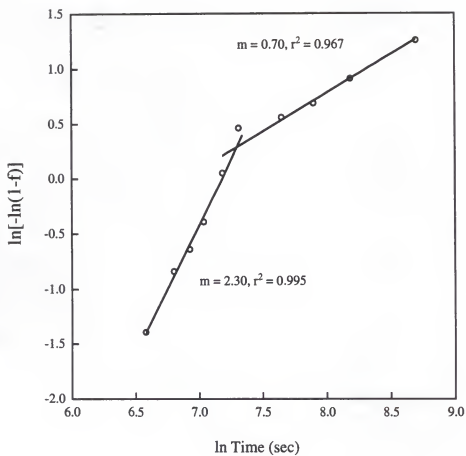


Figure 5-5. Johnson-Mehl-Avrami plot for the kinetic data of  $\text{BaTiO}_3$  formation from the hydrous Ba-Ti complex gel at  $75^\circ\text{C}$  ( $m$  is the exponent constant and  $r^2$  is the correlation coefficient).

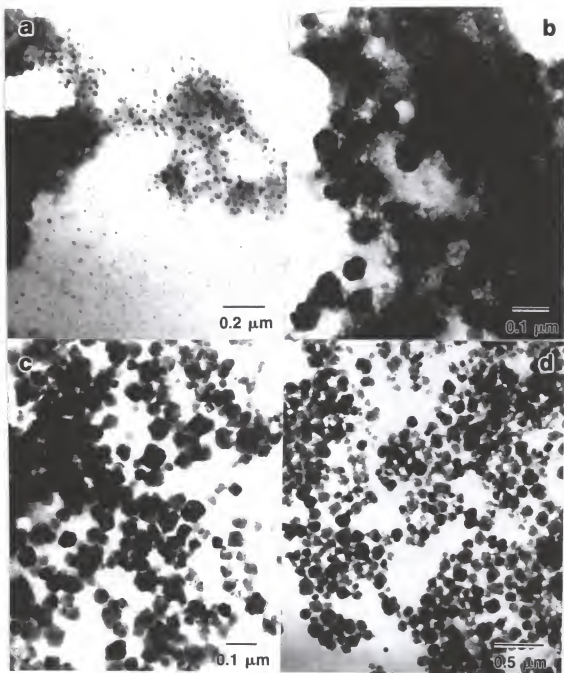


Figure 5-6. TEM micrographs showing formation process of BaTiO<sub>3</sub> from the hydrous Ba-Ti complex gel at 75°C as a function of reaction time: (a) 5 min (BK-06); (b) 15 min (BK-10); (c) 25 min (BK-14); and (d) 60 min (BK-17), respectively.

approximately 50 nm size were observed after 5 minutes although crystallinity in this sample could not be detected by XRD analysis. These particles then grew to 80 nm during the 60 minute reaction time. Interestingly enough, some particles at the intermediate stage exhibited a faceted cube-like shape. The cubic morphology probably reflects the crystallographic nature of the cubic perovskite.

Since the nucleation process occurred earlier than 5 minutes, HRTEM was used to investigate the nucleation process and morphological features of nuclei for the samples collected before reaction temperature was stabilized in the very early stage of the process. For the sample extracted at the instantaneous temperature of 42°C, 5 min after the precursor solution was added into the reactor, spherical nuclei with approximately 4 nm size were observed in the sample as given in Figure 5-7(a). It was difficult to obtain the focused image of a single nuclei with a strong electron beam of 400 KV due to interactions between the nuclei and electron beam. Even with an electron beam voltage of 200 KV, the diffraction pattern was different from that taken from the same area after 4 minutes of electron beam exposure, as shown in Figure 5-8. The origin of the interaction is probably related to destruction or displacement of the nuclei by a strong focused electron beam since the nuclei involve such a small volume. Despite this problem, several nuclei clearly show a lattice structure. Selected area diffraction analysis of BaTiO<sub>3</sub> nuclei reveals their single-crystal nature, as shown in Figure 5-7(b). The crystal structure of the nuclei seems to be cubic perovskite although the tetragonal structure is the thermodynamically stable phase.

There are two models proposed to describe the room temperature stabilization of the cubic phase [161]. One is a phenomenological surface layer model in which a tetragonal core and outer cubic surface layer coexist. The other is a strain effect model in which lattice hydroxyl and particle size play an important role. Since it is unlikely to form an interface of crystal structural transition within such a small nuclei, the latter mechanism is considered to be appropriate. Furthermore, it is observed that lattice fringes pass across the entire crystallite without interruption, indicating that the nuclei are free from any point or line

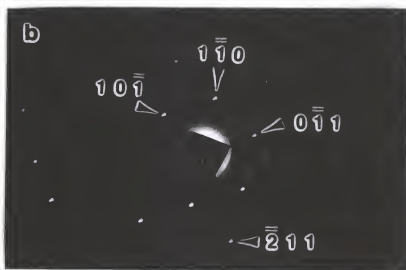
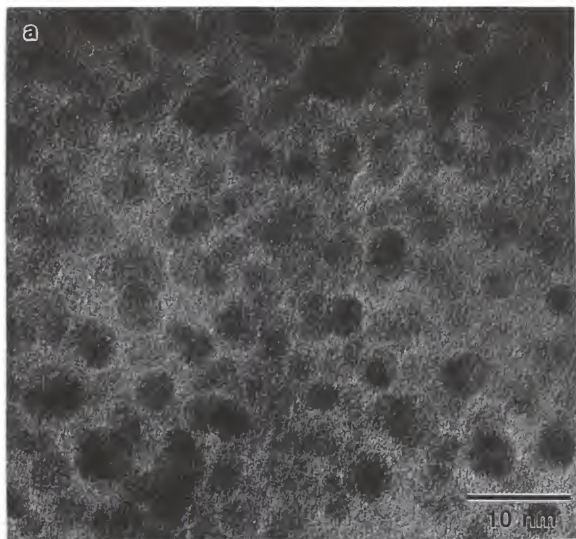


Figure 5-7. HRTEM micrograph of the sample extracted at the instantaneous temperature of 42°C, 5 min after the precursor solution was added into the reactor. A selected area diffraction pattern ( $B=[111]$ ) is also shown.

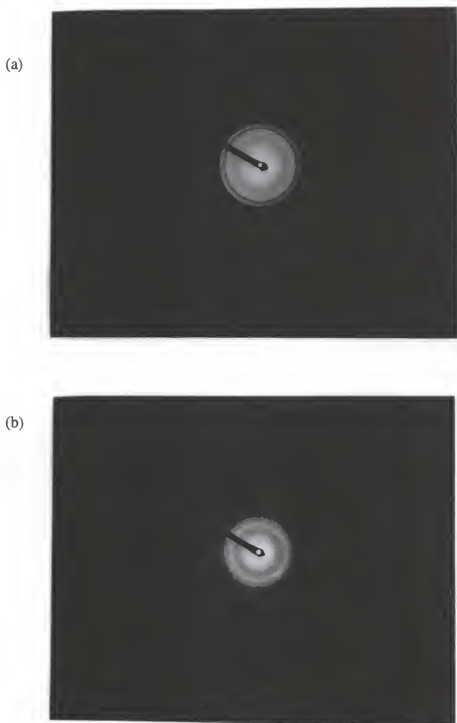


Figure 5-8. Diffraction patterns taken from the same area of the sample collected at 42°C, 5 min as a function of beam exposure time, indicating interaction between the sample and electron beam: (a) as-focused; and (b) after 4 minute exposure.

defect and are neither partially nor poorly crystallized, as would be expected in the product from homogeneous precipitation. The HRTEM micrograph of Figure 5-9 presents microstructural features of the sample (BK-06), which was grown further at 75°C for 5 min. Microstructural information revealed by the lattice structure implies that the particles have a very clear boundary and still maintain a defect-free structure. Unlike the initial nuclei observed in sample BK-01, the particle morphology is cubic. For the fully grown barium titanate particles, as shown in Figure 4-7 of Chapter 4, however, the dominant morphology is spherical. Consequently, it is believed that morphological changes occur during the growth process. The originally spherical particles transform to a cubic morphology and later revert to the spherical habit. Spherical  $\text{BaTiO}_3$  nuclei form to minimize the surface area in the nucleation process. As such nuclei grow, crystallographic habit growth plays a role in particle morphology and the spherical nuclei change into the cubic particles. In the perovskite structure, the  $\{100\}$  has the lowest surface energy and in turn the slowest plane growth rate [167]. Thus, the equilibrium shape is cubic, as observed in the other perovskite  $\text{PbTiO}_3$  and PZT [76, 84]. However, the high energy faceted edges of the cubic particles may be subject to preferential dissolution and, in addition, the strain associated with cubic structure stabilization tends to reduce the surface area of the growing particles. As a result, cubic-shaped particles are exhibited an intermediate morphology which generally returns to the spherical shape during the final stage, although some larger particles still retain their cube-like shape. Particle surface roughness observed in Figure 4-7 is probably due to this competing effect.

The microstructural evidence along with kinetic analysis using the Johnson-Mehl-Avrami equation strongly supports that the formation mechanism of  $\text{BaTiO}_3$  in the current material system is due to dissolution and recrystallization. If transformation is achieved by inward diffusion into the undissolved amorphous Ti gel structure, the boundary between unreacted Ti gel core and  $\text{BaTiO}_3$  outside layer should be observed at the early stage of nucleation by HRTEM. To describe relevant reaction for the proposed formation

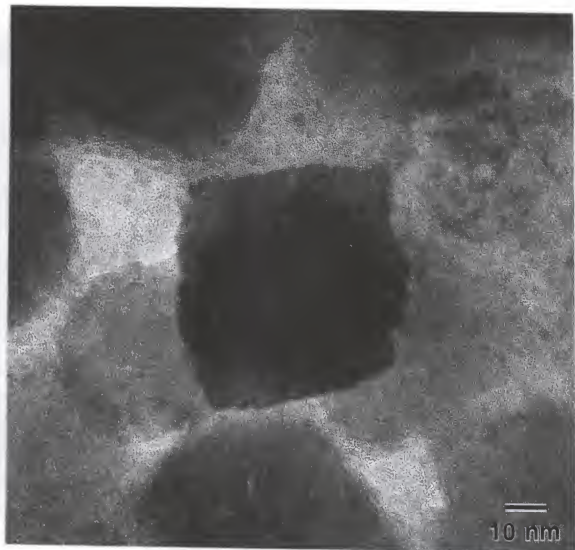
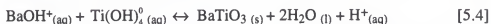


Figure 5-9. HRTEM micrograph of the sample BK-06.

mechanism,  $\text{BaOH}^+$  and  $\text{Ti}(\text{OH})_4^0$  are selected to the appropriate solution reacting species involved in the current highly alkaline condition, based on the aqueous chemistry of metal cations in Chapter 3.  $\text{BaTiO}_3$  precipitates from solution via the following reactions:



The pH is a critical reaction parameter in synthesizing a phase-pure  $\text{BaTiO}_3$  under hydrothermal conditions as shown in Chapter 4. An adequate  $\text{OH}^-$  concentration is required to form hydrolyzed aqueous species and subsequently enhance precipitation of the crystalline product from the Ba-Ti amorphous complex gels. According to the above reactions,  $\text{H}^+$  releases as barium titanate forms, resulting in a lowering of the pH. As shown in Figure 5-10, as a consequence, the pH of the reaction medium continuously lowers and reaches constant, upon reaction completion.

Precipitation from solution proceeds through 1) formation of solute species, 2) nucleation from supersaturated solution, 3) particle growth via either solute addition reaction or aggregation [111]. In the current system, the formation process of solute species is dissolution of the hydrous Ba-Ti gel as indicated by equation [5.3]. Once the solution is supersaturated due to dissolution of the precursor, precipitation of  $\text{BaTiO}_3$  from homogeneous solution occurs, resulting in a burst of the nuclei. In Figure 5-11, the proposed dissolution-recrystallization mechanism for  $\text{BaTiO}_3$  particle formation is schematically depicted. Since dissolution of the hydrous titania would be more difficult, it will be a rate limiting step in the early stage of nucleation and growth. After nucleation, the nuclei grow rapidly, representing an initially fast kinetic rate in the crystallization curve. Then, the nucleation event lowers the solute concentration below the critical supersaturation but high enough for the particles to grow without secondary nucleation. If the particles grow by aggregation, the particles should contain defect structures such as stacking faults or grain boundaries [25]. However, HRTEM analysis does not show any evidence for the presence of the aggregated particles. Thus, particles are believed to grow by addition of

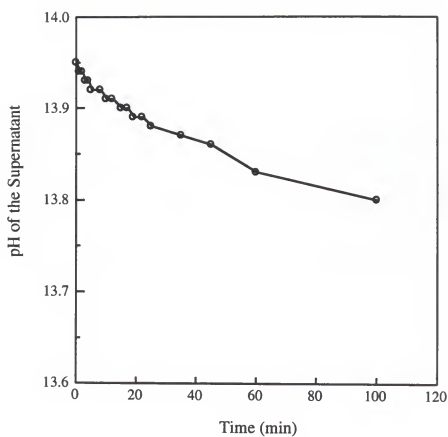


Figure 5-10. The pH variation behavior of the supernatant as a function of reaction time.

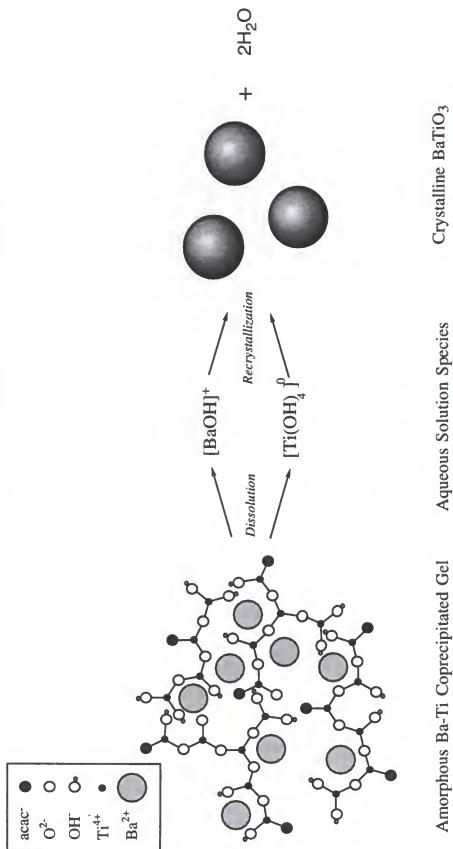


Figure 5-11. Schematic picture illustrating a proposed particle formation mechanism of  $\text{BaTiO}_3$  in the modified Ti alkoxide and barium acetate system.

solute. This reaction is controlled by either diffusion or surface incorporation reaction. In the current system, growth rate is more likely controlled by surface reactions due to the high diffusion coefficient of the solute in solution phase under hydrothermal conditions. Although  $[\text{Ti}(\text{OH})_4^0]$  is assumed as a soluble species for Ti, different soluble species of Ti such as  $\text{Ti}(\text{OH})_{4-x}(\text{acac})_x$  in which the acetylacetonate group is strongly bound to Ti may exist as indicated by the results of TGA/DTA in Figure 4-4(b). If such solute species are involved in surface reaction with  $\text{Ba}^{2+}$ , the acetylacetonate group must be released during dehydration process prior to the incorporation step at the surface of growing particle. Therefore, the dissociation of this terminal group would be rate-limiting in the later stage of growth, which implies a slow kinetic rate in the final stage as shown in Figure 5-4.

### Conclusions

Formation mechanisms of  $\text{BaTiO}_3$  under hydrothermal conditions were investigated. The use of the coprecipitated precursor prepared from the modified titanium alkoxide and barium acetate made it possible to monitor crystallization behavior at  $75^\circ\text{C}$ . Spherical 4 nm size nuclei were observed using high resolution TEM. The lattice image of the 4 nm nuclei implies that crystallites exhibit a defect free structure and are not partially or poorly crystallized. The morphology of the nuclei changes into cubic particles at the intermediate stage as they grow and then mostly return to spherical shape when they are fully reacted. A solid-state kinetic analysis along with supportive microstructural evidence indicates that the formation mechanism of  $\text{BaTiO}_3$  in the current material system is a dissolution and recrystallization. The Ba-Ti complex gel dissolves into the aqueous soluble species, followed by direct precipitation from supersaturated solution occurs between these species. It is proposed that crystallization is controlled by dissolution of the hydrous Ti gel at the initial stage and then possibly by dissociation of the acetylacetonate group from the Ti solution species in which the acetylacetonate group is strongly bound to Ti.

## CHAPTER 6

### INFLUENCES OF TITANIUM PRECURSOR CHARACTERISTICS ON PARTICLE FORMATION MECHANISMS OF BaTiO<sub>3</sub>

#### Introduction

In the hydrothermal particle synthesis of BaTiO<sub>3</sub>, the dynamic nature of the interaction between TiO<sub>2</sub>, Ba<sup>2+</sup>, and OH<sup>-</sup> in solution phase determines crystallization mechanisms. The uncertain reaction characteristics of Ti precursors makes it difficult to understand particle formation mechanisms. Depending upon whether the Ti precursors dissolve or not during hydrothermal reactions, different reaction pathways can be proposed. The Ti precursor itself may undergo phase transformation or crystallization prior to BaTiO<sub>3</sub> formation. In addition, the type of Ti precursors significantly influences reaction kinetics. Generally, the reactivity of the Ti precursors with respect to the formation of BaTiO<sub>3</sub> is recognized to follow the hierarchy: amorphous Ti gel > anatase TiO<sub>2</sub> > rutile TiO<sub>2</sub> [144]. These reactivity differences in the Ti precursors subsequently lead to the production of BaTiO<sub>3</sub> particles with different particle size and morphology via distinct formation mechanisms.

In the last chapter, dissolution-recrystallization mechanism was proposed for BaTiO<sub>3</sub> formation from the modified Ti alkoxide and barium acetate based on microstructural evidence and kinetic analysis. In the current chapter, a similar approach is taken to study the effect of the Ti precursor type on BaTiO<sub>3</sub> formation mechanisms. The reaction kinetics of both BaTiO<sub>3</sub> derived from the amorphous Ti gel and BaTiO<sub>3</sub> derived from the hydrothermally treated Ti precursor in barium hydroxide solution are compared at 75°C. Kinetic studies at this lower temperature allows direct observation of microstructural

evolution, including the nucleation process, and leads to a better understanding of formation mechanisms under hydrothermal conditions.

### Materials and Methods

Aqueous suspension of the titanium gels<sup>1</sup> were prepared by neutralization of  $\text{TiCl}_4$  with  $\text{NH}_4\text{OH}$  at pH 6-8 at Cabot Performance Materials. Upon receipt in our laboratory, the gels were separated into aliquots and stored in the frozen state to prevent aging. Preliminary experiments indicated that the titanium gels produce inconsistent results as a function of aging time. Phase and morphology of the as-received Ti gel were examined by X-ray diffractometry and by transmission electron microscopy, respectively. Determination of solids loading in the Ti gel slurry entailed the use of thermal gravimetric analysis and differential thermal analysis. Samples of 0.2 ml were taken from the Ti gel slurry while under rigorous agitation. The sample for TGA/DTA was heated at a rate of  $5^\circ\text{C}/\text{min}$  from  $25^\circ\text{C}$  to  $90^\circ\text{C}$  and held for 1 hour to slowly evaporate water, followed by faster heating ( $10^\circ\text{C}/\text{min}$ ) up to  $800^\circ\text{C}$ .

Three different heat-treated titanium precursors were prepared from the as-received Ti gel. The heat treatments included drying, calcination and hydrothermal crystallization. A portion of the as-received wet Ti gel was dried at  $130^\circ\text{C}$  for 24 hours in an oven and another portion calcined at  $600^\circ\text{C}$  for 1 hour in a furnace, respectively.  $\text{CO}_2$ -free deionized water was used to prepare the hydrothermally treated Ti precursor. The pH of the suspension was 7.2. Hydrothermal treatment was performed at  $150^\circ\text{C}$  for 30 min using a 600 ml-capacity autoclave with a magnetically driven stirrer. The phase composition and morphology of each heat-treated Ti precursor were examined using XRD and TEM.

To perform the crystallization kinetics study at the conditions in which the phase-pure  $\text{BaTiO}_3$  can form without carbonate contamination, hydrothermal synthesis conditions using the as-received wet Ti gel and barium octa-hydroxide<sup>2</sup> were determined. The

<sup>1</sup>Lot# 6814-320, Cabot Performance Materials, Boyertown, PA.

<sup>2</sup>97%, Solvay Performance Chemicals, Greenwich, CT.

molarity of the Ti in the as-received slurry was calculated based on the result of TGA assuming the remaining solid product after calcination at 800°C was  $\text{TiO}_2$ . The appropriate amount of Ti gel was added to the  $\text{CO}_2$ -free aqueous suspension containing  $\text{Ba}(\text{OH})_2$  at 25°C. To homogenize the precursor suspension and increase the solubility of the barium hydroxide, the suspension was mechanically agitated by an ultrasonic probe<sup>3</sup> for 5 min under an argon atmosphere. The molar ratio of Ba:Ti was 1.1:1. Excess barium was introduced to easily drive reaction to complete and also to compensate for possible loss of Ba species due to incongruent dissolution in the washing procedure. In the first set of experiments, the feedstock concentration was varied from 0.1 to 0.2 M to examine the effects of solids loading and the precursor suspension pH on the isothermal formation of  $\text{BaTiO}_3$  at 90°C. In the second set, the reaction temperature was varied from 60 to 80°C at the feedstock concentration of 0.2 M to determine the lowest possible synthesis temperature. For the hydrothermal treatment, a Teflon lined acid digestion bomb was used. After reactions, the phase composition of the recovered products were determined by XRD.

Once the synthesis conditions were determined, crystallization behavior was investigated to study the influences of the Ti precursor characteristics on the formation mechanisms. Reaction kinetics of  $\text{BaTiO}_3$  formation under isothermal conditions in  $\text{Ba}(\text{OH})_2$  solution involving either the as-received Ti gel or as-hydrothermally-treated Ti gel were compared. The latter precursor was used as-hydrothermally-treated state without further processes such as drying or washing. The molar ratio of Ba:Ti was 1.1:1 and the feedstock concentration was 0.2 M. The same reaction vessel was utilized as shown in Figure 5-2. Reactions were performed at 75°C by pouring the precursor suspensions into the hot reactor under Ar atmosphere. It took 20 minutes to reach a stable temperature, thus the time at this moment was recorded as a zero reaction time during the kinetic analysis. Reaction products collected at various reaction times were recovered according to the same procedures as described in Chapter 5. Then, quantitative evaluation of reaction progress

---

<sup>3</sup>Model 60, Fisher Scientific, Pittsburgh, PA.

and observation of microstructural evolution were performed by XRD and HRTEM, respectively.

## Results and Discussion

### Ti Precursor Characteristics

The phase of the as-received wet Ti gel was amorphous, whereas its dried state at 130°C consisted of a mixture of an amorphous phase with anatase, as shown in Figure 6-1. When calcined at 600°C, the phase of the Ti precursor was rutile. In contrast, the hydrothermal reaction product of the amorphous Ti gel was anatase. Morphologies of the as-received wet and hydrothermally treated Ti precursors, including a selected area diffraction pattern (SADP), are presented in Figure 6-2. The as-received wet Ti precursor has a very fine gel structure while the hydrothermally synthesized anatase has a granulous shape with an average particle size of 10 nm.

Crystalline titanium dioxide has three different crystal structures, rutile, anatase, and brookite, depending upon the connection modes of the  $[\text{TiO}_6]$  octahedra building block. In rutile 2, in anatase 3, and in brookite, 4 edges of the 12 edges of the octahedra are shared [168]. Since the stability of the structure decreases as the number of the shared edges or faces increases, rutile is the most stable and brookite the least stable of the three polymorphisms. Recently, Cheng et al. demonstrated that the phase and even morphology of  $\text{TiO}_2$  can be controlled by hydrothermal reaction conditions [169]. The granular anatase  $\text{TiO}_2$  formed at a reaction medium pH ranging from 1 to 8, whereas the acicular rutile became stable only at highly acidic conditions ( $\text{pH} < 0$ ). At a highly alkaline condition ( $\text{pH} > 13$ ), however, the hydrothermal reaction product was amorphous.

Dissolution-recrystallization has been proposed for the formation mechanism of  $\text{TiO}_2$  under hydrothermal conditions [170]. In such a case, the chemical nature of the aqueous solution species at a given system condition plays an important role in

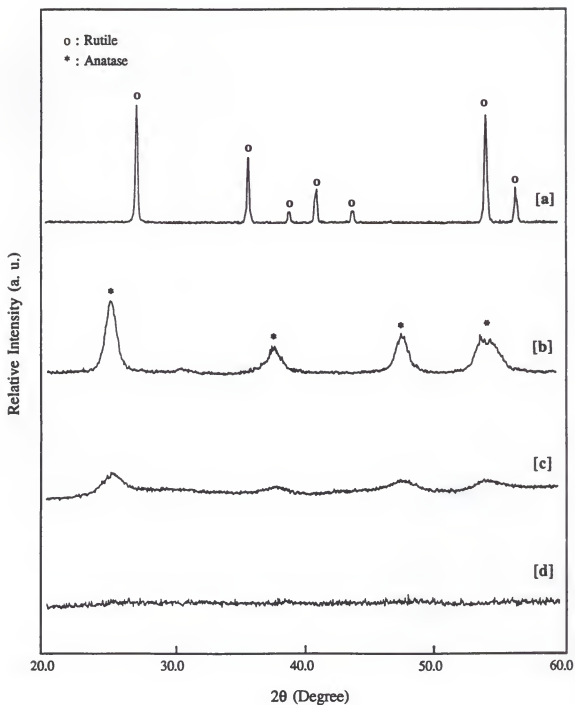


Figure 6-1. X-ray diffraction patterns of the various titanium precursors: (a) calcined at 600°C for 1 hour; (b) hydrothermally treated at 150°C for 30 min; (c) dried at 130°C for 24 hours; and (d) the as-received wet Ti gel.

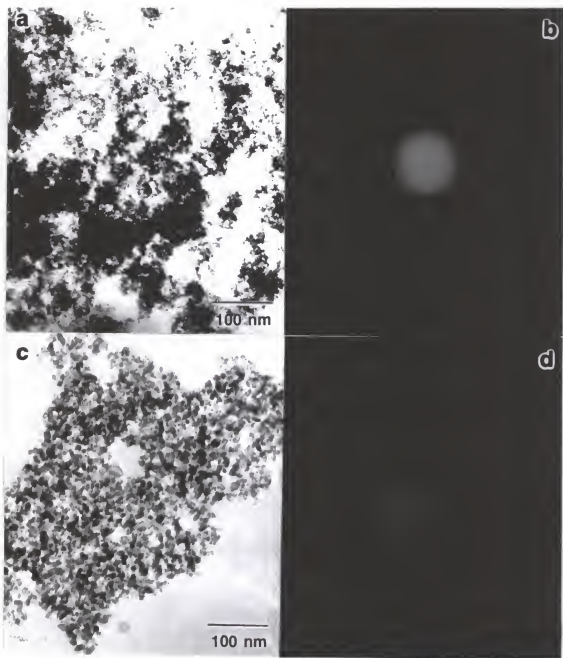


Figure 6-2. TEM micrographs showing morphology of the titanium precursors: (a) and (b) the as-received wet Ti gel and its selected area diffraction pattern; (c) and (d) the hydrothermally treated Ti precursor at 150°C for 30 min and its selected area diffraction pattern.

determining the phase of the precipitate. At  $\text{pH} > 2$ , the dominant aqueous species for Ti is believed to be  $[\text{Ti}(\text{OH})_4]^0$ . In the crystallization of  $\text{TiO}_2$ , a Ti-O-Ti linkage forms via a dehydration reaction (i.e., oxolation) from  $[\text{Ti}(\text{OH})_4]^0$ . Every hydroxyl ( $\text{OH}^-$ ) group in  $[\text{Ti}(\text{OH})_4]^0$  is a reaction active site, so that the possibility of edge sharing between  $[\text{TiO}_6]$  octahedra building blocks increases and subsequently the formation of anatase is preferred. As the pH decreases below 2, the dominant aqueous species of Ti changes into  $[\text{Ti}(\text{OH})_2]^{2+}$ . As a result, the probability of edge sharing decreases, and in turn the rutile becomes stable with the decreasing number of the available hydroxyl groups in the aqueous species of Ti [169].

Similarly, the current hydrothermal treatment of the amorphous Ti gel at pH 7 resulted in the formation of nanosize anatase. However, solid-state heat-treatment of the hydrous Ti gel provided different phases depending upon the calcination temperature. At lower drying temperatures of the amorphous Ti gel, the metastable anatase forms, whereas high temperature calcination transforms the Ti gel into thermodynamically stable rutile. Results of TGA/DTA confirm this phase transformation behavior, as shown in Figure 6-3. The total weight loss was 90.9%, which was mainly associated with the evaporation of water as indicated by the endothermic peak below  $100^\circ\text{C}$ . The latter exothermic peaks at temperatures between  $120^\circ\text{C}$  and  $400^\circ\text{C}$  can be assigned to phase transformation from the amorphous to the metastable anatase and eventually to the stable rutile, respectively.

#### Reaction Conditions for Barium Titanate Particle Synthesis

The solution pH is one of the most critical reaction parameters controlling phase composition and even morphology of the particles, since solution pH mainly determines the chemical nature of the aqueous solution species [137, 138, 140]. In this regard, the pH condition for phase-pure barium titanate formation under hydrothermal conditions was investigated. Since the pH of the reaction medium depends on the concentration of barium hydroxide in the present study, the pH was varied from 12.4 to 13.1 by increasing total

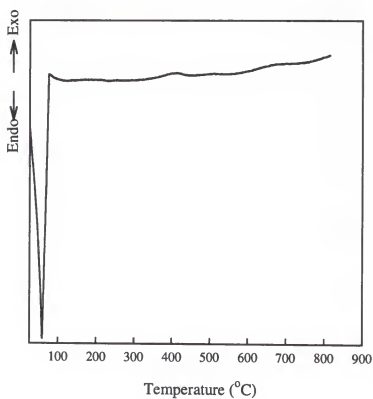
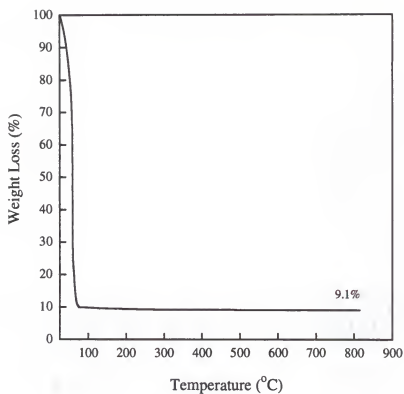


Figure 6-3. TGA/DTA curves for the as-received wet Ti gel. The sample was heated to 800°C at a rate of 10°C/min in air.

feedstock concentration from 0.1 M to 0.2 M, respectively. Reactions were performed at 90°C for 6 hours under an argon atmosphere. It was determined from X-ray analysis that the production of phase-pure BaTiO<sub>3</sub> requires a highly alkaline condition (pH>13) as shown in Figure 6-4(a). Below pH 13, the products were amorphous except for a minor barium carbonate phase, whereas cubic BaTiO<sub>3</sub> forms when the pH >13. This observation was consistent with both the theoretical predictions observed in the stability diagram (Figure 3-3) and the previous findings in Chapter 4.

For the observation of nucleation and growth processes at temperatures as low as possible in the kinetic study, the lowest synthesis temperature for BaTiO<sub>3</sub> formation was also determined. The feedstock suspensions with a constant concentration of 0.2 M were placed in an oven at temperatures of 60°C, 70°C, and 80°C for 12 hours using 23 ml acid digestion bombs. As shown in Figure 6-4(b), the phase of the sample treated at 60°C was unreacted amorphous Ti gel including a contaminant phase of BaCO<sub>3</sub>. However, barium titanate started to form at 70°C, although complete crystallization was not achieved within 12 hours, whereas well-crystallized phase-pure BaTiO<sub>3</sub> was obtained at 80°C. Therefore, it was determined that the most appropriate reaction conditions for the study of particle formation mechanisms entail the use of a 0.2 M of feedstock concentration at reaction temperatures above 70°C.

#### Influence of Ti Precursor Characteristics on Barium Titanate Particle Formation

Detailed reaction conditions for each extracted sample including reaction time, temperature and fractional crystallinity are summarized in Tables 6-1 and 6-2. The crystallization behavior of BaTiO<sub>3</sub> at 75°C involving the as-received Ti and hydrothermally-treated Ti precursors is shown in Figure 6-5. When the amorphous Ti precursor was involved, increased reaction kinetics without an induction period was observed, as compared to the hydrothermally treated Ti precursor. However, no complete transformation was achieved in either case within the investigated reaction time. The

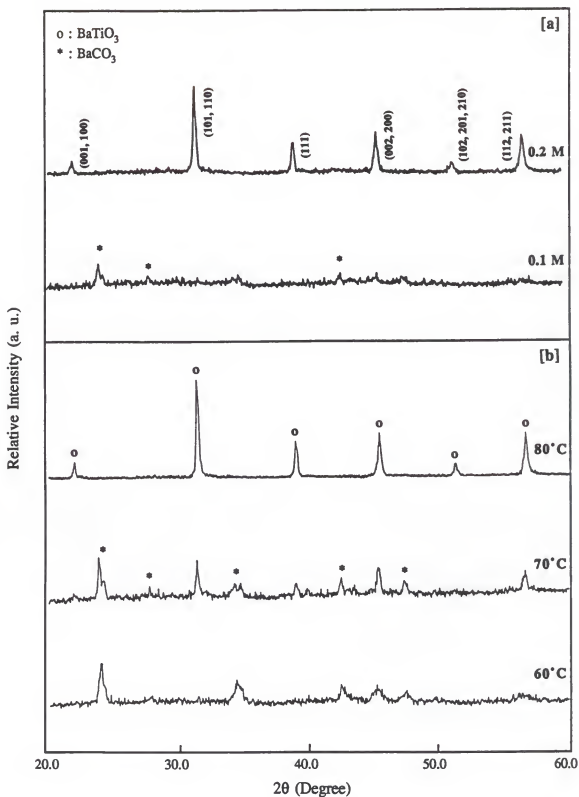


Figure. 6-4. XRD patterns of the hydrothermally synthesized products: (a) as a function of the total feedstock concentration at  $95^\circ\text{C}$ ; and (b) as a function of the reaction temperature at the feedstock concentration of 0.2 M.

Table 6-1. Kinetic Data for the  $\text{BaTiO}_3$  Formation Process from the As-Received Ti Gel Precursor and Barium Hydroxide

Sample ID	Reaction time (min)	Temperature ( $^{\circ}\text{C}$ )	Fractional crystallinity
BA-01	3	38	0
BA-02	9	52	0
BA-03	15	63	0
BA-04	20	68	0.024
BA-05	25	73	0.062
BA-06	30	74	0.145
BA-07	40	75	0.250
BA-08	50	75	0.370
BA-09	60	75	0.480
BA-10	80	74	0.571
BA-11	100	75	0.652

Table 6-2. Kinetic Data for the  $\text{BaTiO}_3$  Formation Process from the Hydrothermally-Treated Ti Precursor and Barium Hydroxide

Sample ID	Reaction time (min)	Temperature ( $^{\circ}\text{C}$ )	Fractional crystallinity
BC-01	1	36	0
BC-02	2	39	0
BC-03	5	50	0
BC-04	10	63	0.024
BC-05	20	69	0.062
BC-06	29	70	0.145
BC-07	35	72	0.250
BC-08	43	73	0.370
BC-09	50	75	0.480
BC-10	60	75	0.571
BC-10	60	75	0.571
BC-11	80	74	0.652

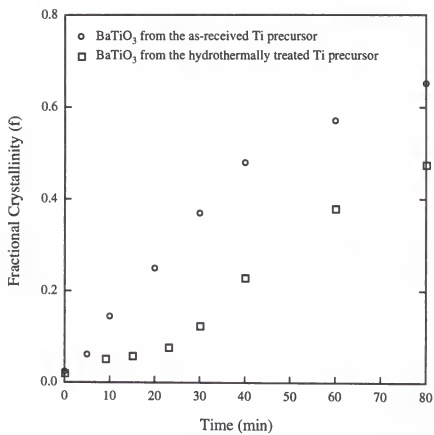


Figure 6-5. Crystallization curves for BaTiO<sub>3</sub> at 75°C prepared by reacting the different Ti precursors in barium hydroxide aqueous solution.

maximum crystallinity for  $\text{BaTiO}_3$  formation from the as-received Ti gel and hydrothermally treated Ti precursors was 0.652 and 0.475, respectively.

In order to gain further insight into the formation mechanism of crystalline  $\text{BaTiO}_3$ , the obtained kinetic data were evaluated using the same Johnson-Mehl-Avrami analysis method as described in Chapter 5. The results of the kinetic analysis are presented in Figure 6-6. The reaction kinetics of  $\text{BaTiO}_3$  from the amorphous Ti gel shows a single-stage rate law. Linear regression yields  $m$  value of 1.09 with very high correlation coefficients. These results imply a phase-boundary controlled mechanism in which the initial crystallization is controlled by interfacial chemical reaction. On the other hand, the crystallization kinetics for  $\text{BaTiO}_3$  formation from the hydrothermally treated Ti precursor is described by a two-stage rate control. The first stage is characterized by  $m = 0.4$  followed by a sharp transition at approximately  $f = 0.059$  to a second stage, which is identified by  $m = 1.69$ . The formation kinetics of both stages do not directly correlate to any mechanisms of standard solid-state reaction rate equations. However, abrupt transition from slow to rapid reaction kinetics may indicate that a precipitation-like mechanism prevails in the early stage of the reaction.

Microstructural evolution during the crystallization process was investigated using TEM. Figure 6-7 presents TEM micrographs showing the barium titanate formation process from the as-received Ti gel as a function of reaction time. It was observed that the spherical 25 nm  $\text{BaTiO}_3$  crystallites evolve from the amorphous Ti gel. However, no significant particle growth occurs so that the 50 nm particle size remains almost constant after 35 min. The relevant SADP also confirms barium titanate formation by showing the (110)  $\text{BaTiO}_3$  reflection spots on the amorphous ring structure. In the case of  $\text{BaTiO}_3$  formation from the hydrothermally treated Ti precursor, on the other hand, it was observed that the 50 nm size  $\text{BaTiO}_3$  crystallites with rough surfaces form at the initial stage on the nanosize anatase aggregates. Then, further growth into 200 nm size particles proceeds by consuming the neighboring anatase after 60 min as shown in Figure 6-8. Consequently,

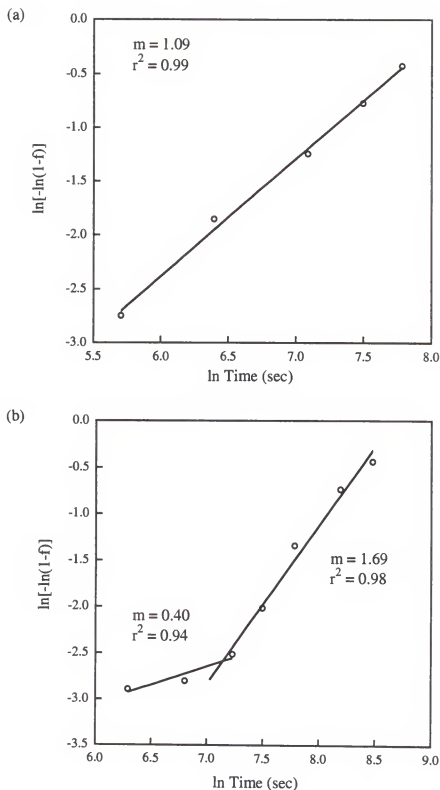


Figure 6-6. Johnson-Mehl-Avrami plot for the kinetic data of  $\text{BaTiO}_3$  formation using the (a) as-received amorphous Ti gel and (b) hydrothermally treated Ti precursor. The  $m$  is exponent constant and  $r^2$  is correlation coefficient.

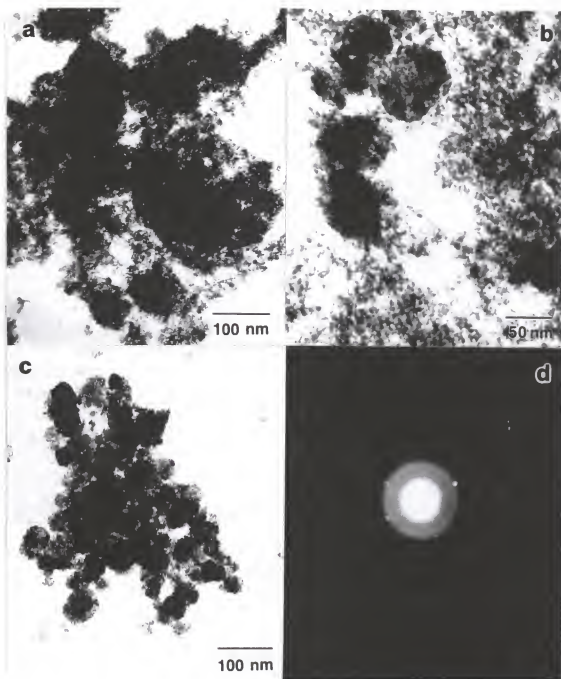


Figure 6-7. TEM micrographs showing formation process of  $\text{BaTiO}_3$  from the as-received Ti gel and barium hydroxide as a function of reaction time: (a) 3 min (BA-01); (b) 9 min (BA-02); (c) 35 min (BA-06); and (d) SADP for BA-02, respectively.

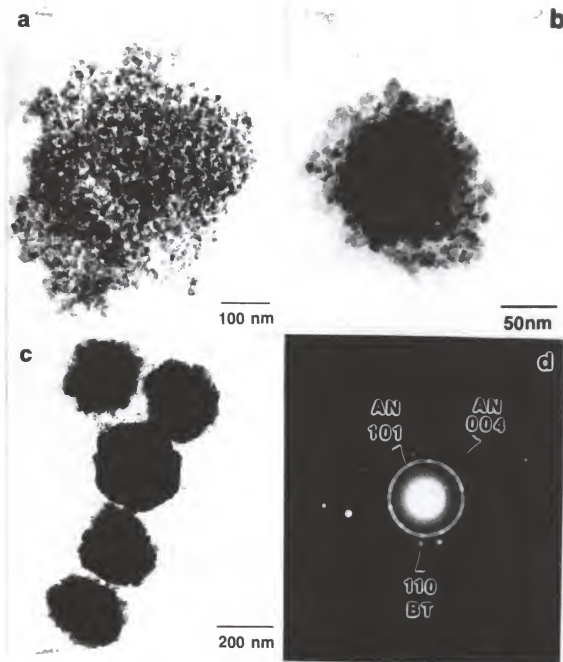


Figure 6-8. TEM micrographs showing formation process of BaTiO<sub>3</sub> from the hydrothermally treated Ti precursor and barium hydroxide as a function of reaction time: (a) 5 min (BC-03); (b) 25 min (BC-06); (c) 60 min (BC-11); and (d) SADP for BC-03, respectively. The 'AN' and 'BT' represent reflection spots for the anatase and BaTiO<sub>3</sub>, respectively.

the (110)  $\text{BaTiO}_3$  reflections appear between the nanosize anatase ring patterns in the relevant SADP.

To obtain better microstructural evidence of the nucleation process, the samples extracted during the very early stage of the reaction were investigated by HRTEM. In the case of  $\text{BaTiO}_3$  formation from the amorphous Ti gel, relatively spherical 5 -10 nm size  $\text{BaTiO}_3$  nuclei embedded in the Ti gel matrix were monitored in the sample BA-01, as shown in Figure 6-9. A random network open structure of the amorphous Ti gel was also revealed. Since the particle size was very small, weak diffraction ring patterns for  $\text{BaTiO}_3$  appeared in the corresponding SADP. No boundary between the unreacted Ti gel core and the  $\text{BaTiO}_3$  outside layer existed, which possibly implies dissolution-recrystallization as the formation mechanism of  $\text{BaTiO}_3$ .

In conjunction with the results of the Johnson-Mehl-Avrami analysis, however, a phase boundary controlled mechanism is proposed. The rate controlling step is a chemical reaction on the surface of the Ti gel. The amorphous Ti gel has a loose network structure in which the pores are mostly filled by solvent and are extensively inter-connected, resulting in the very large surface area [171]. Diffusion through such porous network structure is extremely rapid as compared to the bulk diffusion. Therefore, it is reasonable to assume  $\text{Ba}^{2+}$  ions cover the entire surfaces of the Ti gel throughout reaction. The chemical reaction between  $\text{TiO}_2$  and  $\text{Ba}^{2+}$  at the interfaces gives rise to nucleation of  $\text{BaTiO}_3$  within the gel by breaking and rearranging Ti-O-Ti bonds in the highly cross linked Ti gel followed by incorporation of  $\text{Ba}^{2+}$  into the lattice. Inward diffusion of  $\text{Ba}^{2+}$  through the freshly formed  $\text{BaTiO}_3$  layer is not expected since nucleation occurs from homogeneously mixed  $\text{TiO}_2$  and  $\text{Ba}^{2+}$ . Once  $\text{BaTiO}_3$  nucleates, particles grow via aggregation with unstable smaller  $\text{BaTiO}_3$  primary clusters, resulting in a raspberry-like appearance of  $\text{BaTiO}_3$  particles [29]. Therefore, a defect structure, including grain boundary and stacking faults, is likely to be present. Figure 6-10 shows the microstructure inside a  $\text{BaTiO}_3$  single particle. The proposed formation mechanism is schematically illustrated in Figure 6-11.

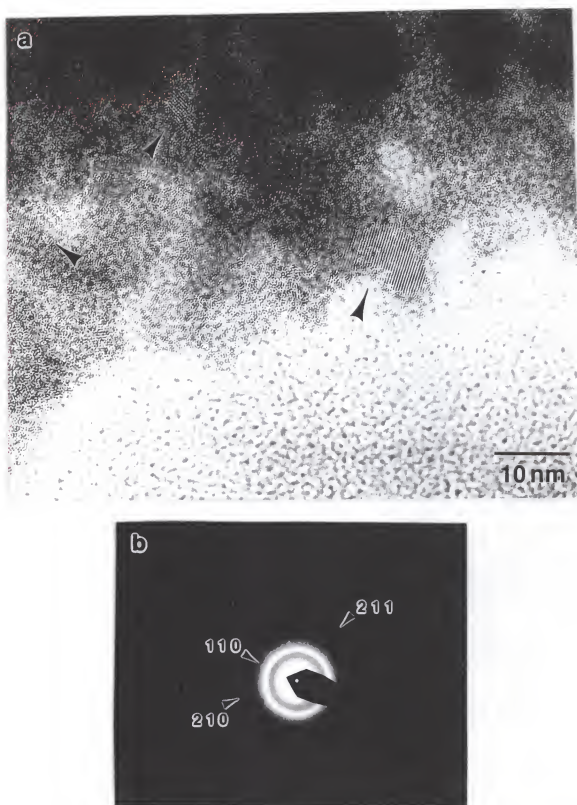
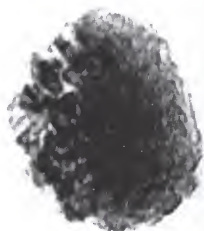


Figure 6-9. HRTEM micrograph of the sample BA-01 including selected area diffraction pattern.



 25 nm

Figure 6-10. TEM micrograph showing microstructure of the BaTiO<sub>3</sub> single particle (sample BA-05).

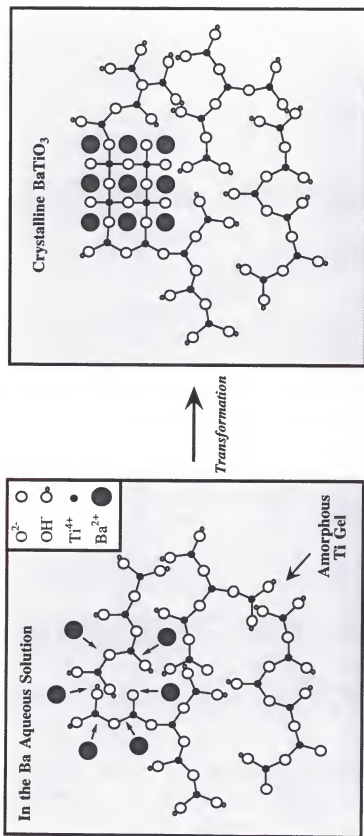


Figure 6-10. Schematic picture illustrating a proposed particle formation mechanism of BaTiO<sub>3</sub> in the amorphous Ti gel and barium hydroxide system.

For  $\text{BaTiO}_3$  nucleation from the hydrothermally treated Ti precursor, the nuclei could not be visually discerned from the aggregated crystalline  $\text{TiO}_2$  in the early reacted sample BC-02, although diffraction patterns suggest the presence of barium titanate. Instead, a further reacted sample BC-05, which manifests larger  $\text{BaTiO}_3$  crystallites, was examined. Bright and dark field images were used to distinguish between  $\text{BaTiO}_3$  and  $\text{TiO}_2$  by selecting  $g = \bar{1}10$ , as presented in Figure 6-12. However, complete exclusion of the  $\text{TiO}_2$  reflections could not be achieved since the  $\text{BaTiO}_3$  reflection spot was so close to the anatase ring pattern, thus a few bright-looking particles observed outside the particle aggregates are considered to be anatase in the dark field image (Figure 6-12(b)). The  $\text{BaTiO}_3$  particle surface was examined under a beam condition of  $B=[111]$ . A HRTEM micrograph showing an 80 nm  $\text{BaTiO}_3$  particle on the anatase aggregates was presented in Figure 6-13. The hexagonal lattice pattern of (111)  $\text{BaTiO}_3$  clearly reveals a phase boundary between the barium titanate and anatase. It was also observed that  $\text{TiO}_2$  lattice fringes run across the phase boundary without interruption. This implies that  $\text{BaTiO}_3$  grows at the expense of the anatase. Moire fringes inside the  $\text{BaTiO}_3$  particle resulted from misorientation of  $\text{BaTiO}_3$  crystallites by approximately  $10^\circ$ , as indicated in the SADP, showing split spots for  $0\bar{1}1$ .

Along with the X-ray kinetic analysis and microstructural evidence, the following formation mechanism for  $\text{BaTiO}_3$  from the hydrothermally treated Ti precursor is proposed. Nucleation of  $\text{BaTiO}_3$  starts heterogeneously on the smallest particle among the aggregated titania via dissolution-recrystallization. Although the solubility of the anatase at  $25^\circ\text{C}$  is approximately  $10^{-7}$  [mole/liter] as shown in Figure 3-1, which is too low to provide a sufficient level of supersaturation, this value does not consider local solubility given by surface energy effect of small particles [31]. The slow initial kinetics, as observed in Figure 6-5, probably represent an incubation-like period for dissolution. Once the desired supersaturation level is locally achieved,  $\text{BaTiO}_3$  nucleates on the anatase via a reaction between  $[\text{Ti}(\text{OH})_4^0]$  and  $[\text{BaOH}^+]$ , and grows by solute addition reaction,

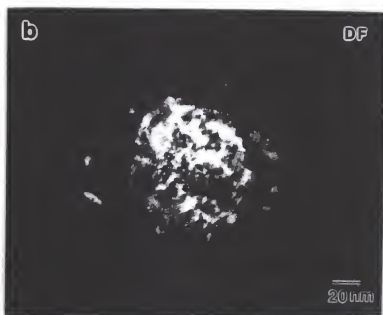
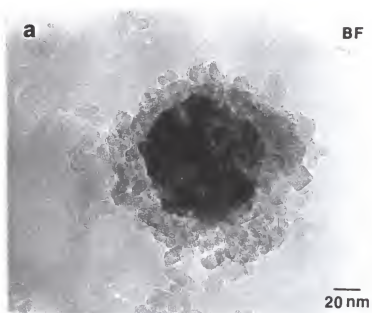


Figure 6-12. TEM micrographs showing microstructure of  $\text{BaTiO}_3$  particles (BC-05) embedded in aggregated anatase: (a) bright field image and (b) dark field image.

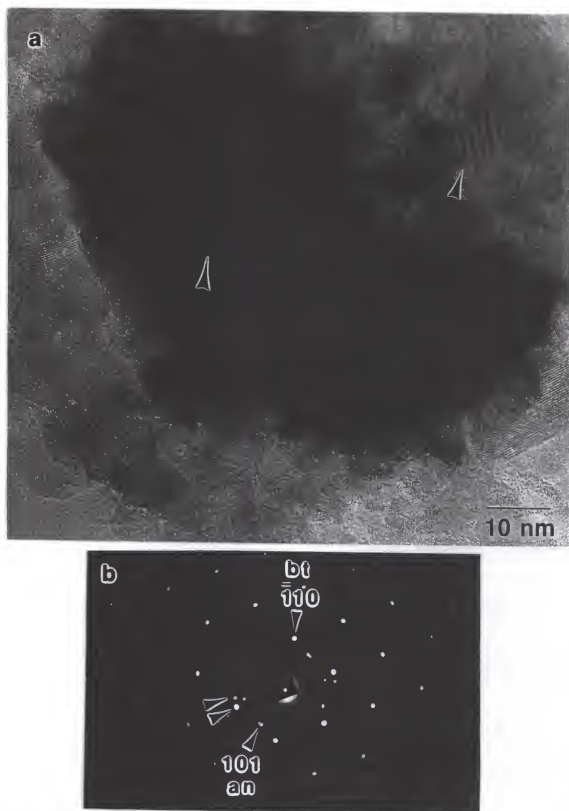


Figure 6-13. HRTEM micrograph of the sample BC-05 including selected area diffraction pattern. The double arrows indicate a split reflection spot of  $\text{BaTiO}_3$  due to lattice misfit. The 'an' and 'bt' represent the reflection spots for the anatase and  $\text{BaTiO}_3$ , respectively.

continuously consuming the anatase. The rate limiting step is the dissolution of the titania. Therefore, overall reaction kinetics are slower than the system involving the more reactive amorphous Ti gel as shown in Figure 6-5.

Several  $\text{BaTiO}_3$  crystallites can heterogeneously nucleate on that same anatase particle. This probably produces lattice misorientation between crystallites, exhibiting a Moire fringe as indicated in Figure 6-13. Unlike the case of  $\text{BaTiO}_3$  from the amorphous Ti gel, nucleation occurs only on the smallest anatase particle. As a result, it was observed that the average particle size ( $\sim 0.2 \mu\text{m}$ ) at the later stage of reaction in this case is larger than the  $\text{BaTiO}_3$  particle ( $\sim 0.05 \mu\text{m}$ ) obtained from the amorphous Ti gel. As all smaller anatase particles are consumed, the required supersaturation level is difficult to maintain and no further particle growth occurs unless larger anatase particles dissolve. The schematic picture illustrating this proposed mechanism is given in Figure 6-14.

### Conclusions

It was determined that the Ti precursor characteristics influenced formation mechanisms of  $\text{BaTiO}_3$  by examining crystallization kinetics at  $75^\circ\text{C}$ . Increased reaction kinetics without an induction period was observed when the amorphous Ti precursor was involved, as compared to the hydrothermally treated Ti precursor. However, no complete transformation was achieved in either case within the currently investigated reaction time. The maximum crystallinity for  $\text{BaTiO}_3$  formation from the as-received Ti and hydrothermally treated Ti precursors was 0.652 and 0.475, respectively.

Based on Johnson-Mehl-Avrami kinetics analysis and microstructural evidence during reaction, the predominant formation mechanisms at the early stages of the reaction were evaluated. In  $\text{BaTiO}_3$  formation involving the amorphous Ti gel, relatively spherical 5 to 10 nm size nuclei which grew out of the amorphous gel matrix were monitored by high resolution TEM. As a relevant formation mechanism, a phase boundary controlled mechanism in which the surface chemical reaction is the rate controlling step is proposed.

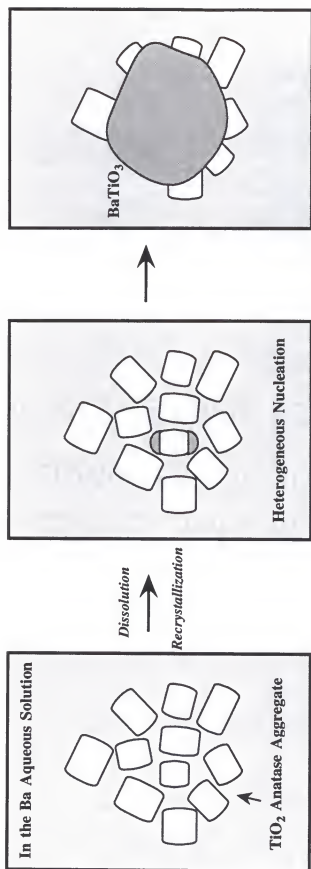


Figure 6-14. Schematic picture illustrating a proposed particle formation mechanism of  $\text{BaTiO}_3$  in the hydrothermally treated Ti gel and barium hydroxide system.

On the other hand, 80 nm size particles which grew on the aggregated anatase were observed in the case of  $\text{BaTiO}_3$  formation from the hydrothermally treated Ti precursor. It is believed that  $\text{BaTiO}_3$  nucleates heterogeneously on the anatase particles via dissolution and recrystallization. Particles grow at the expense of the neighboring anatase. Aggregation between the primary  $\text{BaTiO}_3$  particles is likely to occur in both cases, which produced Moire fringes inside the particles.

The current study, performed at mild hydrothermal conditions (i.e.,  $<100^\circ\text{C}$ ), can facilitate a better understanding of  $\text{BaTiO}_3$  formation mechanisms under severe hydrothermal conditions. However, care must be exercised since the predominant mechanism may change as a function of reaction temperature and pressure. Furthermore, phase transformation behavior of the Ti precursors via a hydrothermal treatment can be utilized in the hydrothermal synthesis of  $\text{BaTiO}_3$  as a possible controlling parameter for crystallization kinetics and even particle size and morphology. Depending on the hydrothermal pretreatment conditions such as the pH, temperature, and time, the characteristics of the Ti precursors which are subjected to react with the injected  $\text{Ba}^{2+}$  will be different. Therefore, in-situ control over the characteristics of the resulting  $\text{BaTiO}_3$  can be achieved.

## CHAPTER 7 CONCLUSIONS AND SUGGESTIONS FOR FUTURE WORK

### Overall Conclusions

A low temperature hydrothermal synthesis procedure which is characterized by the use of stable modified titanium alkoxide with acetylacetone and barium acetate has been developed in the current research. Chemical modification increases the stability of the metal alkoxide against moisture and eventually controls the degree of hydrolysis and condensation. During solution mixing, clear solution precursor in which very fine colloidal Ti sols (~ 5 nm) are homogeneously dispersed in the barium aqueous solution. From this precursor, an intimately mixed Ba-Ti complex hydrous gel was coprecipitated when added into a KOH solution. Well-crystalline cubic BaTiO<sub>3</sub> particles are directly precipitated from such hydrous gel suspensions at temperatures as low as 50°C during hydrothermal treatment.

The pH of the reaction medium plays an important role in the crystallization process. Phase-pure BaTiO<sub>3</sub> can be synthesized only at a highly alkaline condition (i.e., pH>13) under a CO<sub>2</sub>-free atmosphere. The particle size of the hydrothermally derived BaTiO<sub>3</sub> powder ranged from 0.05 - 0.35 µm and could be controlled by proper selection of synthesis conditions such as reaction concentration, temperature and time. To complete the evaluation of the synthesized BaTiO<sub>3</sub> powders, the sintering behavior and dielectric properties were investigated. A pellet was prepared by applying 80 MPa of uniaxial pressure and sintered at 1300°C for 3 hours. The distribution of grain sizes was broad, ranging from 2 to 8 µm, indicating the presence of exaggerated grain growth. This poor microstructure can be attributed to currently involved high sintering temperature and improper forming method. Nonetheless, relatively reasonable results were obtained in

which the dielectric constant and dissipation factor at 1 kHz, 26°C were 1923 and 0.7 %, respectively.

The synthesis of other ferroelectric materials such as  $\text{SrTiO}_3$ ,  $\text{PbTiO}_3$ , PZT, and PLZT has been tried to evaluate the feasibility of the modified Ti alkoxide as a new precursor for hydrothermal particle synthesis. Starting from the modified Ti isopropoxide and metal acetate salts, these Ti-based perovskite ceramics were synthesized at lower temperatures than previously reported. The phase-pure  $\text{PbTiO}_3$  can be synthesized as low as 150°C while other materials at 110°C. The same reaction parameter influence as in the  $\text{BaTiO}_3$  system on the resulting powder characteristics such as phase composition, particle size and particle morphology has been observed. It was demonstrated that the phase-pure stoichiometric perovskites form only when the pH of the initial feedstock solution is about 14, similar to the  $\text{BaTiO}_3$  system. Reaction concentration also significantly influenced the particle size and shape.

To gain a better understanding of particle formation mechanisms, the kinetics of the  $\text{BaTiO}_3$  nucleation under hydrothermal conditions were investigated. The approach was to extract intermediate-stage samples for characterization by XRD and TEM. Crystallization kinetics were determined by a quantitative XRD study, which eventually permitted derivation of reaction rates and consideration of the reaction mechanism by which transformation occurred. In the current research, the Johnson-Mehl-Avrami method was used to perform kinetic analysis on the conversion data. The results of kinetic analysis were corroborated against microstructural evidence to predict rate-controlling mechanisms during hydrothermal reactions. TEM observation provided strong evidence of morphological evolution during transformation with respect to reaction time. Special emphasis was given to monitoring the nucleation process directly at the very early stage of reaction. The Johnson-Mehl-Avrami analysis was originally developed for solid-state reactions based on statistical phenomenology. However, it was demonstrated that careful application of this kinetic analysis can provide meaningful insights regarding particle

formation mechanisms in the solution phase, as an additional clue to verify inference from microstructural evidence.

The characteristics of the Ti precursors significantly influenced the particle formation mechanism of BaTiO<sub>3</sub> under hydrothermal conditions. Dissolution and recrystallization was proposed in the BaTiO<sub>3</sub> system involving the modified precursor and barium acetate, based on the direct observation of spherical 4 nm size BaTiO<sub>3</sub> nuclei using high resolution TEM. The morphology of the nuclei transformed into cubic particles during the intermediate stage of growth and then most return to the spherical shape during the final stage. This tendency is probably due to competing effects between the crystallographic habit growth and strain effect associated with cubic-phase stabilization. Under such conditions, the Ba-Ti complex gel dissolves into the aqueous soluble species, from which BaTiO<sub>3</sub> homogeneously nucleates directly from supersaturated solution. The relevant reaction was proposed as  $\text{BaOH}^+ + \text{Ti}(\text{OH})_4 \leftrightarrow \text{BaTiO}_3 + 2\text{H}_2\text{O} + \text{H}^+$ .

When BaTiO<sub>3</sub> forms by reacting either amorphous Ti gel or hydrothermally treated nanosize anatase in aqueous barium hydroxide solution at 75°C, on the other hand, different particle formation processes were monitored. Faster reaction kinetics without an induction period were observed in the case of the amorphous Ti precursor, as compared to the hydrothermally treated Ti precursor. However, complete transformation could not be achieved in either case within the currently investigated reaction time. The maximum crystallinity for BaTiO<sub>3</sub> formation from the amorphous Ti and hydrothermally treated Ti precursors was 0.652 and 0.475, respectively. The average particle sizes also varied so that larger BaTiO<sub>3</sub> particles, approximately 0.2 μm, were synthesized from the amorphous Ti gel, as compared to the 0.04 μm BaTiO<sub>3</sub> particles from the anatase precursor. In the former case, relatively spherical 5 to 10 nm size nuclei which grew out of the amorphous gel matrix were monitored by high resolution TEM. As a relevant formation mechanism, a phase boundary controlled model was predicted in which the chemical reaction between TiO<sub>2</sub> and Ba<sup>2+</sup> at the interfaces gave rise to the nucleation of BaTiO<sub>3</sub>. In contrast, 80 nm

size  $\text{BaTiO}_3$  particles which grew on the aggregated anatase were observed in the latter case. As a consequence, it was proposed that  $\text{BaTiO}_3$  nucleates heterogeneously on the anatase particles via dissolution and recrystallization.

### Future Work

In the currently developed synthesis procedure, it is believed that the chemical modifying agent, acetylacetone, plays an important role in enhancing crystallization kinetics. The exact chemical behavior throughout hydrothermal particle synthesis should be carefully examined. First of all, the structure of amorphous Ba-Ti complex gel should be thoroughly understood by TGA/DTA, FTIR, and TEM. Scanning TEM together with electron dispersion X-ray (EDX) can provide information regarding how the Ba and Ti are distributed inside gel structure. In particular, the influence of acetylacetone on the solubility of Ti species during hydrothermal conditions must be evaluated. The experimental approach includes treatment of Ti-acetylacetonate complexes in solution over a range of pH values and reaction temperatures (25 - 150°C). Both a solid and its supernatant solution samples are extracted at temperature as a function of pH. By measuring soluble Ti species, the solubility diagram for the Ti-acetylacetone- $\text{H}_2\text{O}$  system as a function of temperature can be constructed. Secondly, it is necessary to determine the change in the characteristics of hydrothermally derived particles and crystallization kinetics as a degree of chemical modification of the Ti precursor increases.

Acetylacetone has a strong complexing ability towards Ti species as discussed in Chapter 4. This tendency may indicate the presence of acetylacetone species on the particle surface, even after hydrothermal treatment. In this regard, thirdly, the surface chemical character of the hydrothermally derived  $\text{BaTiO}_3$  need to be determined by FTIR and Raman spectroscopy. In addition, Hall-Williamson analysis method can provide information concerning the internal structure of the particles by evaluating the microstrain and crystallite

size. Ultimately, the systematic study concerning the role of the chemical modifying agent should be evaluated based on the sintering behavior and dielectric property measurements.

As described in Chapter 3, the stability diagram of the Ba-Ti-H<sub>2</sub>O system predicts that BaTiO<sub>3</sub> is thermodynamically stable at 25°C under alkaline conditions. However, no one has reported particle synthesis of BaTiO<sub>3</sub> at 25°C. As a consequence, it is academically interesting to monitor the nucleation process at 25°C as a function of aging time to verify the theoretical prediction. Although complete crystallization would not be achieved due to kinetic reasons, BaTiO<sub>3</sub> nuclei of critical size may be observed by either high resolution TEM or small angle X-ray scattering (SAXS).

Regarding the particle formation mechanism study, in the current research, the influence of the Ti precursor characteristics was evaluated at fixed reaction conditions. However, predominant mechanisms may change as a function of reaction conditions. Therefore, crystallization kinetics should be analyzed as a function of reaction temperature, time, and concentration. Furthermore, quantitative XRD analysis needs to be supplemented by kinetic information assessed by unreacted solution species to produce more accurate data for the extent of crystallization. Due to the relating insolubility of titanium in solution, elemental analysis by an inductive coupled plasma spectroscopy (ICP) for atomic Ba will provide appropriate reaction kinetics of BaTiO<sub>3</sub> crystallization. Only under these circumstances, will in-depth knowledge concerning particle formation mechanisms in the hydrothermal synthesis of BaTiO<sub>3</sub> be obtained.

## LIST OF REFERENCES

1. B. Jaffe, W. Cook, and H. Jaffe, Piezoelectric Ceramics, Academic Press, Inc., New York, NY, 1971.
2. R. E. Newnham, "Electroceramics," *Rep. Prog. Phys.*, **52**, 123-156 (1989).
3. D. Hennings, "Barium Titanate Based Ceramic Materials for Dielectric Use," *Int. J. High Technol. Ceram.*, **3**, 91-111 (1987).
4. G. Goodman, "Ceramic Capacitor Materials," pp. 79-138 in Ceramic Materials for Electronics: Processing, Properties, and Applications, Edited by R.C. Buchanan, Marcel Dekker Inc., New York, NY, 1986.
5. M. Kahn, D. P. Burks, I. Burn, and W. A. Schulze, "Ceramic Capacitor Technology," pp. 191-274 in Electronic Ceramics: Properties, Devices, and Applications, Edited by L. M. Levinson, Marcel Dekker Inc., New York, NY, 1988.
6. L. E. Cross, "Dielectric, Piezoelectric, and Ferroelectric Components," *Am. Ceram. Soc. Bull.*, **63**, 586-590 (1984).
7. A. K. Maurice and R. C. Buchanan, "Preparation and Stoichiometry Effects on Microstructure and Properties of High Purity BaTiO<sub>3</sub>," *Ferroelectrics*, **74**, 61-75 (1987).
8. A. Beauge, J. C. Mutin, and J. C. Niepce, "Synthesis Reaction of Metatitanate BaTiO<sub>3</sub>," *J. Mat. Sci.*, **18**, 3041-3050 (1983).
9. W. Johnson, Jr, "Innovations in Ceramic Powder Preparation," pp. 3-19 in Advances in Ceramics Vol 21. Ceramic Powder Science, Edited by G.L. Messing, K.S. Mazdhyasni, J.W. McCauley, R.A. Haber, The American Ceramic Society Inc., Westerville, OH, 1987.
10. M. Stockenhuber, H. Mayer, and J. A. Lercher, "Preparation of Barium Titanate from Oxalates," *J. Am. Ceram. Soc.*, **76**, 1185-1190 (1993).
11. M. H. Frey and D.A. Payne, "Synthesis and Processing of Barium Titanate Ceramics from Alkoxide Solutions and Monolithic Gels," *Chem. Mater.*, **7**, 123-129 (1995).
12. Y. Hayashi, T. Kimura, T. Yamaguchi, "Preparation of Rod-Shaped BaTiO<sub>3</sub> Powder," *J. Mater. Sci.*, **21**, 757-762 (1986).
13. J. Menashi and R. C. Reid, *Barium Titanate Powders*, U.S. Patent No. 4,829,033, May 9, 1989.

14. H. Kumazawa, S. Annen, and E. Sada, "Hydrothermal Synthesis of Barium Titanate Fine Particles from Amorphous and Crystalline Titania," *J. Mater. Sci.*, **30**, 4740-4744 (1995).
15. W. J. Dawson, J. C. Preston, and S. L. Swartz, "Processing Issues of Hydrothermal Synthesis of Fine Dielectric Powders," pp. 27-32 in Ceramics Transactions, Vol. 22, Ceramic Powder Science IV, Edited by S. Hirano, G.L. Messing, and H. Hausner, The American Ceramic Society Inc., Columbus, OH, 1991.
16. E. Barringer, N. Jubb, B. Fegley, R. L. Pober, and H. K. Bowen, "Processing Monosized Powders," pp. 315-33 in Ultrastructure Processing of Ceramics, Glasses, and Composites, Edited by L. L. Hench and D. R. Ulrich, John Wiley & Son, New York, 1984.
17. S. Hirano, "Hydrothermal Processing of Ceramics," *Am. Ceram. Soc. Bull.*, **66**, 1342-1344 (1987).
18. R. A. Laudise, "Hydrothermal Synthesis of Crystals," *Chem. Eng. News*, Sept. **28**, 30-43 (1987).
19. W. J. Dawson, "Hydrothermal Synthesis of Advanced Ceramic Powders," *Am. Ceram. Soc. Bull.*, **67**, 1673-1678 (1988).
20. A. N. Christensen, "Hydrothermal Preparation of Barium Titanate by Transport Reactions," *Acta Chem. Scand.*, **24** [7] 2447-2452 (1970).
21. K. Abe, M. Aoki, H. Rikimaru, T. Ito, K. Hidaka, and K. Segawa, *Process for Producing a Composition Which Includes Perovskite Compounds*, U.S. Patent 4,643,984, Feb.17, 1987.
22. T.R.N. Kutty and P. Murugaraj, "Hydrothermal Precipitation and Characterization of Polytitanates in the System BaO-TiO<sub>2</sub>," *J. Mater. Sci. Lett.*, **7**, 601-603 (1988).
23. E. Lilley and R. Wusarika, *Method for the Production of Mono-Size Powders of Barium Titanate*, U.S. Patent No. 4,764,493, August 16, 1988.
24. M. K. Klee and H. W. Brand, *Method of Manufacturing Powdered Barium Titanate*, U.S. Patent No. 4,859,448, August 22, 1989.
25. P. K. Dutta and J. R. Gregg, "Hydrothermal Synthesis of Tetragonal Barium Titanate," *Chem. Mater.*, **4**, 843-846 (1992).
26. D. Hennings, G. Rosenstein, and H. Schreinemacher, "Hydrothermal Preparation of Barium Titanate from Barium-Titanate Acetate Gel Precursors," *J. Euro. Ceram. Soc.*, **8**, 107-115 (1991).
27. R. P. Denkwics, Jr., K. S. TenHuisen, and J. H. Adair, "Hydrothermal Crystallization Kinetics of m-ZrO<sub>2</sub> and t-ZrO<sub>2</sub>," *J. Mater. Res.*, **5**, 2698-2705 (1990).
28. P. P. Phule and S. H. Risbud, "Review: Low-Temperature Synthesis and Processing of Electronic Materials in the BaO-TiO<sub>2</sub> System," *J. Mater. Sci.*, **25**, 1169-1183 (1990).

29. A. T. Chien, J. S. Speck, F. F. Lange, A. C. Daykin, and C. G. Levi, "Low Temperature/Low Pressure Hydrothermal Synthesis of Barium Titanate: Powders and Heteroepitaxial Thin Films," *J. Mater. Res.*, **7**, 1784-1789 (1995).
30. F. Chaput, J.-P. Boilot and A. Beauger, "Alkoxide-Hydroxide Route to Synthesize BaTiO<sub>3</sub>-Based Powders," *J. Am. Ceram. Soc.*, **73**[4], 942-948 (1990).
31. J. O. Eckert, Jr., C. C. Hung-Houston, B. L. Gersten, M. M. Lencka, and R. E. Riman, "Kinetics and Mechanisms of Hydrothermal Synthesis of Barium Titanate," submitted to *J. Am. Ceram. Soc.*
32. W. Hertl, "Kinetics of Barium Titanate Synthesis," *J. Am. Ceram. Soc.*, **71**, 879-883 (1988).
33. G. A. Rossetti, Jr., D. J. Watson, R. E. Newnham and J. H. Adair, "Kinetics of the Hydrothermal Crystallization of the Perovskite Lead Titanate," *J. Cryst. Growth*, **116**, 251-259 (1992).
34. L. L. Hench and J. K. West, Principles of Electronic Ceramics, John Wiley & Sons, New York, NY, 1990.
35. R. W. Whatmore, "An Introduction to Ferroelectric Ceramics and Their Applications," pp. 223-254 in Fundamentals of Ceramic Engineering, Edited by P. Vincenzini, Elsevier Science Publishers, London, UK, 1991.
36. L. M. Sheppard, "Advances in Processing of Ferroelectric Thin Films," *Am. Ceram. Soc. Bull.*, **71** [1] 85-95 (1992).
37. W. D. Kingery, H. K. Bowen, and D. R. Uhlmann, Introduction to Ceramics, 2nd Edition, John Wiley & Sons, New York, NY, 1976.
38. G. H. Heartling, pp. 139-225 in Ceramic Materials for Electronics: Processing, Properties, and Applications, Edited by R.C. Buchanan, Marcel Dekker Inc., New York, NY, 1986.
39. A. J. Moulson and J. M. Herbert, Electroceramics: Materials, Properties, Applications, Chapman & Hall, London, UK, 1990.
40. J. M. Herbert, Ceramic Dielectrics and Capacitors, Gordon and Breach Science Publishers, New York, NY, 1985.
41. H. Emoto and J. Hojo, "Sintering and Dielectric Properties of BaTiO<sub>3</sub>-Ni Composite Ceramics," *J. Ceram. Soc. Japan*, **100**[4], 555-559 (1992).
42. H. C. Ling and M. F. Yan, "Processing of Lead-Based Dielectric Materials," pp. 397-419 in Chemical Processing of Ceramics, Edited by B. I. Lee and E. J. A. Pope, Marcel Dekker Inc., New York, NY, 1994.
43. T. R. Shrout and A. Halliyal, "Preparation of Lead-Based Ferroelectric Relaxors for Capacitors," *Am. Ceram. Soc. Bull.*, **66**[4], 704-711 (1987).

44. T-S. Yeh and M. D. Sacks, "Effect of Green Microstructure on Sintering of Alumina," pp. 309-331 in Ceramic Transactions, Vol 7, Sintering of Advanced Ceramics, Edited by C.A. Handwerker, J.E. Blendell, and W.A. Kaysser, The American Ceramic Society Inc., Westerville, OH, 1990.
45. Y. Suyama and T. Yamaguchi, "Powders for Advanced Ceramics: Characterization and Synthesis," pp. 121-151 in Fundamentals of Ceramic Engineering, Edited by P. Vincenzini, Elsevier Science Publishers, London, UK, 1991.
46. R. E. Riman, "The Chemical Synthesis of Ceramic Powders," pp. 29-69 in Surface and Colloid Chemistry in Advanced Ceramic Processing, Edited by R. J. Pugh and L. Bergstrom, Surfactant Science Series Vol 51, Marcel Dekker Inc., New York, NY, 1994.
47. M. D. Sacks, Class Notes for Ceramic Processing, EMA 6448, University of Florida, Gainesville, Spring 1994.
48. S. G. Malghan, P. S. Wang, and V. A. Hackley, "Techniques for Characterization of Advanced Ceramic Powders," pp. 129 -153 in Chemical Processing of Ceramics, Edited by B. I. Lee and E. J. A. Pope, Marcel Dekker Inc., New York, NY, 1994.
49. J. A. Voigt, "Powder and Precursor Preparation by Solution Techniques," pp. 1-27 in Characterization of Ceramics, Edited by R. E. Loehman and L. E. Fitzpatrick, Butterworth-Heinemann, Boston, MA, 1993.
50. P. K. Gallagher and J. Thomson, "Thermal Analysis of Some Barium and Strontium Titanyl Oxalates," *J. Am. Ceram. Soc.*, **48**[12], 644-647 (1965).
51. T. Mah, E. E. Hermes, K. S. Mazdiasni, "Multicomponent Ceramic Powders," pp. 75-103 in Chemical Processing of Ceramics, Edited by B. I. Lee and E. J. A. Pope, Marcel Dekker Inc., New York, NY, 1994.
52. T.-T. Fang, H.-B. and J.-B. Hwang, "Thermal Analysis of Precursors of Barium Titanate Prepared by Coprecipitation," *J. Am. Ceram. Soc.*, **73**[11], 3363-3367 (1990).
53. P. K. Dutta, P. K. Gallagher, and J. Twu, "Raman Spectroscopic Study of the Formation of Barium Titanate from an Oxalate Precursor," *Chem. Mater.*, **5**, 1739-1743 (1993).
54. K. Saegusa, W. E. Rhine, and H. K. Bowen, "Preparation of Stoichiometric Fine Lead Barium Titanate Powder," *J. Am. Ceram. Soc.*, **76**[6], 1495-1504 (1993).
55. C. J. Brinker and G. W. Scherer, Sol-Gel Science: The Physics and Chemistry of Sol-Gel Processing, Academic Press, Boston, 1990.
56. K. S. Mazdiasni, R. T. Dolloff, and J. S. Smith II, "Preparation of High-Purity Submicron Barium Titanate Powders," *J. Am. Ceram. Soc.*, **52**[10], 523 (1969).
57. P.P. Phule and S.H. Risbud, "Low Temperature Synthesis and Dielectric Properties of Ceramics Derived from Amorphous Barium Titanate Gels and Crystalline Powders," *Mat. Sci. Eng.*, **B3**, 241-247 (1989).

58. Y. Suyama and M. Nagsawa, "Single-Crystal Barium Titanium Isopropoxide Complex to Form Barium Titanate," *J. Am. Ceram. Soc.*, **77**[2], 603-605 (1994).
59. M. P. Pechini, *Barium Titanate and Processes for Producing Same*, U. S. Patent No. 2,985,506, May 23, 1961.
60. E. Matijevic, "Colloid Science in Ceramic Powders Preparation," pp. 441-458 in Materials Science Monographs Vol. 38A, High Tech Ceramics Part A, Edited by P. Vincenzini, Elsevier Science Publishers, New York, NY, 1987.
61. E. Matijevic, "Preparation and Properties of Uniform Size Colloids," *Chem. Mater.*, **5**, 412-426 (1993).
62. P. Gherardi and E. Matijevic, "Homogeneous Precipitation of Spherical Colloidal Barium Titanate Particles," *Colloids and Surfaces*, **32**, 257-274 (1988).
63. Y.-S. Her, E. Matijevic, and M. C. Chon, "Preparation of Well-Defined Colloidal Barium Titanate Crystals by the Controlled Double-Jet Precipitation," *J. Mater. Res.*, **10**, 3106-3114 (1995).
64. D. Segal, Chemical Synthesis of Advanced Ceramic Materials, Cambridge University Press, Cambridge, 1989.
65. S.-B. Cho, S. Venigalla, and J. H. Adair, "Morphological Control of  $\alpha$ - $\text{Al}_2\text{O}_3$  in 1,4-Butanediol Solution," pp. 135-50 in Ceramic Transaction, Vol. 54, Science, Technology, and Applications of Colloidal Suspensions, Edited by J. H. Adair, J. A. Casey, C. A. Randall, and S. Venigalla, American Ceramic Society, Westerville, OH, 1995.
66. T. Kimura and T. Yamaguchi, "Morphology Control of Electronic Ceramic Powders by Molten Salt Synthesis," pp 169-177 in Advances in Ceramics Vol 21, Ceramic Powder Science, Edited by G. L. Messing, K. S. Mazdiyasn, J. W. McCauley, R. A. Haber, The American Ceramic Society Inc., Westerville, OH, 1987.
67. A. Shaikh and G. M. Vest, "Kinetics of  $\text{BaTiO}_3$  and  $\text{PbTiO}_3$  Formation from Metallo-Organic Precursors," *J. Am. Ceram. Soc.*, **69**[9], 682-688 (1986).
68. S. Kumar, G. L. Messing, and W. B. White, "Metal Organic Resin Derived Barium Titanate: I. Formation of Barium Titanate Oxycarbonate Intermediate," *J. Am. Ceram. Soc.*, **76**[3], 617-624 (1993).
69. T. S. Shrout, P. Papet, S. Kim, and G.-S. LEE, "Conventionally Prepared Submicrometer Lead-Based Perovskite Powders by Reactive Calcination," *J. Am. Ceram. Soc.*, **73**[7], 1862-1867 (1990).
70. G. R. Fox, J. H. Adair, and R. E. Newnham, "Effect of pH and  $\text{H}_2\text{O}_2$  upon Coprecipitated  $\text{PbTiO}_3$  Powders: Part I Properties of As-Precipitated Powders," *J. Mat. Sci.*, **25**, 3634-3640 (1990).
71. M.-H. Lee and B.-C. Chol, "Crystallization of Lead Titanate Prepared by Wet Chemical Methods," *J. Am. Ceram. Soc.*, **74**[9], 2309-2311 (1991).

72. C. T. Lin, B. W. Scanlan, J. D. McNeil, J. S. Webbs, L. Li, R. A. Lipeles, P. M. Adams, and M. S. Leung, "Crystallization Behavior in a Low Temperature Acetate Process for Perovskite  $\text{PbTiO}_3$ ,  $\text{Pb}(\text{Zr,Ti})\text{O}_3$ , and  $(\text{Pb}_{1-x}\text{La}_x)(\text{Zr}_y\text{Ti}_{1-y})_{1-x/4}\text{O}_3$  Bulk Powders," *J. Mater. Res.*, **7**, 2546-2554 (1992).
73. J. B. Blum and S. R. Gorkovich, "Sol-Gel Derived  $\text{PbTiO}_3$ ," *J. Mat. Sci.*, **20**, 4479-4483 (1985).
74. M. J. Kim and E. Matijevic, "Preparation and Characterization of Uniform Submicrometer Lead Titanate Particle," *Chem. Mater.*, **1**, 363-369 (1989).
75. D. J. Watson, C. A. Randall, R. E. Newnham, and J. H. Adair, "Hydrothermal Formation Diagram in the Lead Titanate System," pp 154-162 in Ceramics Transactions, Vol 1, Ceramic Powder Science II, Edited by G. L. Messing, E. R. Fuller Jr., H. Hausner, The American Ceramic Society Inc., Westerville, OH, 1988.
76. J. Moon, T. Li, C. A. Randall, and J. H. Adair, "Low Temperature Synthesis of Lead Titanate by a Hydrothermal Method," submitted to *J. Mater. Res.*
77. S. Sato, T. Murakata, H. Yanagi, F. Miyasaka, and S. Iwaya, "Hydrothermal Synthesis of Fine Perovskite  $\text{PbTiO}_3$  Powders with a Simple Mode of Size Distribution," *J. Mater. Sci.*, **29**, 5657-5663 (1994).
78. R. H. Arendt and J.H. Rosolowski, *Molten Salt Synthesis of Lead Zirconate Titanate Solid Solution Powder*, U.S. Patent, 4,152,282, May 1, 1979.
79. A. P. Singh, S. K. Mishra, D. Pandey, C. D. Prasad, and R. Lal, "Low Temperature Synthesis of Chemically Homogeneous Lead Zirconate Titanate (PZT) Powders by a Semi-Wet Method," *J. Mater. Sci.*, **28**, 5050-5055 (1993).
80. H.-W. Wang, D. A. Hall, and F. R. Sale, "Phase Homogeneity and Segregation in PZT Powders Prepared by Thermal Decomposition of Metal-EDTA Complexes Derived from Nitrate and Chloride Solutions," *J. Am. Ceram. Soc.*, **75**[1], 124-130 (1992).
81. C. M. R. Baston, M. Jafellicci, Jr., J. A. Varela, and M. A. Zaghette, "Preparation of PZT from Citrates," pp. 1983-1990 in Ceramics Today-Tomorrow's Ceramics, Edited by P. Vincenzini, Elsevier Science Publishers, London, UK, 1991.
82. B. G. Muralidharan, A. Sengupta, G. S. Rao, and D. C. Agrawal, "Powders of  $\text{Pb}(\text{Zr}_x\text{Ti}_{1-x})\text{O}_3$  by Sol-Gel Coating of  $\text{PbO}$ ," *J. Mater. Sci.*, **30**, 3231-3237 (1995).
83. C. D. E. Lakeman and D. A. Payne, "Processing Effects in the Sol-Gel Preparation of PZT Dried Gels, Powders, and Ferroelectric Thin Layers," *J. Am. Ceram. Soc.*, **75**[11], 3091-3096 (1992).
84. K. C. Beal, "Precipitation of Lead Zirconate Titanate Solid Solution under Hydrothermal Conditions," pp 33-41 in Advances in Ceramics Vol 21, Ceramic Powder Science, Edited by G. L. Messing, K. S. Mazdiyasni, J. W. McCauley, R.A. Haber, The American Ceramic Society Inc., Westerville, OH, 1987.
85. H. Cheng, J. Ma, B. Zhu, and Y. Cui, "Reaction Mechanisms in the Formation of Lead Zirconate Titanate Solid Solutions under Hydrothermal Conditions," *J. Am. Ceram. Soc.*, **76** [3], 625-629 (1993).

86. T. R. N. Kutty and R. Balachandran, "Direct Precipitation of Lead Zirconate Titanate by the Hydrothermal Method," *Mat. Res. Bull.*, **19**, 1479-1488 (1984).
87. T. Kimura, A. Takenaka, T. Mifune, Y. Hayashi, and T. Yamaguchi, "Preparation of Needle-Like PZT Powder," *J. Mater. Sci.*, **27**, 1497-1483 (1992).
88. T. R. Shrout, B. Jones, J. V. Biggers, and J. H. Adair, "Enhanced Processing of Perovskite  $\text{Pb}(\text{Mg}_{1/3}\text{Nb}_{2/3})\text{O}_3$  Relaxors through Understanding the Surface Chemistry of the Component Powders," pp. 519-527 in Ceramics Transactions, Vol. 22, Ceramic Powder Science IV, Edited by S. Hirano, G. L. Messing, and H. Hausner, The American Ceramic Society Inc., Columbus, OH, 1991.
89. F. Chaput, J. P. Boilot, M. Lejeune, R. Papiernik, and L. G. Huber-Pfalzgraf, "Low Temperature Route to Lead Magnesium Niobate," *J. Am. Ceram. Soc.*, **67**[5], 311-315 (1988).
90. P. Ravindranathan, S. Komarneni, A. S. Bhalla, R. Roy, and L. E. Cross, "Sol-Gel Processing of Lead Magnesium Niobate (PMN) Powder and its Characterization," pp.182-195 in Ceramics Transactions, Vol. 22, Ceramic Powder Science IV, Edited by S. Hirano, G. L. Messing, and H. Hausner, The American Ceramic Society Inc., Columbus, OH, 1991.
91. K. H. Yoon, Y.-S. Cho, D.-H. Lee, and D.-H. Kang, "Powder Characteristics of  $\text{Pb}(\text{Mg}_{1/3}\text{Nb}_{2/3})\text{O}_3$  Prepared by Molten Salt Synthesis," *J. Am. Ceram. Soc.*, **76** [5], 1373-1376 (1993).
92. L. Gordon, M. L. Salutsky, and H. H. Willard, Precipitation from Homogeneous Solution, John Wiley and Sons, Inc., New York, NY, 1959.
93. A. E. Nielsen, Kinetics of Precipitation, The Macmillan Co., New York, NY, 1964.
94. H. Furedi-Milhofer and A. G. Walton, "Principles of Precipitation of Fine Particles," pp. 203-272 in Dispersion of Powders in Liquids, Edited by G.D. Parfitt, Applied Science, London, 1985.
95. A. Mersmann, "Fundamentals of Crystallization," pp. 1-78 in Crystallization Technology Handbook, Edited by A. Mersmann, Marcel Dekker Inc., New York, NY, 1995.
96. N. S. Tavare, Industrial Crystallization: Process Simulation Analysis and Design, Plenum Press, New York, NY, 1995.
97. A. S. Myerson and R. Ginde, "Crystals, Crystal Growth, and Nucleation," pp. 33-63 in Handbook of Industrial Crystallization, Edited by A. S. Myerson, Butterworth-Heinemann, Boston, MA, 1993.
98. M. A. Larson and J. Garside, "Solute Clustering and Interfacial Tension," *J. Crystal Growth*, **76**, 88-92 (1986).
99. J. Nyvlt, O. Sohnel, M. Matuchova, and M. Broul, The Kinetics of Industrial Crystallization. Chemical Engineering Monographs Vol. 19, Elsevier, New York, NY, 1985.

100. E. Ruckenstein and B. Nowakowski, "A Kinetic Theory of Nucleation of Liquid," *J. Colloid Interface Sci.*, **137**, 583-592 (1990).
101. P.-P. Chiang, M. D. Donohue, and J. L. Katz, "A Kinetic Approach to Crystallization from Ionic Solution: II Crystal Nucleation," *J. Colloid Interface Sci.*, **122**, 251-265 (1988).
102. A. D. Randolph and M. A. Larson, Theory of Particulate Processes: Analysis and Techniques of Continuous Crystallization, Academic Press Inc., San Diego, CA, 1988.
103. R. Boistelle and J. P. Astier, "Crystallization Mechanisms in Solution," *J. Crystal Growth*, **90**, 14-30 (1988).
104. P. Chiang and M. D. Donohue, "A Kinetic Approach to Crystallization from Ionic Solution: I Crystal Growth," *J. Colloid Interface Sci.*, **122**, 230-250 (1988).
105. W. K. Burton, N. Cabrera and F. C. Frank, "The Growth of Crystals and the Equilibrium Structure of their Surfaces," *Phil. Trans. Roy. Soc. London*, **A243**, 299-358 (1951).
106. A. E. Nielsen, "Precipitates: Formation, Coprecipitation, and Aging," pp. 304-306 in Treatise on Analytical Chemistry, Part I, Theory and Practice, 2nd Ed., Volume 3, Edited by I.M. Kolthoff and P.J. Elving, John Wiley and Sons, Inc., 1983.
107. J. Estrin, "Precipitation Process," pp. 131-149 in Handbook of Industrial Crystallization, Edited by A. S. Myerson, Butterworth-Heinemann, Boston, MA, 1993.
108. P. Chiang and M. D. Donohue, "The Effect of Complex Ions on Crystal Nucleation and Growth," *J. Colloid Interface Sci.*, **126**, 579-591 (1988).
109. E. Matijevic, "Control of Powder Morphology," pp. 513-527 in Chemical Processing of Advanced Materials, Edited. L. L. Hench and J. K. West, John Wiley and Sons, New York, NY, 1992.
110. G. Wulff, "Zur Frage der Geschwindigkeit des Wachstums und der Auflösung der Kristallflächen," *Z. Krist.*, **34**, 449-530 (1901).
111. T. Sugimoto, "Preparation of Monodispersed Colloidal Particles," *Adv. Colloid Interface Sci.*, **28**, 65-108 (1987).
112. J. D. H. Donnay and D. Harker, "A New Law of Crystal Morphology Extending the Law of Bravais," *Amer. Min.*, **22**, 446-467 (1937).
113. P. Hartman and W.G. Perdok, "On the Relations Between Structure and Morphology of Crystals I," *Acta Cryst.*, **8**, 49-52 (1955).
114. P. Hartman, "Structure and Morphology," pp. 367-402, in Crystal Growth: An Introduction, Edited by P. Hartman, North-Holland, Amsterdam, 1973.
115. P. Hartman and P. Bennema, "The Attachment Energy as a Habit Controlling Factor. I. Theoretical Considerations," *J. Cryst. Growth*, **49**, 145-156 (1980).

116. P. Bennema, "Growth and Morphology of Crystals: Integration of Theories of Roughening and Hartman-Perdok Theory," pp. 477-581 in Handbook of Crystal Growth, Vol. 1, Edited by D.T.J. Hurle, Elsevier Science Publishers B.V., New York, NY, 1993.
117. E. I. Givargizov, Oriented Crystallization on Amorphous Substrates, Plenum Press, New York, 1991.
118. D. L. Klug, "The Influence of Impurities and Solvents on Crystallization," pp. 65-87 in Handbook of Industrial Crystallization, Edited by A. S. Myerson, Butterworth-Heinemann, Boston, MA, 1993.
119. G. M. Van Rosmalen and P. Bennema, "Characterization of Additive Performance on Crystallization: Habit Modification," *J. Cryst. Growth*, **99**, 1053-1060 (1990).
120. T. Sugimoto, Preparation and Characterization of Monodisperse Colloidal Particles," *MRS Bulletin*, December, 23-28 (1989).
121. J. Th. G. Overbeek, "Monodisperse Colloidal Systems, Fascinating and Useful," *Adv. Colloid Interface Sci.*, **15**, 251-277 (1982).
122. W. Stober, A. Fink, and E. Bohn, "Controlled Growth of Monodisperse Silica Spheres in the Micro Size Range," *J. Colloid Interface Sci.*, **26**, 62-69 (1968).
123. P. Calvert, "Precipitation of Monodisperse Ceramic Particles; Theoretical Models," pp 79-84 in Better Ceramics Through Chemistry II, Edited by C. J. Brinker, D. E. Clark, and C. R. Ulrich, Materials Research Society, Pittsburgh, 1986.
124. J. Stavek, M. Sipek, I. Hirasawa, and K. Toyokura, "Controlled Double-Jet Precipitation of Sparingly Soluble Salts. A Method for the Preparation of High Added Value Materials," *Chem. Mater.*, **4**, 545-555 (1992).
125. V.K. LaMer and R.H. Dinegar, "Theory, Production and Mechanism of Formation of Monodisperse Hydrosols," *J. Am. Chem. Soc.*, **72**, 4847-4854 (1950).
126. T. Matsoukas and E. Gulari, "Dynamics of Growth of Silica Particles from Ammonia-Catalyzed Hydrolysis of Tetra-ethyl-orthosilicate," *J. Colloid Interface Sci.*, **124**, 252-261 (1988).
127. T. Matsoukas and E. Gulari, "Monomer Addition Growth with A Slow Initiation Step: A Growth Model for Silica Particles from Alkoxides," *J. Colloid Interface Sci.*, **132**, 13-21 (1989).
128. G. H. Bogush and C. F. Zukoski, "Uniform Silica Particle Precipitation: An Aggregative Growth Model," *J. Colloid Interface Sci.*, **142**, 19-34 (1991).
129. C. F. Zukoski, M. K. Chow, G. H. Bogush, and J-L Look, "Precipitation of Uniform Particles: The Role of Aggregation," pp. 131-140 in Better Ceramics Through Chemistry IV, Edited by B. J. Zelinski, C. J. Brinker, D. E. Clark, and C. R. Ulrich, Materials Research Society, Pittsburgh, 1990.

130. K. Osseo-Asare, F. J. Arriagada, and J.H. Adair, "Solubility Relationships in the Coprecipitation Synthesis of Barium Titanate: Heterogeneous Equilibria in the Ba-Ti-C<sub>2</sub>O<sub>4</sub>-H<sub>2</sub>O System," pp 47-53 in Ceramics Transactions, Vol 1, Ceramic Powder Science II, Edited by G.L. Messing, E.R. Fuller Jr., H. Hausner, The American Ceramic Society Inc., Westerville, OH, 1988.
131. M. M. Lencka and R. E. Riman, "Thermodynamic Modeling of Hydrothermal Synthesis of Ceramic Powders," *Chem. Mater.*, **5**, 61-67 (1993).
132. B. L. Utech, *The Effect of Solution Chemistry on Barium Titanate Ceramics*, The Pennsylvania State University, University Park, 1990.
133. G. B. Naumov, B. N. Ryzhenko, I.L. Khodakovskiy, Handbook of Thermodynamic Data, I. Barnes, V. Speltz. Eds., U.S. Geological Survey, Menlo Park, CA, 1974.
134. M. M. Lencka and R. E. Riman, "Synthesis of Lead Titanate: Thermodynamic Modeling and Experimental Verification," *J. Am. Ceram. Soc.*, **76**[10], 2649-2659 (1993).
135. M. M. Lencka and R. E. Riman, "Hydrothermal Synthesis of Perovskite Materials: Thermodynamic Modeling and Experimental Verification," *Ferroelectrics*, **151**, 159-164 (1994).
136. M. M. Lencka and R. E. Riman, "Thermodynamics of the Hydrothermal Synthesis of Calcium Titanate with Reference to Other Alkaline-Earth Titanates," *Chem. Mater.*, **7**, 18-25 (1995).
137. M. Henry, J. P. Jolivet, and J. Livage, "Aqueous Chemistry of Metal Cations: Hydrolysis, Condensation, and Complexation," pp.153-206 in Chemistry, Spectroscopy and Applications of Sol-Gel Glasses, Structure and Bonding Vol. 77, Edited by R. Reisfeld and C. K. Jorgensen, Springer-Verlag, Berlin, Germany, 1992.
138. J. Livage, M. Henry, and J. P. Jolivet, "Inorganic Polymerization in Aqueous Solutions," pp. 223-237 in Chemical Processing of Advanced Materials, Edited by L. L. Hench and J. K. West, John Wiley and Sons, New York, NY, 1992.
139. I. S. Butler and J. F. Harrod, Inorganic Chemistry: Principles and Applications, The Benjamin/Cummings Publishing Company Inc., Redwood City, CA, 1988.
140. J. Livage, M. Henry, and J. P. Jolivet, and C. Sanchez, "Chemical Synthesis of Fine Powders," *MRS Bulletin*, Vol. 15[1], 18-25 (1990).
141. C.F. Baes, and R.E. Mesmer, The Hydrolysis of Cations, Wiley-Interscience, New York, NY, 1976.
142. F. A. Cotton and G. Wilkinson, Advanced Inorganic Chemistry, 5th Edition, Wiley & Sons, New York, NY, 1988.
143. L. I. Bekkerman, I. P. Dobrovolskii, and A. A. Ivakin, "Effect of the Composition of Titanium (IV) Solutions and Conditions of Precipitation on the Structure of the Solid Phase," *Russ. J. Inorgan. Chem.*, **21**[2], 223-226 (1976).

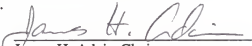
144. G. Pfaff, "BaTiO<sub>3</sub> Preparation by Reaction of TiO<sub>2</sub> with Ba(OH)<sub>2</sub>," *J. Euro. Ceram. Soc.*, **8**, 35-39 (1991).
145. J. Livage, "Molecular Design of Transition Metal Alkoxide Precursors," pp. 3-22 in Chemical Processing of Ceramics, Edited by B. I. Lee and E. J. A. Pope, Marcel Dekker Inc., New York, NY, 1994.
146. J. Livage, C. Sanchez, M. Henry, and S. Doeuff, "The Chemistry of the Sol-Gel Process," *Solid State Ionics*, **32/33**, 633-638 (1989).
147. P. P. Phule and F. Khairulla, "Molecularly Modified Alkoxide Precursors(MMAP) for Synthesis of Electroceramic Powders"; pp 725-32 in Ceramics Transactions, Vol 12, Ceramic Powder Science III, Edited by G. L. Messing, S.-I. Hirano, Jr. H. Hausner, The American Ceramic Society Inc., Westerville, OH, 1990.
148. C. Sanchez, J. Livage, M. Henry, and F. Babonneau, "Chemical Modification of Alkoxide Precursors," *J. Non-Cryst. Solids*, **100**, 65-76 (1988).
149. C. Sanchez, P. Toledano and F. Ribot, "Molecular Structure of Metal Alkoxide Precursors"; pp 47-59 in Better Ceramics Through Chemistry IV, Edited by B. J. Zelinski, C. J. Brinker, D. E. Clark, and C. R. Ulrich, Materials Research Society, Pittsburgh, 1990.
150. S. Kawaguchi, "Variety in the Coordination Modes of  $\beta$ -Dicarbonyl Compounds in Metal Complexes," *Coordination Chemistry Reviews*, **70**, 51-94 (1986).
151. A. Yamanoto and S. Kambara, "Structure of the Reaction Products of Tetraalkoxytitanium with Acetylacetone and Ethylacetoacetate," *J. Am. Chem. Soc.*, **79**, 4344-4348 (1957).
152. A. Leautic, F. Babonneau, and J. Livage, "Structural Investigation of the Hydrolysis-Condensation Process of Titanium Alkoxides Ti(OR)<sub>4</sub> (OR=OPr<sup>i</sup>,OEt) Modified by Acetylaceton. 1. Study of the Alkoxide Modification," *Chem. Mater.*, **1**, 240-47 (1989).
153. A. Leautic, F. Babonneau, and J. Livage, "Structural Investigation of the Hydrolysis-Condensation Process of Titanium Alkoxides Ti(OR)<sub>4</sub> (OR=OPr<sup>i</sup>,OEt) Modified by Acetylaceton. 2. From the Modified Precursor to the Colloids," *Chem. Mater.*, **1**, 248-52 (1989).
154. S. J. Milne and S. H. Pyke, "Modified Sol-gel Process for the Production of Lead Titanate Films," *J. Am. Ceram. Soc.*, **74**[6] 1407-10 (1991).
155. L. G. Hubert-Pfalzgraf, O. Poncelet and J-C. Daran, "Tailored Molecular Precursors of Yttrium Oxide using Functional Alcohols and Acetylacetone as Modifiers," pp 73-78 in Better Ceramics Through Chemistry IV, Edited by B. J. Zelinski, C. J. Brinker, D. E. Clark, and C. R. Ulrich, Materials Research Society, Pittsburgh, 1990.
156. R. Vivekanandan, and T. R. N. Kutty, "Characterization of Barium Titanate Fine Powders Formed From Hydrothermal Crystallization," *Powder. Technol.*, **57**, 181-192 (1989).

157. R. Vivekanandan, S. Philip, and T. R. N. Kutty, "Hydrothermal Preparation of Ba(Ti,Zr)O<sub>3</sub> Fine Powders," *Mater. Res. Bull.*, **22** [1] 99-108 (1986).
158. T. Allen, Particle Size Measurement, Chapman and Hall, New York, NY, 1990.
159. R. L. Scheaffer and J. T. McClave, Probability and Statistics for Engineers, PWS-KENT Publishing Company, Boston, MA, 1990.
160. K. Uchino, E. Sadanaga, and T. Hirose, "Dependence of the Crystal Structure on Particle Size in Barium Titanate," *J. Am. Ceram. Soc.*, **72** [8] 1555-58 (1989).
161. B. D. Begg, E. R. Vance, and J. Nowotny, "Effect of Particle Size on the Room-Temperature Crystal Structure of Barium Titanate," *J. Am. Ceram. Soc.*, **77**[12], 3186-3192 (1994).
162. P. K. Dutta, R. Asiaie, S. A. Akbar, and W. Zhu, "Hydrothermal Synthesis and Dielectric Properties of Tetragonal BaTiO<sub>3</sub>," *Chem. Mater.*, **6**, 1542-1548 (1994).
163. G. Arlt, D. Hennings, and G. de With, "Dielectric Properties of Fine-Grained Barium Titanate Ceramics," *J. Appl. Phys.*, **58**[4], 1619-1625 (1985).
164. M. J. Avrami, "Kinetics of Phase Change. I," *J. Chem. Phys.*, **7**, 1103-1112 (1939).
165. S. F. Hulbert, "Models for Solid-State Reactions in Powdered Compacts: A Review," *J. Brit. Ceram. Soc.*, **6**, 11-20 (1969).
166. J. D. Hancock and J. H. Sharp, "Method of Comparing Solid-State Kinetic Data and Its Applications to the Decomposition of Kaolinite, Brucite, and BaCO<sub>3</sub>," *J. Am. Ceram. Soc.*, **55**, 74-77 (1992).
167. T. Tani, Z. Xu, and D. Payne, "Preferred Orientations for Sol-Gel Derived PLZT Thin Layers," pp. 269-274 in Ferroelectric Thin Films III. Symposium Proceedings Vol. 310, Edited by E. R. Myers, B. A. Tuttle, S. B. Desu, and P. K. Lauser, Material Research Society, Pittsburgh, 1993.
168. R. C. Evans, An Introduction to Crystal Chemistry, 2nd Edition, Cambridge University Press, New York, 1964.
169. H. Cheng, J. Ma, Z. Zhao, and L. Qi, "Hydrothermal Preparation of Uniform Nanosize Rutile and Anatase Particles," *Chem. Mater.*, **7**, 663-671 (1995).
170. M. Kondo, K. Shinozaki, R. Ooki, and N. Mizutani, "Crystallization Behavior and Microstructure of Hydrothermally Treated Monodispersed Titanium Dioxide Particles," *J. Ceram. Soc. Japan*, **102**, 742-746 (1994).
171. T. R. N. Kutty and P. Padmini, "Wet Chemical Formation of Nanoparticles of Binary Perovskites through Isothermal Gel to Crystalline Conversion," *Mater. Res. Bull.*, **27** [8] 945-952 (1992).

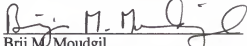
## BIOGRAPHICAL SKETCH

Jooho Moon is the youngest son of Chang-Soon Moon and Sook-Hee Park, born on December 6, 1967, in Seoul, Korea. He attended Yonsei University in Seoul, Korea. During his undergraduate studies, he served as a teacher in Catholic Sunday school for 4 years. In the Spring of 1990, the author graduated with a Bachelor of Science in ceramic engineering from Yonsei University. He then began his pursuit of a doctoral degree in the Department of Materials Science and Engineering at the University of Florida in the Spring of 1992. He received a Master of Science in materials science and engineering and also an award of Excellent Academic Achievement from the Office of International Studies and Programs at the University of Florida in August, 1995. He is currently a member of both the Korean and American Ceramic Societies.

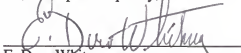
I certify that I have read this study and that in my opinion it conforms to acceptable standards of scholarly presentation and is fully adequate, in scope and quality, as a dissertation for the degree of Doctor of Philosophy.

  
James H. Adair, Chairman  
Associate Professor of Materials  
Science and Engineering

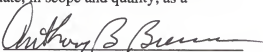
I certify that I have read this study and that in my opinion it conforms to acceptable standards of scholarly presentation and is fully adequate, in scope and quality, as a dissertation for the degree of Doctor of Philosophy.

  
Brij M. Moudgil  
Professor of Materials Science and  
Engineering

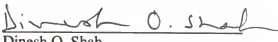
I certify that I have read this study and that in my opinion it conforms to acceptable standards of scholarly presentation and is fully adequate, in scope and quality, as a dissertation for the degree of Doctor of Philosophy.

  
E. Dow Whitney  
Professor of Materials Science and  
Engineering

I certify that I have read this study and that in my opinion it conforms to acceptable standards of scholarly presentation and is fully adequate, in scope and quality, as a dissertation for the degree of Doctor of Philosophy.

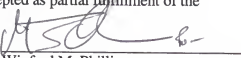
  
Anthony B. Brennan  
Associate Professor of Materials  
Science and Engineering

I certify that I have read this study and that in my opinion it conforms to acceptable standards of scholarly presentation and is fully adequate, in scope and quality, as a dissertation for the degree of Doctor of Philosophy.

  
Dinesh O. Shah  
Professor of Chemical Engineering

This dissertation was submitted to the Graduate Faculty of the College of Engineering and to the Graduate School and was accepted as partial fulfillment of the requirements for the degree of Doctor of Philosophy.

August, 1996

  
Winfred M. Phillips  
Dean, College of Engineering

  
Karen A. Holbrook  
Dean, Graduate School